Die Relevanz von Phasenübergängen für die katalytischen Eigenschaften von Oxidationskatalysatoren

The relevance of phase transitions in terms of the catalytic properties of oxidation catalysts

Wissenschaftliche Arbeit zur Erlangung des Grades

Master of Science

an der Fakultät für Chemie der Technischen Universität München

Betreut von Professor Dr. Klaus Köhler

Lehrstuhl für Anorganische Chemie

Technische Universität München

Eingereicht von Maximilian James Werny

Julbach am Inn

Eingereicht am Garching, den 20.02.2018

Die Relevanz von Phasenübergängen für die katalytischen Eigenschaften von Oxidationskatalysatoren

The relevance of phase transitions in terms of the catalytic properties of oxidation catalysts

Wissenschaftliche Arbeit zur Erlangung des Grades

Master of Science

an der Fakultät für Chemie der Technischen Universität München

Co-Betreut von Dr. Annette Trunschke

Department of Inorganic Chemistry – Reactivity Group

Fritz-Haber-Institut der Max-Planck-Gesellschaft

Eingereicht von Maximilian James Werny

Julbach am Inn

Eingereicht am Garching, den 20.02.2018

Acknowledgements

Firstly, I would like to thank **Prof. Dr. Robert Schlögl** for the opportunity to work in his Department of Inorganic Chemistry at the Fritz-Haber-Institute of the Max-Planck-Society in Berlin.

I would then like to gratefully acknowledge my direct co-supervisor and group leader of the Reactivity group, **Dr. Annette Trunschke**, for the numerous constructive discussions and her continuous support during my thesis. Thank you for a pleasant six months in your group. I would also like to extend sincere thanks to **Prof. Dr. Klaus Köhler** at the Technische Universität München for acting as co-supervisor of my thesis.

My work and results would not have been possible without the help of my colleagues in the Department of Inorganic Chemistry. I would like to thank **Dr. Yuanqing Wang** for his supervision and outstanding support during Raman spectroscopy, **Pierre Kube** for the catalytic activity measurements, technical support and many fruitful discussions, **Dr. Frank Girgsdies** for the elaborate XRD measurements, **Dr. Andrey Tarasov** and **Jasmin Allan** for TG-DSC and TG-DTA, **Wiebke Frandsen** and **Danail Ivanov** for SEM-EDX measurements, **Dr. Olaf Timpe** for XRF and ICP-OES, **Maike Hashagen** for BET measurements, **Dr. Hamideh Ahi** for UV/Vis-spectroscopy and her constructive feedback on my research, **Samuel Tragl** and **Jutta Kröhnert** for their support during UV/Vis-spectroscopy, **Dr. Gregor Koch** for his helpful advice in many situations and **Daniel Brennecke** and **Sven Richter** for their dedicated technical support in the laboratory and administrative matters. I must also thank **Dr. Milivoj Plodinec** and the team of **Thermo Fisher Scientific** in Eindhoven for the *in-situ* TEM experiments. My sincere gratitude goes to **Dr. Rupert Hochleitner** (Mineralogische Staatssammlung München) and **Dr. Ralf-Thomas Schmitt** (Museum für Naturkunde, Berlin) for providing the braunite samples that I required for analysis.

Last but not least, I would like to thank my family, **Mum**, **Dad**, **Louisa** and **Sophia**, for bringing me so far and giving me the motivation to succeed.

Abstract

Die strukturelle Dynamik des Mn-Na_2WO_4/SiO_2 Katalysators unter Reaktionsbedingungen wurde mittels *in-situ* und *operando* Raman-Spektroskopie untersucht. Die Aktivität des Systems steht im Zusammenhang mit der Verfügbarkeit einer vermutlich fein-dispergierten MnO_x-Spezies. Hohe Methanumsätze führten zu einem Abfall der Sauerstoffkonzentration in der Reaktionsatmosphäre und schließlich zu einer Reduktion der geträgerten Mn_7SiO_{12}-Phase zu $MnWO_4$. Eine entsprechende Abnahme der aktiven Zentren ist anzunehmen. Die Reversibilität dieser Phasenumwandlung wurde unter Reaktionsbedingungen beobachtet.

Die katalytische Relevanz der redox-aktiven Mn_7SiO_{12}-Phase wurde ebenfalls aus TG-DSC-MS/TG-DTA-MS Messungen entnommen. Eine Sauerstofffreigabe von 0.21 Gew% fand bei hohen Temperaturen (ab 680 °C, Maximum bei 918 °C) statt.

Eine weitere Phasenumwandlung, in Form einer partiellen Verflüssigung der Na_2WO_4-Phase, wird auf Basis von *in-situ* Raman Messungen ab 581 °C vermutet. *In-situ* XRD Experimente bestätigten diesen Trend.

Abbreviations and Symbols

A	Ampere, electrical current
Å	Ångström, 10^{-10} m
at%	atomic percent
a.u.	arbitrary unit
BET	Brunauer-Emmett-Teller
CCD	charge-coupled device
cm^{-1}	inverse centimeter, wavenumber
cps	counts per second
C_2	ethane + ethene
DSC	differential scanning calorimetry
DTA	differential thermal analysis
EDX	energy dispersive X-ray spectroscopy
et al.	*et alii* (lat.)
eV	electron volt
FHI	Fritz-Haber-Institut
FTIR	Fourier-transform infrared spectroscopy
FTS	Fischer Tropsch synthesis
G	gram, mass
GC	gas chromatograph
GHSV	gas hourly space velocity
h	hour, time
HTRS	high-temperature Raman spectroscopy
ICP-OES	inductively coupled plasma-optical emission spectroscopy
K	Kelvin, temperature
L	lattice vibration/translational mode
MDA	methane dehydroaromatization
MEMS	microelectromechanical system
min	minute, time
MS	mass spectrometry
MTA	methanol-to-aromatics
MTG	methanol-to-gasoline
MTO	methanol-to-olefins
MTOAH	methanol-to-olefins-aromatics-hydrogen
m.p.	melting point
m/z	mass-to-charge ratio
n	molarity
NIR	near infrared

OCM	oxidative coupling of methane
p	pressure
Pa	Pascal, pressure
PASCA	positron annihilation spectroscopy for chemical analysis
QE	quantum efficiency
RT	room temperature
S	selectivity
S_{BET}	surface area (BET)
SDD	silicon drift detector
SE	secondary electron
SEM	scanning electron microscope
STP	standard temperature and pressure
S/TEM	scanning/ transmission electron microscope
S/V	surface-area-to-volume ratio
Tc	thermocouple
TEM	transmission electron microscope
TG	thermogravimetry
TGA	thermogravimetric analysis
TPD	temperature-programmed desorption
TPR	temperature-programmed reduction
TUB	Technische Universität Berlin
UV	ultraviolet
V	Volt, electrical potential
Vis	visible
W	Watt, power
W/F	catalyst weight/feed flow rate
wt%	weight percent
X	conversion
XAES	X-ray absorption spectroscopy near edge structure
XPS	X-ray photoelectron spectroscopy
XRD	X-ray diffraction
XRF	X-ray fluorescence spectroscopy
$\delta_{s/as}$	symmetric/antisymmetric bending mode
θ	theta, angle
λ	lambda, wavelength
$\nu_{s/as}$	symmetric/antisymmetric stretching mode
ω_{obs}	observed wavenumber
°	degree, angle
°C	degree Celsius, temperature

Table of Contents

1 Introduction

Methane is the largest constituent of natural gas, yet possesses numerous thermodynamic and kinetic challenges in its selective one-step conversion to value-added products.[1] Despite its abundance[2], not a single process for the direct utilisation of methane has been fully implemented on an industrial scale for economic reasons. In fact, the majority of the global methane production is combusted for energy generation and mobility.[2b]

In order to access higher value products from methane, current technology focusses on the multi-step, capital intensive steam reforming process to produce syngas (CO/H_2), followed by the water-gas shift reaction to control the ratio of CO and H_2 and finally Fischer Tropsch (FTS), methanol synthesis or ammonia synthesis (refer to **Figure 1**).[1, 2b, 3] The obtained methanol can then be further converted using technologies such as methanol-to-olefins (MTO), methanol-to-gasoline (MTG) and methanol-to-aromatics (MTA).[1] The conversion of methane to hydrocyanic acid via the Andrussow and Degussa processes has also been established.[4]

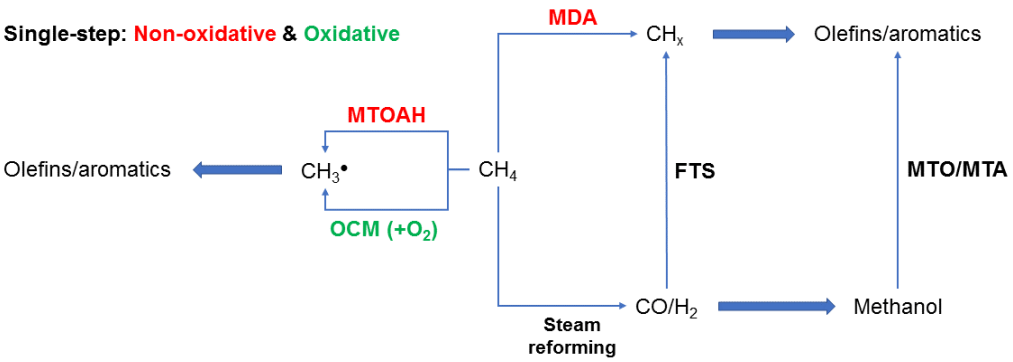

Figure 1: C-C coupling reaction pathways of methane to olefins and aromatics.

The high transportation costs of methane as well as the remoteness of its extraction sites underline the need for conducting further process and catalyst research, to ultimately establish feasible, single-step reactions that convert methane on-site.[1] To date, the direct conversion of methane to higher value chemicals is either conceivable via non-oxidative pathways such as methane dehydroaromatization (MDA) and the methane-to-olefins-aromatics-hydrogen (MTOAH) reaction or via the oxidative coupling of methane (OCM) (**refer to Figure 1**).

First reported in 1993[5], the MDA technology is based on bifunctional zeolite-supported metal catalysts that selectively produce benzene from methane. The most widely studied catalysts, Mo/HZSM-5 and Mo/MCM-22, possess selectivities in the range of 60-80%.[6] However, they feature a relatively low methane conversion (~10%) and a limited lifetime caused by extensive coke deposition.[6-7]

The MTOAH pathway was reported more recently by Guo *et al*..[8] Here, single iron sites embedded in a non-acidic silica matrix are responsible for converting methane to olefins, aromatics and hydrogen. A methane conversion of 48.1% and ethene selectivity of 48.4% were reported at 1090 °C. Furthermore, the total hydrocarbon selectivity exceeded 99%.

Since the pioneering works of Keller and Bhasin[9], Hinsen and Baerns[10] and Ito and Lunsford[11] in the early 1980s, the oxidative coupling of methane has received great attention in the scientific community. A methane conversion of 20−30% at a relatively high C_2 selectivity of 70−80% can be realised in a single pass using a Mn-Na_2WO_4/SiO_2 catalyst.[12]

2 Theoretical Background

2.1 Oxidative coupling of methane (OCM)

The oxidative coupling of methane to higher hydrocarbons is an attractive alternative to current crude oil-based processes, especially for accessing valuable C_2-compounds such as ethane and ethene.

Mechanistically speaking, the reaction is thought to occur via a heterogenous-homogenous mechanism, in which catalyst surface-generated methyl radicals continue to react in the gas-phase.[13] While the existence of these methyl radicals has been the experimentally proven for different catalysts under relevant conditions (Lunsford *et al*.[14], Buyevskaya *et al*.[15]), the exact mechanism behind the C−H bond cleavage is still debated. The heterolytic bond dissociation to yield CH_3^- and H^+ is based on the experimentally documented basicity of selective catalytic materials.[16] Here, the generated methyl anion loses an electron to form a methyl radical. However, since no experiments have been able to clearly support this pathway, homolytic bond cleavage or a combination of both pathways must be considered (refer to **Figure 2**).[13]

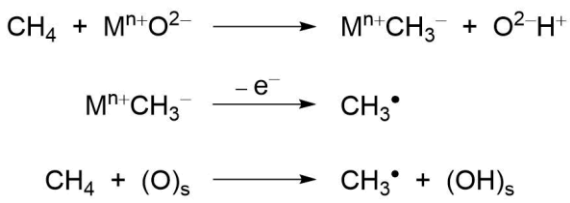

Figure 2: Heterolytic and homolytic C–H bond dissociation in methane.[13]

The recombination of gas-phase methyl radicals leads to the formation of ethane, which is dehydrogenated homogenously or heterogeneously in a consecutive reaction to yield ethene (refer to **Figure 3**).[13] In general, the exothermic nature of OCM results in the absence of thermodynamic limitations.[12a] Nevertheless, high temperatures, often exceeding 700 °C, must be maintained to for most practically viable OCM processes.[7] At these temperatures, both the total oxidation of methane/methyl radicals and the consecutive oxidation of the more reactive C_2-products are thermodynamically more favoured, subsequently resulting in the formation of CO_x and H_2O as side-products (refer to **Figure 3**).[7] This not only decreases the product yield, but also introduces additional downstream gas-separation costs.[7]

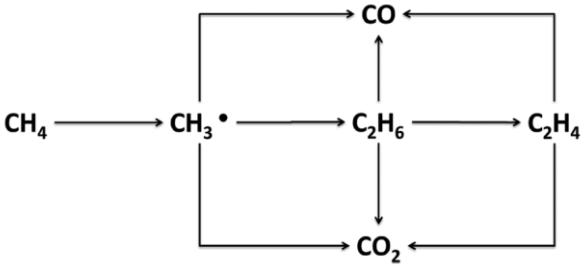

Figure 3: Simplified scheme of the OCM reaction network.[17]

The application of selective catalysts, which generate methyl radicals at lower temperatures without their consecutive heterogenous oxidation, is therefore paramount to the success of the reaction.[7, 12a, 13] A large variety of catalytic materials have been investigated for the oxidative coupling of methane.[16c, 18] Despite these efforts, not a single catalyst, displaying suitable activity, selectivity and stability, has been identified that would guarantee the feasibility of an industrially implemented full-scale process.[19]

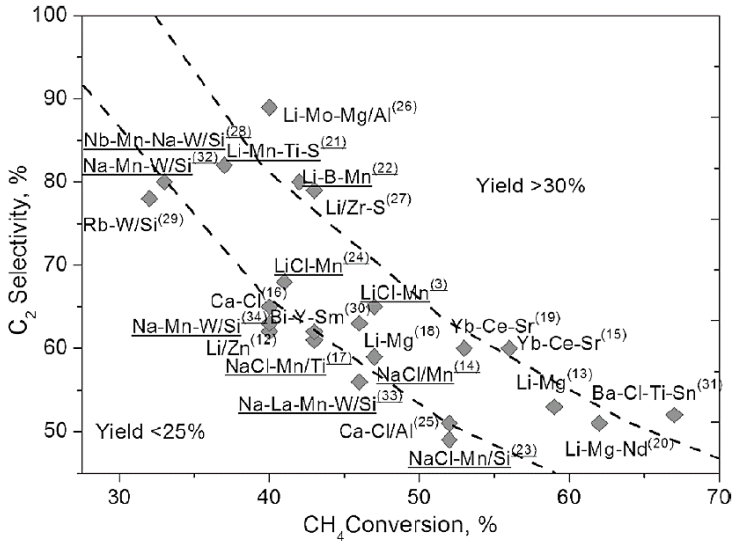

Figure 4: Elemental compositions of OCM catalysts with $Y(C_2) \geq 25\%$ reported in the literature. All the catalysts were tested in a fixed-bed reactor in the co-feed mode under atmospheric pressure at temperatures from 670 to 950 °C, $p(CH_4)/p(O_2) = 1.7-9.0$, and contact times from 0.2 to 5.5 s.[20]

Zavyalova *et al.* recently analysed catalysts, reported in approximately 420 publications since 1982, on the basis of their composition and performance (refer to **Figure 4**).[20] Their investigation showed that most high-performance catalysts exhibit strong basicity and are predominantly based on doped Mg- and La-oxides. While alkali (Na,Cs) and alkaline-earth (Sr, Ba) metal dopants increase the

selectivity of the host oxides, dopants such as Mn, W, and Cl enhance the methane conversion.

It is evident that the optimisation and detailed characterisation of existing catalysts are of critical importance for the sustainability of the OCM reaction on a techno-economic scale. By obtaining a better understanding of their working mechanism and structure-activity correlations, the discovery of novel catalytic systems may also be accelerated.

2.2 The Mn-Na_2WO_4/SiO_2 catalyst

2.2.1 Phase composition and activity

Since its discovery by Li *et al*. in 1992[21], the Mn-Na_2WO_4/SiO_2 catalyst has emerged as the most effective catalyst for OCM with its comparatively good performance ($X(CH_4)$ = 20−30%, $S(C_2)$ = 70−80%) and extended on stream stability at high temperatures.[12] As a result of its complex structure and phase composition, however, it is still unclear how the active phase and sites are constituted in the system.

In general, the calcined catalyst features Na_2WO_4 and Mn_2O_3 phases supported on an inert, low-surface area α-cristobalite support.[21] In certain cases, $Na_2W_2O_7$ and Mn-containing phases such as Mn_7SiO_{12} and $MnWO_4$ are also present.[12d, 22] This usually correlates with the respective composition, synthesis and applied activation procedures.

In 1993, Jiang *et al*. studied the oxide-support interaction as well as surface dispersion for a 1.9 wt% Mn-y wt% Na_2WO_4/SiO_2 catalyst by XRD, XPS and PASCA (positron annihilation spectroscopy for chemical analysis).[23] A strong interaction between the Na_2WO_4 phase and silica was observed in the region of y = 0−1.5 wt% Na_2WO_4, while a weaker interaction was observed in the range of y = 1.5−4.0 wt% Na_2WO_4. At 4.0 wt%, Na_2WO_4 was found to exist as a close-packed dispersed layer on the surface of the silica support, in preference to interacting with Mn oxide, which formed separate Mn_2O_3 crystallites. Maximum activity was observed here. Loadings higher than 4.0 wt% resulted in the formation of free, crystalline Na_2WO_4 and did not increase the activity further. A correlation between the catalyst performance and the dispersion of Na_2WO_4 on the catalyst surface was thus suggested. The group also proposed a redox mechanism involving a restructured WO_4 cluster compound with W═O and W–O–Si bonds as active species.

In 1995, Wang *et al*. suggested a Na−O−Mn motif as active site.[24] This was based on the observation that $NaMnO_4/MgO$, Mn-Na_2WO_4/SiO_2 and Mn-Na_2WO_4/MgO all displayed similar catalytic activity. The group suggested that Mn is responsible for O_2 activation while W imparts stability to the system.

Wu *et al*. reported on the activity of two differently prepared Na-WO_3/SiO_2 catalysts that possessed divergent WO_x structures. While both displayed a similar methane conversion (~21%), the catalyst featuring tetrahedral WO_4 produced a far superior C_2 selectivity in comparison to the catalyst containing octahedral WO_6. Thus, WO_4 was regarded as critical to the catalyst performance.

In 1997, Jiang *et al*. proposed a two-site model for the generation of methyl radicals via a redox mechanism.[25] While the activation of methane was postulated to occur at the W^{6+} sites, the activation of gas-phase O_2 was centred at the Mn^{3+} sites. The high activity of the catalyst was explained by an oxygen spillover from the Mn_2O_3 to the Na_2WO_4 phase.

In 1998, Palermo and co-workers studied different trimetallic, bimetallic and single metal formulations of Na, Mn and W supported on amorphous silica after calcination.[26] For the simplified systems, the amounts of metal components corresponded to the composition of the trimetallic catalyst (1.9 wt% Mn-5 wt% Na_2WO_4/SiO_2). Using XRD, XPS/XAES, TPR and catalytic activity testing, the group identified Na as a structural and chemical promoter. During calcination, the presence of Na was responsible for the phase transition of the catalytically active, amorphous silica support to crystalline yet catalytically inert α-cristobalite below the normal phase transition temperature, indicating a strong interaction of Na with the support. This α-cristobalite produced from amorphous silica during catalyst genesis displayed higher activity than pure α-cristobalite. The XRD results also underlined that the crystallinity of the support was enhanced by the presence of W. Na on the SiO_2 surface was shown to lead to a better dispersion and stabilization of WO_x species, thus indicating a structural interaction of W with Na.

In the same year, Kou *et al*. investigated a Mn-Na_2WO_4/SiO_2 catalyst using XAFS and XPS.[27] The surface of the fresh catalyst was mainly constituted by oxygen-enriched amorphous phases featuring tetrahedral WO_4 and octahedral MnO_6 groups. These were allocated to Na_2WO_4 and Mn_2O_3. After a 450 h run, the surface of the used catalyst was dominated by highly dispersed MnO_4 groups, consisting of tetrahedrally coordinated Mn^{2+} and coordinatively unsaturated, octahedrally coordinated Mn^{3+} sites. These ambivalent sites were proposed to enable lattice oxygen transport in a synergistic catalytic cycle with the tetrahedral WO_4 units.

A detailed study on the variation of the composition with respect to the catalyst performance was performed by Ji *et al.* using XPS, Raman spectroscopy, XRD and continuous micro-reactor testing.[22a] It was found that the relative composition of the catalyst could be changed to a certain extent while maintaining high catalyst selectivity and conversion (Na: 0.4−2.3 wt%, W: 2.2−8.9 wt%, Mn: 0.5−2.0 wt%). For catalysts of the composition x%Na-3.1%W-2%Mn/SiO_2, increasing the Na content from 0.4 to 1.6 wt% strongly increased the near-surface concentration of both Na and Mn as determined via XPS. This resulted in improved CH_4 conversion and C_2H_4 selectivity (refer to **Figure 5**). Amounts above 2.3 wt% Na consequently led to a decrease of catalyst performance, with the near-surface Mn concentration apparently determining catalyst activity.

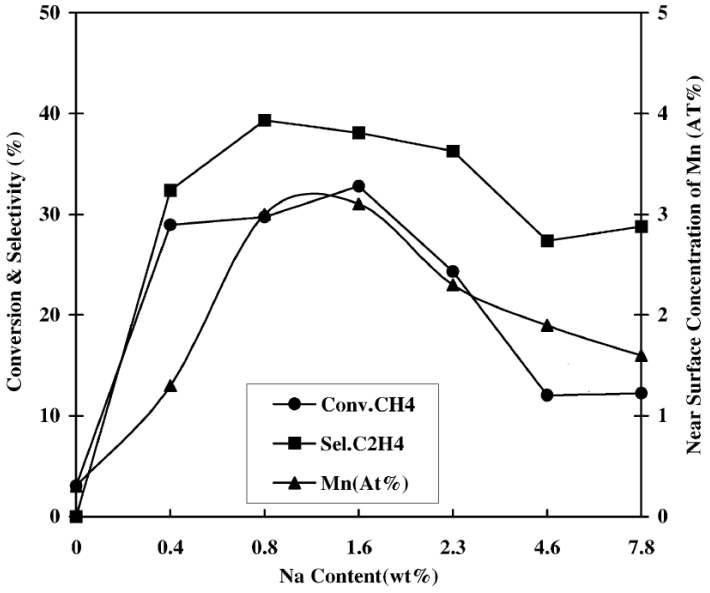

Figure 5: Correlation between near-surface concentration of Mn (at%) and CH_4 conversion and C_2H_4 selectivity in the x%Na-3.1%W-2%Mn/SiO_2 catalyst.[22a]

With the help of Raman spectroscopy, a correlation between the surface structure of these catalysts and the corresponding Na content was established. While the 0.4%Na-3.1%W-2%Mn/SiO_2 catalyst featured a band of octahedral WO_6 at 881 cm^{-1}, indicating $MnWO_4$, the 0.8%Na-3.1%W-2%Mn/SiO_2 catalyst contained several bands of tetrahedral WO_4 at 910, 925, 934 and 948 cm^{-1} instead, suggesting the presence of Na_2WO_4 and $Na_2W_2O_7$. XRD studies confirmed the presence of $Na_2W_2O_7$, Mn_2O_3 and $MnWO_4$ phases in the 0.4%Na-3.1%W-2%Mn/SiO_2 catalyst, while the 0.8%Na-3.1%W-2%Mn/SiO_2 catalyst mainly featured $Na_2W_2O_7$, Mn_2O_3 and Na_2WO_4. At loadings above 2.3 wt% Na, the amounts of $Na_2W_2O_7$ and Mn_2O_3 decreased while the concentration of Na_2WO_4

increased. Based on these findings, Ji and co-workers assumed that Na has a higher “affinity” for WO_4 than for Mn. A variation of the W content was also performed, with the 0.8%Na-y%W-2%Mn/SiO_2 catalyst displaying the highest conversion and C_2H_4 selectivity in the range of 2.2−8.9 wt% W. Interestingly, the near-surface concentration of W, as determined by XPS, was lower than the stoichiometrically derived atomic percentage. This indicates that W is present beneath the surface of the catalyst. The Raman spectra of the 0.8%Na-y%W-2%Mn/SiO_2 catalyst with y = 0.8−4.5 wt% contain bands that can be assigned to Mn_2O_3 and Na_2WO_4. Upon increasing the W content to 4.5 wt%, the 881cm^{-1} band of WO_6 ($MnWO_4$) also appeared. While this band became more pronounced at 8.9 wt% W, the bands assigned to tetrahedral WO_4 (Na_2WO_4) disappeared. Concurrently, a slight decrease in activity is observed. The activity dropped significantly for the 17.8 wt% W catalyst, in which $MnWO_4$ was found to exist as predominant phase. Thus, the formation of octahedral WO_6 can be attributed to the high W concentration. Similar results were obtained via XRD. While Mn_2O_3 was present from 0.4 wt% W onwards, Na_2WO_4 and $Na_2W_2O_7$ were formed at 0.8 wt% W. The formation of $MnWO_4$ occurred at 4.5 wt% and higher. A complete disappearance of the Mn_2O_3, Na_2WO_4 and $Na_2W_2O_7$ phases was evident at 17.8 wt% W. $MnWO_4$ remained as only phase. Considering the catalytic data for these systems, it can be concluded that the *in-situ* generated $MnWO_4$ phase on α-cristobalite may be inactive in the OCM. To further study the model catalyst, the Mn content was also changed. Systems of the composition 0.8%Na-3.1%W-z%Mn/SiO_2 with y = 0.5−2.0 wt% displayed high conversion and selectivity. XPS studies showed that the addition of Mn to the catalyst system led to a near-surface enrichment with Na. This is in agreement with the results of Palermo *et al*..[26] The Raman spectra of the 0.8%Na-3.1%W-z%Mn/SiO_2 catalysts contained a strong band at 910 cm^{-1} for z = 0.5−3.0 wt%, which was assigned to tetrahedral WO_4. Further increasing the Mn content in the catalyst led to a weakening of this band, while another band representing WO_4 at 948 cm^{-1} grew in intensity. At above 6.0 wt%, only the latter remained. This transition suggests that the Mn content in the catalyst exerts a strong influence on the vibration mode of tetrahedral WO_4 in the catalyst. No significant Raman bands corresponding to Mn_2O_3 were observed at contents below 2 wt% Mn. At 0.5 wt% Mn, reflections of Na_2WO_4 and $Na_2W_2O_7$ were detected via XRD. Mn_2O_3 was formed at 1.0 wt% Mn and higher. A new

phase in form of Mn_7SiO_{12} was reported at 6.0 wt% Mn. With the catalysts displaying decreased performance from 3.0 wt% Mn onwards, a correlation between the high surface coverage with Mn_7SiO_{12} and a reduced catalyst activity was postulated.

Using FTIR spectroscopy on a series of M−W−Mn/SiO_2 catalysts, Ji *et al*. also showed that the WO_4 tetrahedron has a stronger interaction with the cristobalite support than the WO_6 octahedron.[22b] Furthermore, they applied theoretical calculations to estimate the stabilities of the respective transition states with CH_4, concluding that WO_4 is energetically and geometrically more favoured.[22b]

In 2006, Hou *et al*. examined OCM on different sodium-salt modified Mn/SiO_2 catalysts.[28] The addition of salts containing WO_4^{2-}, MoO_4^{2-}, SO_4^{2-}, PO_4^{3-} and $P_2O_7^{4-}$ anions led to the transformation of the amorphous SiO_2 support to α-cristobalite and the concurrent oxidation of Mn_3O_4 to Mn_2O_3. This generally resulted in good catalyst activity and selectivity. The application of more basic salts containing CO_3^{2-} and SiO_3^{2-} led to the formation of Mn^{4+} species and consequently, a significantly reduced catalyst performance. Thus, Mn_2O_3 was considered to be active in the activation of methane.

Salehoun and co-workers studied the dynamics of the Mn-Na_2WO_4/SiO_2 catalyst using transient experiments.[29] The group was able to demonstrate the stable redox properties of the catalyst. It provided lattice oxygen for the reaction in absence of gas-phase oxygen.

2.2.2 On-stream stability

The group of Li studied the on-stream stability of the catalyst for 500 h and 1000 h in a fixed-bed reactor and for 450 h in a fluidized-bed reactor.[12b, 12c] In all three cases, catalyst stability was observed while maintaining a relatively constant performance. Structural studies also showed the disappearance of the supported crystalline Na_2WO_4 and Mn_2O_3 phases in the fixed-bed reactor experiments, without influencing the activity.[12b] The stability of the Mn-Na_2WO_4/SiO_2 system was also validated by several other groups for shorter time periods (15−100 h).[12d-f]

3 Objectives

The Mn-Na_2WO_4/SiO_2 catalyst system for the oxidative coupling of methane (OCM) has been extensively investigated over the last decades. Both the active site and the mechanism remain much debated, however. The tetrahedral WO_4 group is often postulated as active site, yet no comprehensive model explaining the functionality of the remaining phases in combination with WO_4 has been established. In fact, several publications also report on the Mn_2O_3 phase and its relevance for catalyst activity.

A model Mn-Na_2WO_4/SiO_2 catalyst, supplied by Simon *et al*.[12d] (Technische Universität Berlin), is investigated via *ex-situ* and *in-situ* X-ray diffraction, thermal analysis (TG-DSC-MS/TG-DTA-MS), electron microscopy (SEM-EDX/TEM-EDX) and *in-situ* and *operando* Raman spectroscopy to identify structural motifs and possible phase transitions under reaction conditions. In OCM, catalyst characterisation is often performed before or after the reaction due to the high-temperatures and the gas-phase chemistry that are involved. *Operando* Raman spectroscopy is a method that can be used to investigate the structural dynamics of the catalyst directly under reaction conditions. Ideally, new structure-activity correlations can be derived from the spectroscopic and catalytic data to enhance our knowledge and understanding of the catalyst's functionality and mechanism. Reference samples, in form of pure $Na_2WO_4{\cdot}2H_2O$ and $MnWO_4$ as well as natural Mn_7SiO_{12}, will also be examined thermally and spectroscopically at relevant temperatures. With pure Na_2WO_4 undergoing phase transition from solid to liquid at 695 °C, the formation of a catalytically active liquid component containing alkali and transition metal oxides will also be re-investigated for the Mn-Na_2WO_4/SiO_2 catalyst.

4 Results and Discussion

4.1 Structural composition and morphology of the Mn-Na_2WO_4/SiO_2 catalyst

The Mn-Na_2WO_4/SiO_2 catalyst was obtained by annealing coated SiO_2 granules, featuring a nominal composition of 2.0 wt% Mn^{2+}-ions and 4.5 wt% Na_2WO_4, for 8 h under air. No additional activation procedures were performed before analysis. The calcined catalyst was ground for XRD, Raman spectroscopy, TG-DSC/TG-DTA and TEM measurements.

4.1.1 X-ray fluorescence analysis (XRF) and inductively coupled plasma optical emission spectroscopy (ICP-OES)

To verify the exact composition of the catalyst, X-ray fluorescence analysis (XRF) and inductively coupled plasma atomic emission spectroscopy (ICP-OES) were applied (refer to **Table 1**). Discrepancy in the values for the respective concentrations of Mn, Na, W and Si may correlate with the sensitivity of the methods as well the corresponding sample preparation (fluxing digestion/dissolution). In the case of XRF, the analysis of lighter elements such Na is limited to the upper layers of the sample in presence of a heavier matrix such as W. Thus, precise quantitative analysis of light elements in the bulk was not possible here. The results of the ICP-OES were more accurate for Na. In general, the determined catalyst composition is sufficiently close to the desired nominal composition. A minor impurity in form of S was observed.

Table 1: Catalyst composition as determined by XRF analysis and ICP-OES.

Element	Nominal Composition [wt%]	Concentration (XRF) [wt%]	Concentration (ICP-TUB) [wt%]	Concentration (ICP-FHI) [wt%]
Mn	2.00	2.14 ± 0.01	1.77 ± 0.12	1.94
Na	0.70	1.33 ± 0.06	0.62 ± 0.02	0.65
W	2.82	2.70 ± 0.02	2.57 ± 0.11	/
Si	44.17	42.79 ± 0.16	40.11 ± 1.33	/

4.1.2 Powder X-ray diffraction

The XRD results for the ground Mn-Na_2WO_4/SiO_2 catalyst at room temperature are given in **Figure 6**. A high degree of crystallinity was observed for the α-cristobalite support, which is formed from amorphous silica during calcination. Traces of the thermodynamically more favoured quartz phase were also present. The coating or active phase mainly consisted of Na_2WO_4 and mixed-valent Mn_7SiO_{12} (braunite, $Mn^{2+}Mn^{3+}{}_6SiO_{12}$). Quantitative analysis revealed the catalyst to be constituted by 92.01 wt% α-cristobalite, 0.49 wt% quartz, 4.11 wt% Na_2WO_4 and 3.38 wt% Mn_7SiO_{12}.

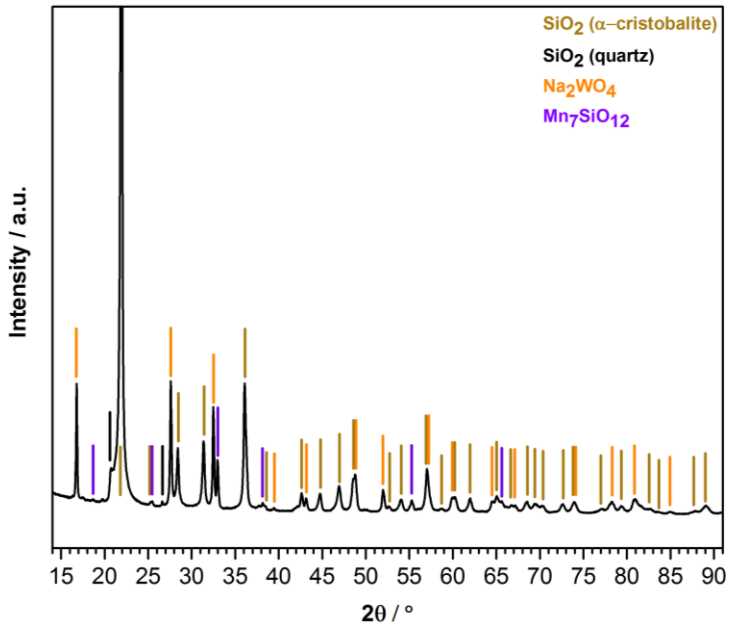

Figure 6: X-ray diffraction pattern of mortared Mn-Na_2WO_4/SiO_2 at room temperature.

4.1.3 *Ex situ* resonance Raman spectroscopy

Raman spectroscopy can function as a sensitive tool in investigating structural transitions and interactions in compounds. Phases or species that are only formed under reaction conditions or in low concentrations may be discernible using this characterization method.

The mortared Mn-Na_2WO_4/SiO_2 catalyst was analysed at nine different wavelengths, as can be seen in **Figure 7**. This multi-wavelength approach was chosen to target resonance effects in a systematic manner. The highest resonance enhancement of bands originating from supported Mn_7SiO_{12} (*e.g.*: 470−710 cm^{-1})

and Na_2WO_4 (*e.g.*: 905−950 cm^{-1}) phases was observed with visible light lasers. In case of the 457 nm laser, the Raman bands of the α-cristobalite support at 234 cm^{-1} and 419 cm^{-1} were partly supressed. Hence, this laser was chosen as excitation source for further experiments.

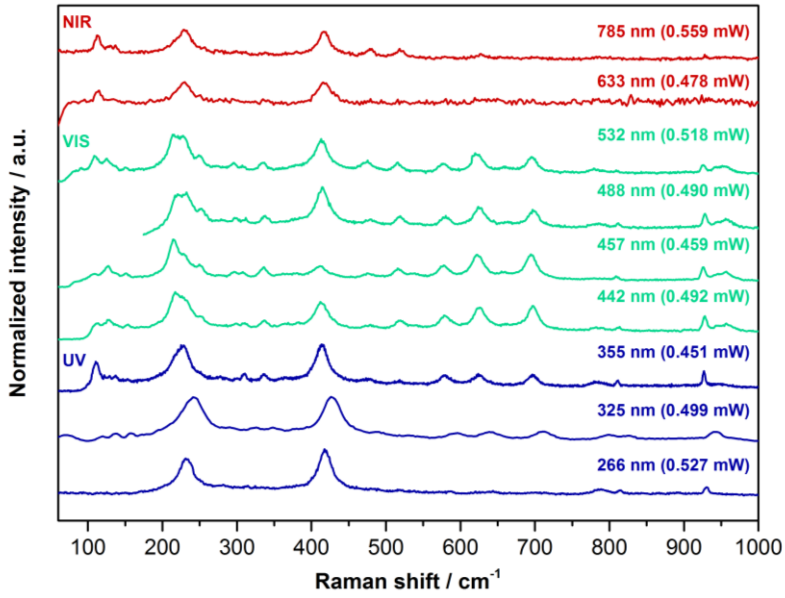

Figure 7: Multi-wavelength Raman spectroscopy of Mn-Na_2WO_4/SiO_2 recorded at 22 °C (*ex situ*, exposure time = 5 min).

Figure 8 shows a detailed allocation of bands to the respective phases present in the catalyst, based on literature[22, 30] and reference measurements. While the α-cristobalite support produces six peaks at 116, 281, 287, 419, 784, 997 and 1079 cm^{-1} respectively, the Mn_7SiO_{12} phase is responsible for a much larger group of bands – the most notable modes appearing at 223, 340, 478, 521, 584, 628 and 702 cm^{-1}. Bands indicating the Na_2WO_4 phase are visible at 87, 312, 814 and 930 cm^{-1}, with the 930 cm^{-1} band possessing the highest intensity. This is in agreement with the findings of Wu *et al*. for the Na_2WO_4/SiO_2 system.[30i] Finally, another phase in form of $MnWO_4$ was identified, with two bands appearing at 131 cm^{-1} and 887 cm^{-1} respectively. As this phase was not detected by XRD, it is likely to exist in relatively low concentrations or in X-ray amorphous form. The low concentration could also be associated with the higher stability of mixed valent Mn_7SiO_{12} ($Mn^{2+}Mn^{3+}{}_6SiO_{12}$) under oxidising conditions, in which Mn can predominantly exist in a higher oxidation state (Mn).

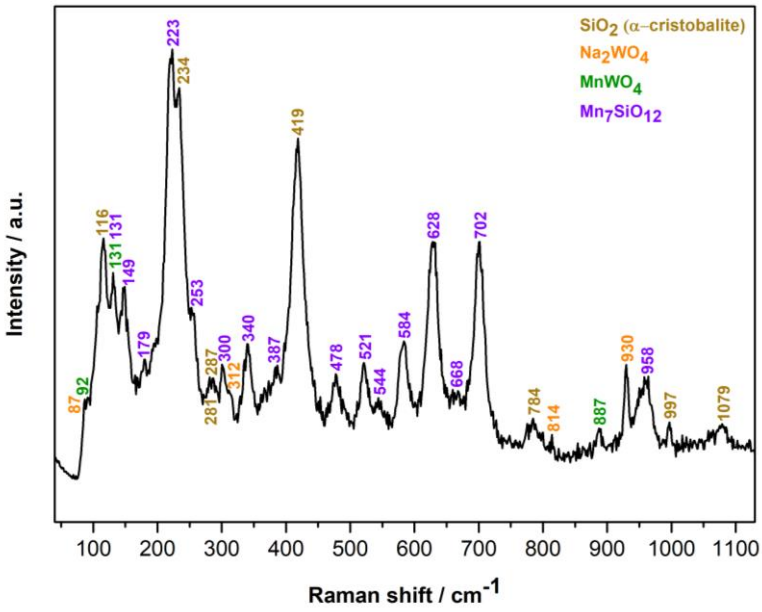

Figure 8: *In-situ* Raman spectrum of the Mn-Na_2WO_4/SiO_2 catalyst recorded at 457 nm (He:O_2 = 79:21, total flow = 10 mL/min, 22 °C, exposure time = 10 min).

To estimate the chances of inducing laser damage to the Mn-Na_2WO_4/SiO_2 catalyst system, spectra were recorded at increased laser power and exposure time (refer to **Figure 9**). The catalyst displayed high stability throughout. Thereupon, a laser power of 0.459 mW was chosen for all spectroscopic measurements.

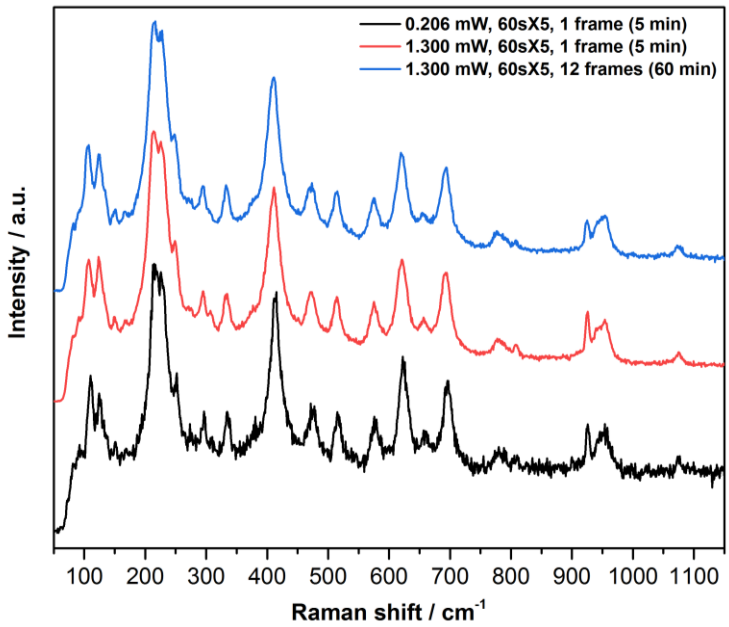

Figure 9: High catalyst stability as indicated by the absence of laser damage after applying a prolonged exposure time and high laser power (457 nm, 23 °C).

4.1.4 Scanning electron microscopy and energy dispersive X-ray analysis (SEM-EDX)

On a macroscopic level, SEM revealed that the Mn-Na_2WO_4/SiO_2 catalyst exists in coarse, irregularly shaped granules in µm dimensions, which already suggests inhomogeneity (refer to **Figure 10**). The surface morphology of these coated SiO_2 granules was further examined at higher magnifications (refer to **Figure 11**).

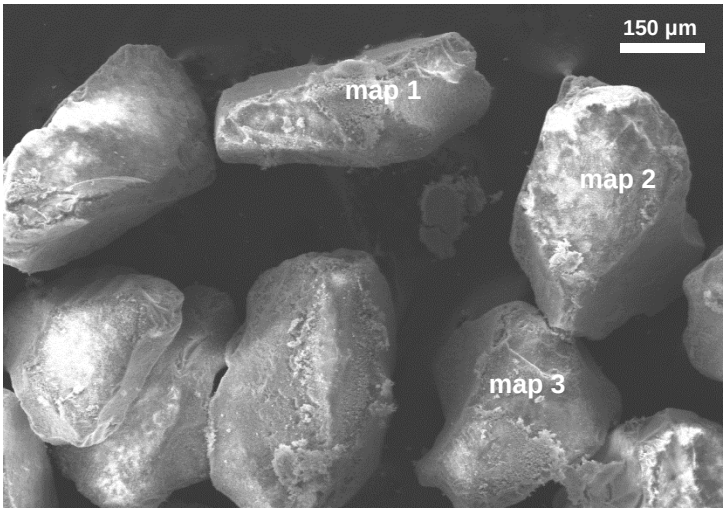

Figure 10: SEM image of Mn-Na_2WO_4/SiO_2 catalyst particles taken at a magnification of x100, an acceleration voltage of 20.0 kV and a working distance of 10.0 mm. The three marked areas were selected for EDX mapping.

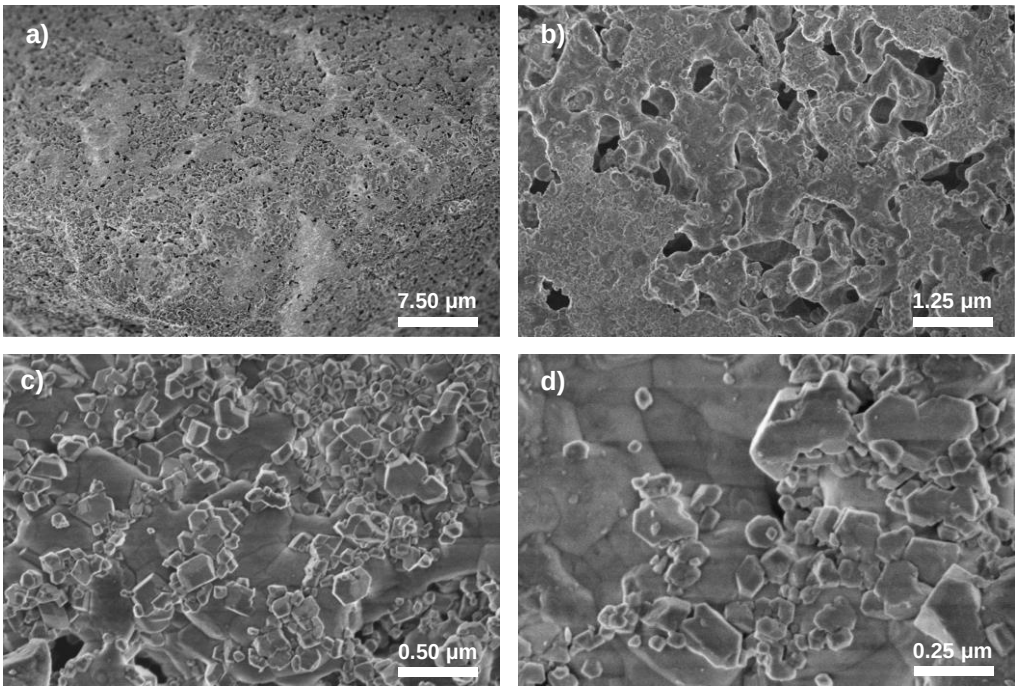

Figure 11: SEM images of Mn-Na_2WO_4/SiO_2 taken at a magnification of x1.5k (a), x5.0k (b), x10.0k (c) and x25.0k (d), an acceleration voltage of 1.5 kV and a working distance of 3.0 mm.

The corresponding images show that the surface layer of the support is inhomogeneously covered by glass-like domains of coating. Based on the results of the XRD measurements, it can be assumed that these are largely constituted by crystalline Na-, Mn- and W-containing phases. The presence of X-ray amorphous forms also seems plausible in lower quantities, with the SEM images revealing areas, where the crystallinity was not unambiguous.

To gain better insight into the elemental distribution on the surface of the catalyst, five spots were selected for elemental mapping via energy dispersive X-ray analysis (**map 1−5**, refer to **Figure 10** for **map 1−3** position, refer to **Figure 65** for spectra). The fluctuation of the values for the individual elements underlines the inhomogeneous distribution of active phase/s on the support (refer to **Table 2**). In the case of W, significantly lower values were obtained via EDX in comparison to XRF and ICP-OES. This might correlate with a lower surface and subsurface concentration of W in comparison to Na and Mn. As an acceleration voltage of 20 kV leads to a sufficient penetration depth, W may be principally occupying the bulk regions of the supported catalyst. It is also to be noted, however, that EDX mapping delivers local information of the catalyst surface and is, thus, not to be interpreted as representative for the entire catalyst.

Table 2: Concentration of elements in at% collected for five different areas of the catalyst via EDX (acceleration voltage: 20 kV, magnification: x1.0k, working distance: 10 mm, average interaction depth: 2.8 µm).

Element	C	O	Na	Si	Mn	W
Map 1	35.43	43.22	0.67	17.95	2.35	0.38
Map 2	15.69	65.50	0.84	14.82	2.63	0.52
Map 3	37.76	45.29	0.28	14.73	1.72	0.20
Map 4	20.82	59.08	1.59	15.17	2.52	0.82
Map 5	24.36	53.37	0.82	17.55	3.52	0.39
Mean	26.81	53.29	0.84	16.04	2.55	0.47
σ	9.48	9.33	0.48	1.58	0.65	0.22

The SE images and elemental maps of three selected areas (**map 1−3**, refer to **Figure 10**) have been displayed here for discussion (refer to **Figure 12**). Both clearly demonstrate the inhomogeneity of the catalyst coating, with Na_2WO_4 preferentially forming separate domains. Mn and W cover large areas of the catalyst surface but also in relatively inhomogeneous dispersion. Higher concentrations of Mn in close vicinity to the Na_2WO_4 phase, as seen in both maps, may suggest a structural interaction of the Mn-containing phases (Mn_7SiO_{12}, possibly MnO_x/SiO_2 species) with Na_2WO_4. Freely existing W can also be

observed, suggestive of a WO_x/SiO_2 species. The presence of Na in the α-cristobalite support could not be verified due to background noise. Further maps can be found in the appendix (**maps 1** and **2**: refer to **Figure 64**).

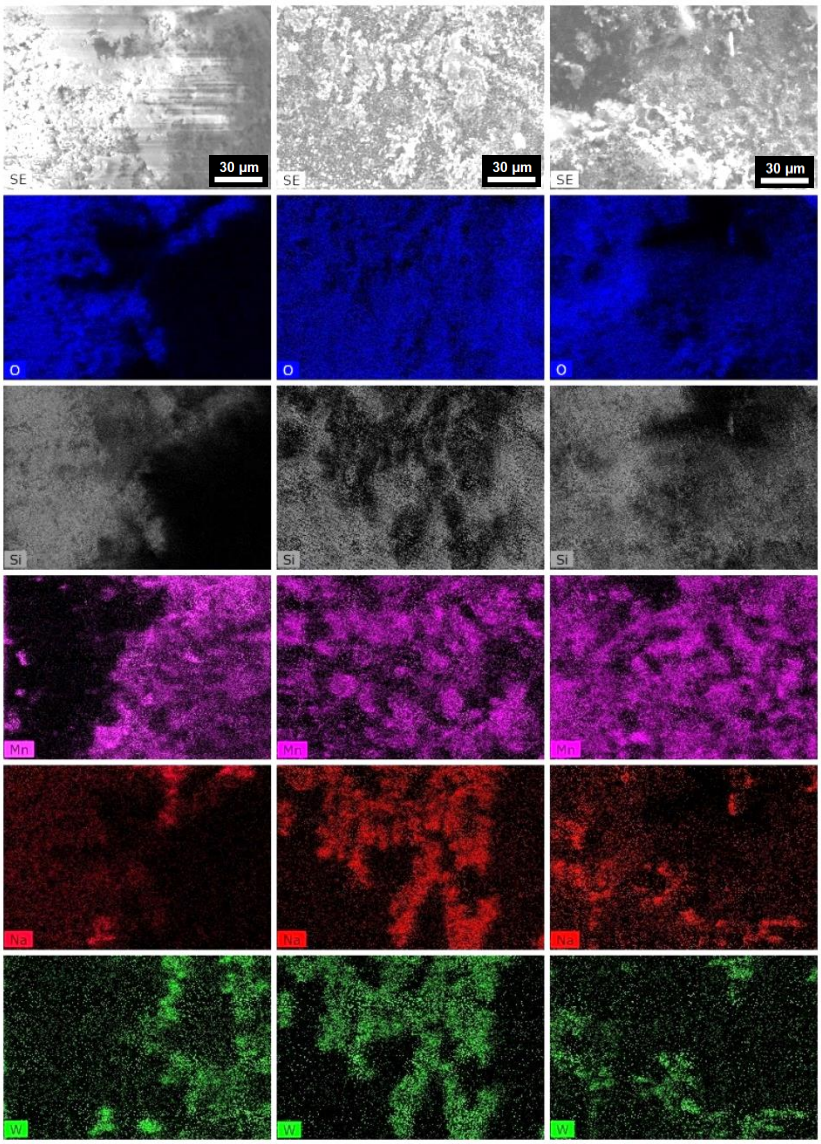

Figure 12: SE images and EDX mapping of O, Si, Mn, Na and W for three selected catalyst areas (maps 1-3 arranged from left to right; acceleration voltage: 20 kV, magnification: x1.0k, working distance: 10 mm, average interaction depth: 2.8 µm). The SE image of map 1 indicates strong charging of the SiO_2 support.

4.1.5 N_2-physisorption (BET method)

A relatively low surface area of S_{BET} = 2.9 m²/g was experimentally determined for the Mn-Na_2WO_4/SiO_2 catalyst (refer to **Figure 13**), which is in compliance with the results of Simon *et al*. (S_{BET} = 2.71 ± 0.08 m²/g)[12d]. The slight deviation could be explained by the limited amount of catalyst (53.7 mg) that was used for characterization. Furthermore, the catalyst barely contains micro- or mesopores

based on the hysteresis of the recorded adsorption/desorption isotherm and can be classified as a largely macroporous system.

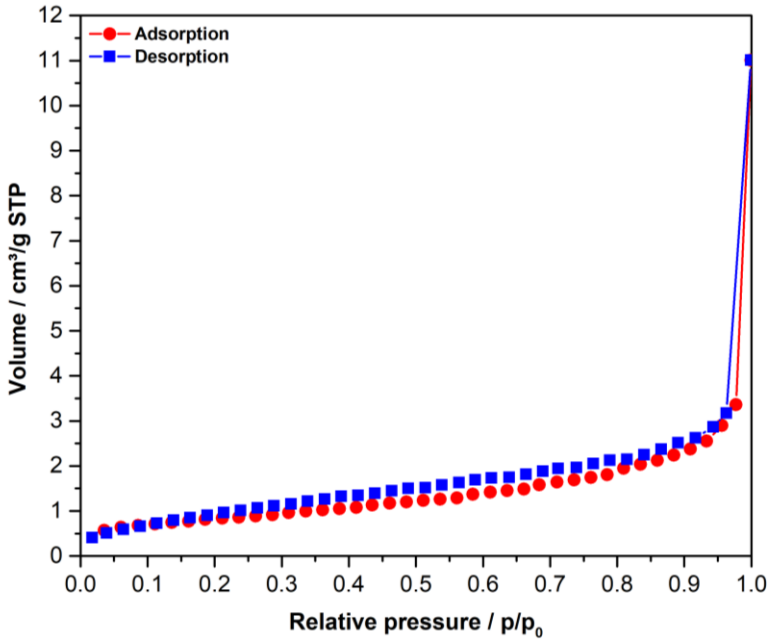

Figure 13: N_2-adsorption/desorption isotherm for the Mn-Na_2WO_4/SiO_2 catalyst.

4.2 Thermal behaviour of the Mn-Na_2WO_4/SiO_2 catalyst

The Mn-Na_2WO_4/SiO_2 catalyst, together with three relevant reference samples in form of pure Na_2WO_4 and $MnWO_4$ as well as natural Mn_7SiO_{12}, were subjected to thermogravimetry (TG) and differential scanning calorimetry (DSC) or differential thermal analysis (DTA) measurements.

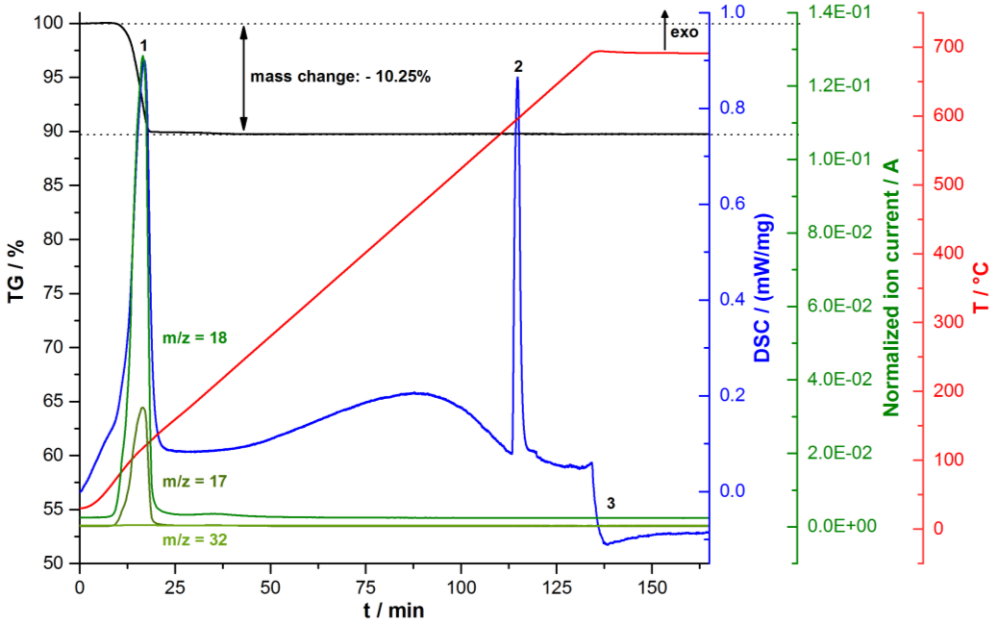

Figure 14: TG-DSC-MS of $Na_2WO_4 \cdot 2H_2O$ in Ar (100 mL/min). The sample was subjected to a heating rate of 5 °C/min to reach a maximum temperature of 700 °C. MS signal intensities were normalized to the carrier gas Ar (m/z = 40).

Figure 14 displays the thermal behaviour of $Na_2WO_4 \cdot 2H_2O$ (34.6 mg) until 700 °C, which is responsible for three significant events. At 117 °C (**1**), dehydration of the sample is indicated by the evolution of water (m/z = 17, m/z = 18). At 596 °C, another exothermic peak, attributed towards the first order phase transition of Na_2WO_4 from a cubic to an orthorhombic crystal system (**2**), occurred.[30f, 31] Lastly, the endothermic peak at 694 °C (**3**) represents the melting of Na_2WO_4.[31] No significant oxygen evolution was detected for this process. The mass loss of 10.25% (3.55 mg) is mainly caused by the release of water.

The TG-DSC-MS data for Mn_7SiO_{12} (17.6 mg) can be seen in **Figure 15**. H_2O (m/z = 17, m/z = 18), O_2 (m/z = 32) and CO_2 (m/z = 44) were released at the beginning of the heating ramp at 99 °C (**1−4**). With the sample being of natural origin and containing traces of calcite ($CaCO_3$), the release of CO_2 at approximately 348 °C (**5**) and 574 °C (**6**) can be attributed to the decomposition of this phase.

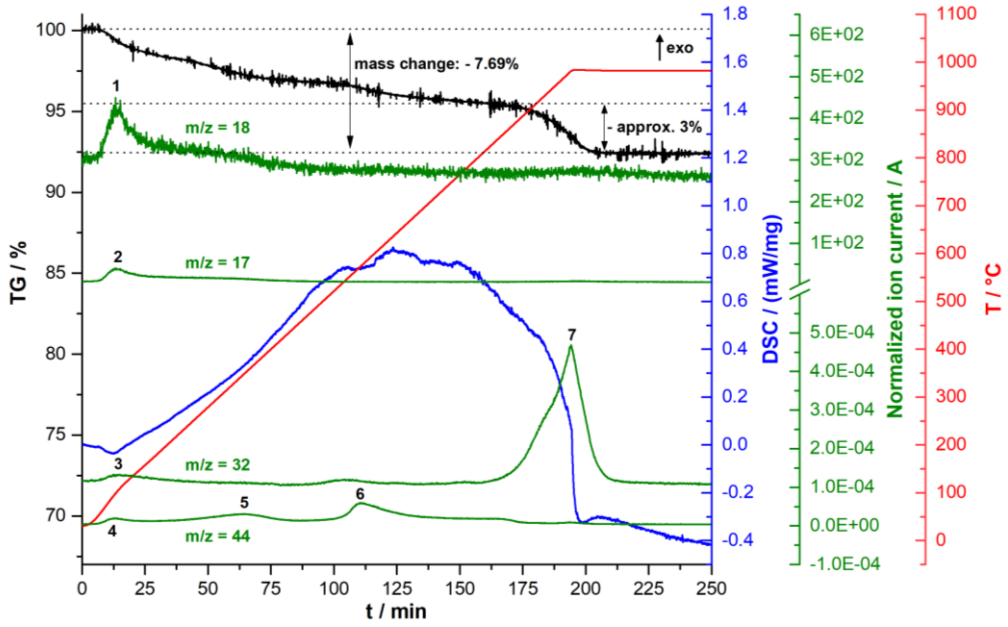

Figure 15: TG-DSC-MS of Mn_7SiO_{12} in Ar (100 mL/min). The sample was subjected to a heating rate of 5 °C/min to reach a maximum temperature of 1000 °C. MS signal intensities were normalized to the carrier gas Ar (m/z = 40).

A relatively pronounced loss of oxygen was also observed from approximately 800 °C onwards (**7**, maximum at 981 °C). A total mass change of 7.69% (1.35 mg) was detected, with the oxygen release above 800 °C accounting for roughly 3% (0.53 mg). With 17.6 mg of Mn_7SiO_{12} theoretically containing 5.56 mg O_2, the O_2 release is very likely connected to the Mn_7SiO_{12} phase.

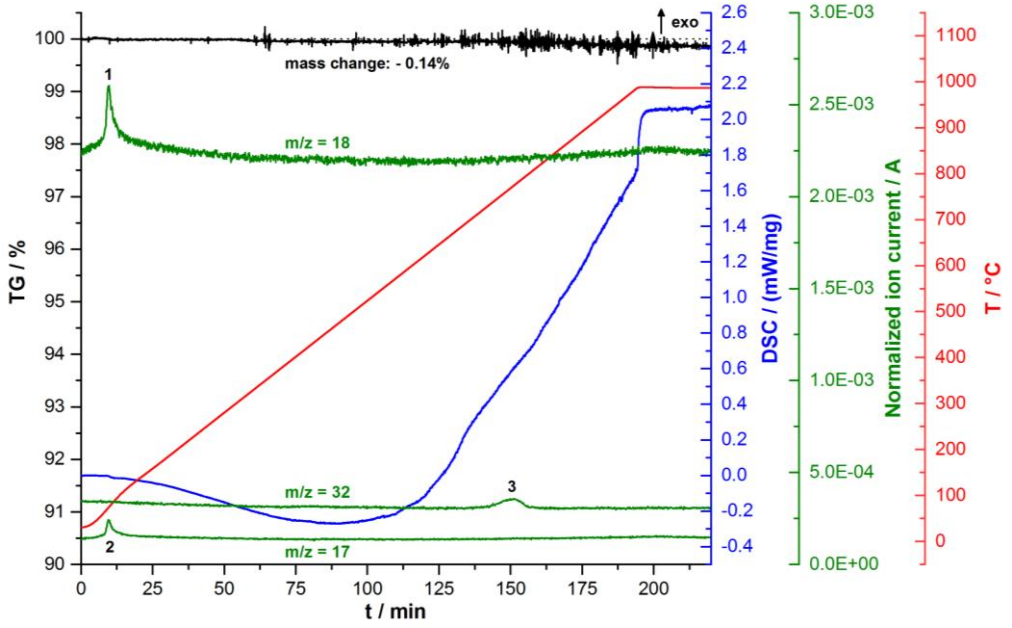

Figure 16: TG-DSC-MS of $MnWO_4$ in Ar (100 mL/min). The sample was subjected to a heating rate of 5 °C/min to reach a maximum temperature of 1000 °C. MS signal intensities were normalized to the carrier gas Ar (m/z = 40).

The TG-DSC-MS measurement for $MnWO_4$ (31.2 mg) is given in **Figure 16**. Overall, no significant change to the mass of the sample was observed. Residual water was desorbed from the surface at 74 °C, as indicated by the MS signals for H_2O (m/z = 18, **1**) and OH (m/z = 17, **2**). An evolution of oxygen was also detected via MS (m/z = 32) in the range of 690−825 °C (maximum at 774 °C, **3**). This might be lattice oxygen that goes into the gas-phase at such high temperatures. As no phase transitions or decomposition events were detected, the mass change of 0.14% (0.04 mg) may directly correlate with the generation of oxygen defects.

The thermal behaviour of the Mn-Na_2WO_4/SiO_2 catalyst (16.5 mg) in synthetic air is demonstrated in **Figure 17**. A reversible endothermic event occurred at 225 °C (**1** and **4**), which can be attributed to the phase transition of the cristobalite support from the α- to the β-modification.[30a, 30d, 32] Another endothermic peak was observed at 778 °C (**2**), which seems to correlate with the exothermic peak at 453 °C (**3**). Both could represent phase changes, catalyst decomposition or recrystallization events. The MS data, however, gave no indication of O_2 (m/z = 32), H_2O (m/z = 17 and m/z = 18) or CO_2 (m/z = 44) being formed. Furthermore, no significant mass change was observed.

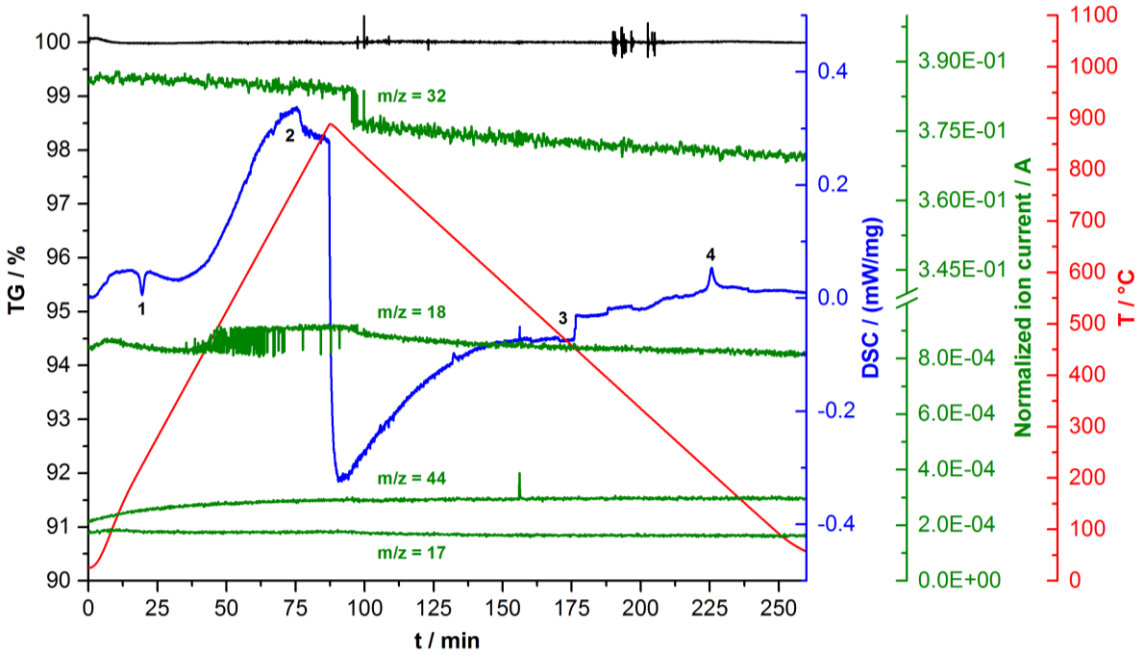

Figure 17: TG-DSC-MS of the Mn-Na_2WO_4/SiO_2 catalyst in synthetic air (Ar:O_2 = 79:21, total flow rate = 100 mL/min). The sample was subjected to a heating rate of 10 °C/min to reach a temperature of 900 °C. After reaching the maximum temperature, the sample was cooled to 30 °C at a cooling rate of 5 °C/min. MS signal intensities were normalized to the carrier gas Ar (m/z = 40).

The measurement was repeated in Ar with a larger amount of sample (104.5 mg) (refer to **Figure 18**). The corresponding DTA curve features an endothermic event

at 215−217°C (**1**), which is assigned to the phase transition of the cristobalite support.[30a, 30d, 32] While no evolution of CO_2 (m/z = 44) was detected, a limited amount of H_2O (m/z = 18) was formed at the beginning of the heating procedure. It can be assumed that a relatively clean surface was formed after pre-treatment. A prolonged release of water (m/z = 18) is observed at 515−579 °C (**2**) (maximum at 535 °C). This event, however, does not appear in the curves of the reference samples. Two peaks, indicating oxygen evolution (m/z = 32), were also observed. The first peak (**3**), with an onset at 653°C and maximum at 680 °C, could be linked to the phase transition of Na_2WO_4 from solid to liquid (m.p. = 695 °C). The phase transition may induce structural changes, rearrangements and/or even dissolution of the remaining supported phases, thus releasing oxygen.

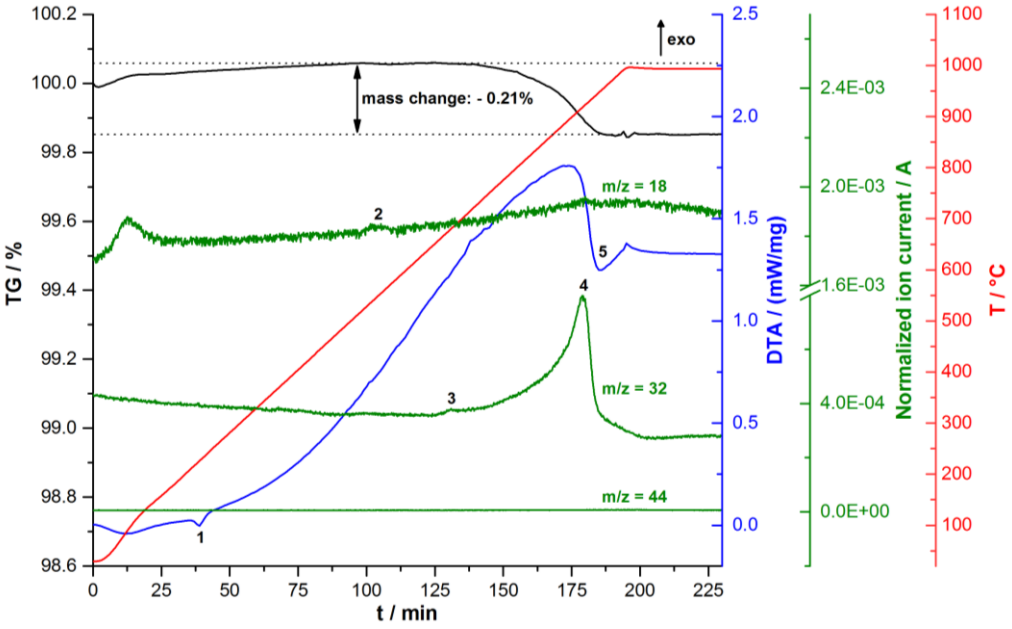

Figure 18: TG-DTA-MS of the Mn-Na_2WO_4/SiO_2 catalyst in Ar (70 mL/min). The sample was subjected to a heating rate of 5 °C/min to reach a maximum temperature of 1000 °C. MS signal intensities were normalized to the carrier gas Ar (m/z = 40).

The slight deviation in temperature, compared to the melting point of the pure substance, might be explained by the dispersion of Na_2WO_4 on the support, together with other species. Contrary to the MS signal (m/z = 32), that can be interpreted as indication of a partial phase transition, the DTA curve (blue) displays irregularities in the relevant temperature regime instead of a well-defined endothermic peak. It is likely that only a limited amount of the surface species undergoes phase transition, with DTA lacking the sensitivity for a successful detection in this case. The alternative scenario of Na_2WO_4 not melting, due to strong interactions with the support, must also be considered. The second peak

(maximum at 918 °C, **4**) covers a much broader temperature range of approximately 200 °C (onset overlaps with event **3** at approximately 680 °C). A weight loss of 0.21% (0.22 mg) was caused by the event, with the DTA curve indicating endothermicity (**5**). While the peak most likely arises from the decomposition of phases present on the catalyst, which only remains stable until 750 °C, it could additionally represent a gradual release of oxygen from the two supported phases at higher temperatures. According to the nominal composition of the catalyst, both Na_2WO_4 and Mn_7SiO_{12} can release a maximum of 1.02 mg and 1.04 mg O_2 respectively for 104.5 mg of the catalyst. As seen in **Figure 19**, both phases produce gas-phase oxygen in a temperature regime similar to that of the catalyst. With pure Mn_7SiO_{12} featuring a similarly broad and intense peak at 981 °C, it is proposed to contribute strongly towards the release of O_2 (**4**) in the catalyst. The shift in temperature for this event may correlate with the fact that Mn_7SiO_{12} (3.29 mg according to nominal composition) exists as a supported phase in the catalyst, where structural interactions with the support and other phases influence the chemical properties of Mn_7SiO_{12}. In the case of Na_2WO_4, the two peaks in the range of 377−681 °C (**1**) and 681−909 °C (**2**) may be representative for the above-mentioned phase transitions from cubic to orthorhombic and from solid to liquid. The liquefaction may additionally improve oxygen mobility in the upper catalyst layers.

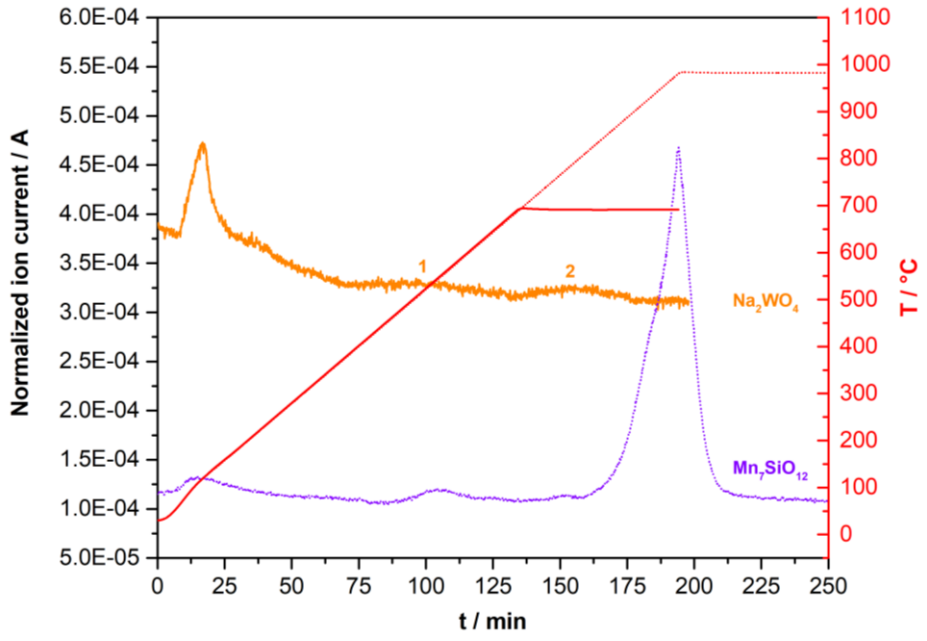

Figure 19: Time-dependent O_2-evolution (m/z = 32) for $Na_2WO_4 \cdot 2H_2O$ (34.6 mg, orange) and Mn_7SiO_{12} (17.6 mg, purple) as recorded via MS. The intensities were normalized to the carrier gas Ar (m/z = 40). The MS data as well as the temperature profiles (red) were taken from the respective measurements.

4.3 Catalytic activity testing

The catalytic activity of the system in the temperature range of 700−750 °C is given in **Figure 20**. A maximum C_2-yield of 3.1% was observed at 750 °C for a co-feed of CH_4, O_2 and He (4:1:4). C_2H_6 was formed in higher selectivity than C_2H_4.The curves for the selectivity of C_2H_6 and C_2H_4 also suggest that the formation of both products equilibrates at higher conversions. Only a minor percentage of methane was converted to propane. The main by-products formed were CO and CO_2 (refer to **Figure 21**). Testing was not performed above 750 °C to avoid catalyst decomposition.

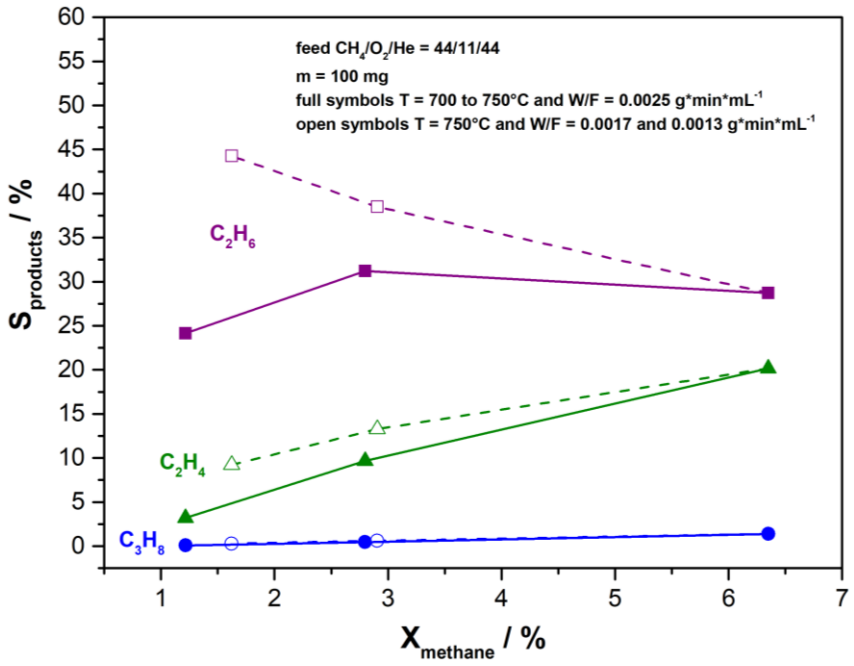

Figure 20: Performance of the Mn-Na_2WO_4/SiO_2 catalyst in the oxidative coupling of methane. A contact time variation was performed at 750 °C.

Increasing the flow rate stepwise from 40 mL/min (W/F = 0.0025 g*min*mL^{-1}) to 60 mL/min (W/F = 0.0017 g*min*mL^{-1}) and 80 mL/min (W/F = 0.0013 g*min*mL^{-1}) at a constant temperature of 750 °C led to a subsequent gain in C_2-selectivity, but, concurrently, a decreased conversion. The opposing selectivity trends for C_2H_6 and C_2H_4 at higher flow rates are representative for a consecutive reaction network, in which ethane dehydrogenates to yield ethene.

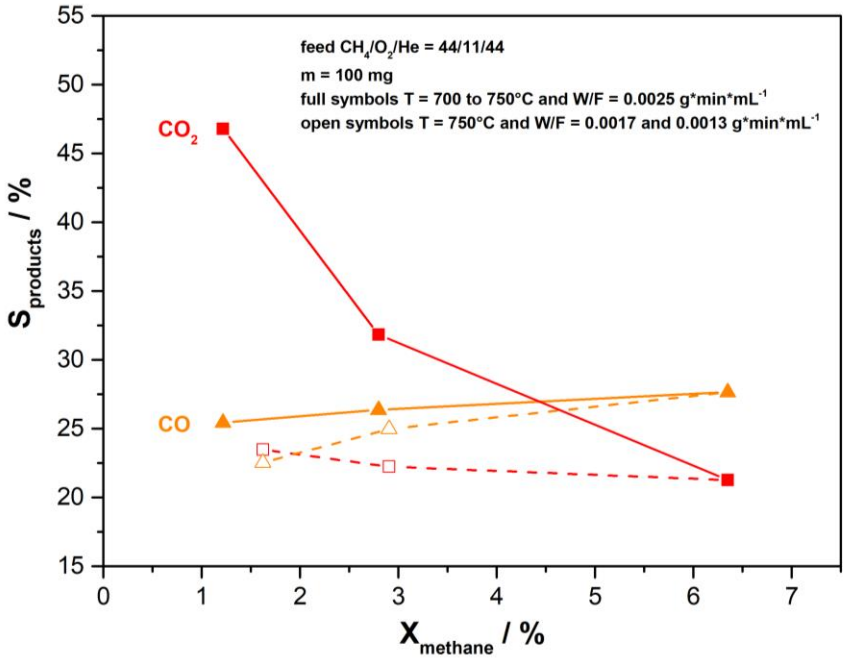

Figure 21: Selectivity of the Mn-Na_2WO_4/SiO_2 catalyst for CO and CO_2 *versus* the conversion of methane. A contact time variation was performed at 750 °C.

The activity maximum at 750 °C is in agreement with experiments by Simon *et al*.[12d]. At W/F = 0.0025 g*min*mL^{-1}, the research group observed X(CH_4) = 7% and S(C_2) = 76% under analogous conditions (T = 750 °C, CH_4:O_2:He = 4:1:4). The here studied catalyst was less selective in comparison, with X(CH_4) = 6% and S(C_2) = 49% observed. This may be attributed to the additional dilution with quartz sand that was applied by Simon *et al*.. In order to enable a better comparison with the *operando* Raman experiments, the catalyst was used in an undiluted state. By analysis of the collected catalytic data, suitable reaction conditions for *in-situ* and *operando* Raman spectroscopy experiments were identified. To reach a sufficient conversion, a W/F ratio of 0.0025 g*min*mL^{-1} or higher should be maintained. Furthermore, a reaction temperature of 750 °C should be targeted for maximum catalyst activity.

Figure 22 shows the XRD patterns of the fresh and the spent catalyst from catalyst testing experiment as discussed above. Major reflections belonging to α-cristobalite and quartz are discernible for the latter. Thus, a portion of the support underwent phase transition from α-cristobalite to quartz during the reaction. The reflections of the α-cristobalite support are also more intense for the used catalyst, indicating more pronounced crystallinity. The reflections for the Na_2WO_4 phase, on the other hand, seem to have decreased in intensity. There are different scenarios

that can account for this. It may either have formed smaller crystallites that go undetected by XRD or may have been transformed into an amorphous state. Since the melting point of Na_2WO_4 (m.p. = 695 °C) is below the reaction temperature, it may have also reacted to form a different phase while the Na^+ ions migrate into the support. Thus, a direct involvement not only in the catalysis but also in the re-crystallization of the support is plausible. Quantitative phase analysis showed that the catalyst contained 89.82 wt% α-cristobalite, 3.21 wt% quartz, 3.88 wt% Na_2WO_4 and 3.09 wt% Mn_7SiO_{12}, thus confirming a slight decrease in the concentrations of Na_2WO_4 and Mn_7SiO_{12} after reaction. No $MnWO_4$ was detected.

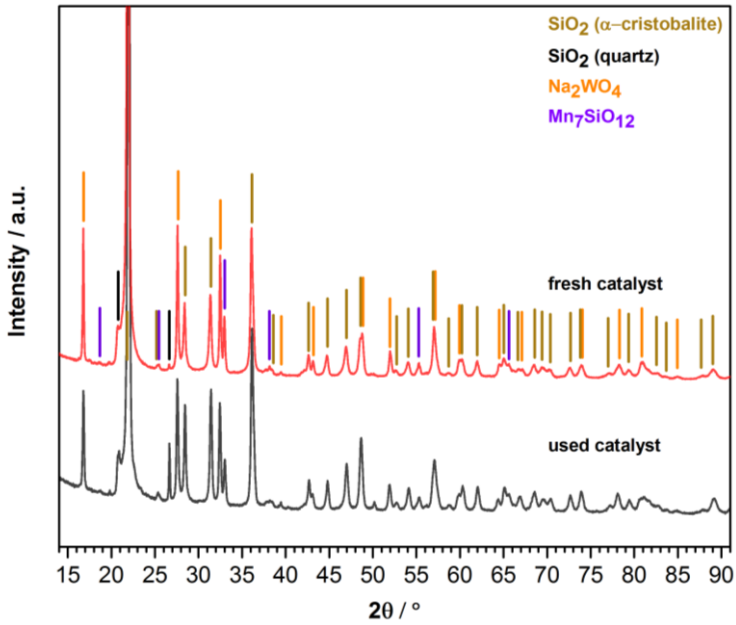

Figure 22: XRD of Mn-Na_2WO_4/SiO_2 before (red) and after reaction (black).

4.4 Characterization of the Mn-Na_2WO_4/SiO_2 catalyst under reaction conditions

4.4.1 High temperature *in-situ* XRD analysis

Initially, an *operando* approach involving different ratios of CH_4:O_2:He was attempted. An almost quantitative conversion of both methane and oxygen was observed. Henceforth, *in-situ* XRD experiments were conducted under oxidizing and reducing conditions. The results thereof are not entirely representative of the catalyst under reaction conditions but do serve as an approximation of its working state.

Oxidizing conditions

The experiment under oxidizing conditions was performed using a feed of O_2:He = 1:8 at a total flow rate of 20 mLn/min. 64.0 mg of catalyst were placed in the sample holder. Thus, both the W/F ratio (0.0032 g*min*mLn^{-1}) as well as the partial pressure of oxygen in the feed were similar to those chosen for catalytic testing.

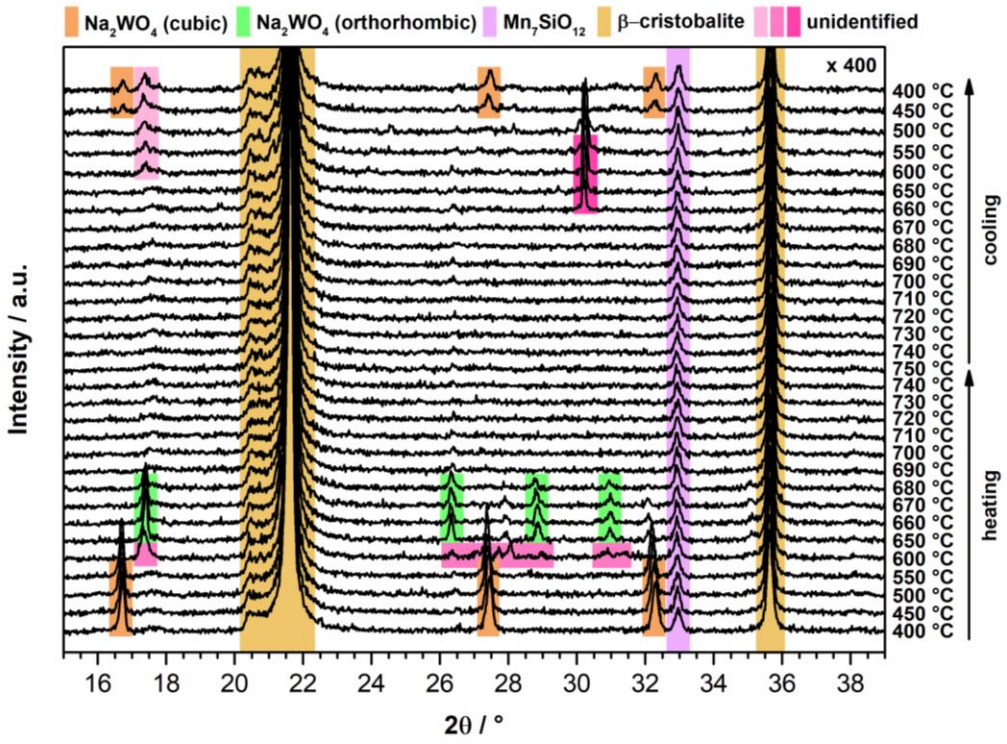

Figure 23: In-situ XRD of the Mn-Na_2WO_4/SiO_2 catalyst under oxidizing conditions (O_2:He = 1:8, 20 mLn/min, W/F = 0.0032 g*min*mLn-1).

As seen in **Figure 23**, both the β-cristobalite support and Mn_7SiO_{12} did not undergo structural changes in the temperature range of 400−750 °C, as indicated by their relatively constant peak intensities. The Na_2WO_4 phase, on the other hand, displayed significant structural dynamics. At 600 °C (heating-phase), the reflections of cubic Na_2WO_4 were replaced by an unidentified phase, which seems to form during the transition to orthorhombic Na_2WO_4, which is first observed at 650 °C. This orthorhombic Na_2WO_4 remained stable until 680 °C. Further heating resulted in a drastic intensity loss of the respective reflections, which is suggestive of a liquefaction of the Na_2WO_4 phase. During cooling, two unidentified phases were formed between 660−550 °C and 600 °C−RT. The latter maybe be associated with orthorhombic Na_2WO_4 due to the position of the reflection. Cubic Na_2WO_4 was reformed at 450 °C.

Similar results were reported by Hou *et al*..[28] The group observed a weakening of the reflections for Na_2WO_4 in air from 500 °C onwards and a complete disappearance at 700 °C, suggesting a deformation of its lattice structure close to its melting point (695 °C). The diffraction signals for Mn_2O_3, on the other hand, remained stable.

Reducing conditions

Analogous to the experiment performed under oxidizing conditions, the feed composition and flow rate were chosen to match the reaction conditions during catalyst testing (CH_4:Ar = 4:5, total flow rate = 20 mLn/min, 64.2 mg catalyst, W/F = 0.0032 g*min*mLn^{-1}). **Figure 24** shows the XRD patterns of the Mn-Na_2WO_4/SiO_2 catalyst in the temperature range of 400−700 °C. The reflections of the β-cristobalite support did not change with temperature. In contrast to the measurement under oxidizing conditions, a disappearance of Mn_7SiO_{12} was observed when heating to 600 °C. Concurrently, several reflections belonging to $MnWO_4$ were detected. This phase, however, was not found at any other temperature. Cubic Na_2WO_4 was only present at 400 °C and 500 °C (heating-phase). No reformation was observed during cooling. The disappearance of its reflections at 600 °C is most likely connected to its phase transition from a cubic to an orthorhombic system. Additionally, a partial conversion of this phase to $MnWO_4$ by reaction with Mn_7SiO_{12} must be considered due to the absence of reflections originating from orthorhombic Na_2WO_4 at 600 °C. A phase showing

resemblance to orthorhombic Na_2WO_4 is, however, detected between 600 °C and 400 °C during cooling, albeit in low concentration. Phase analysis of the spent catalyst showed it to be constituted 95.10 wt% α-cristobalite, 1.04 wt% quartz, 1.76 wt% W, 1.05 wt% hexagonal W_2C and 1.05 wt% Mn_2SiO_4. Based on this, a strong reduction and partial decomposition of the catalyst can be assumed.

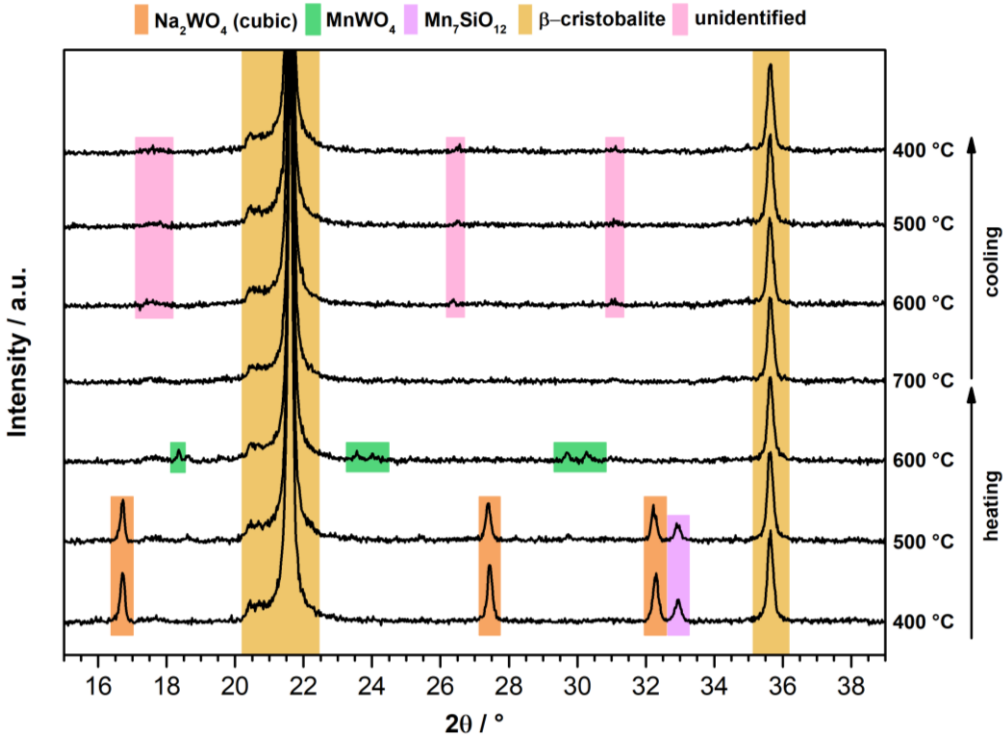

Figure 24: In-situ XRD of Mn-Na_2WO_4/SiO_2 under reducing conditions (CH_4:He = 4:5, 20 mLn/min, W/F = 0.0032 g*min*mLn-1).

The reduction of the Mn_7SiO_{12} phase to yield $MnWO_4$ was also observed by Hou and co-workers, who were successful in demonstrating the reversibility of this transition.[28] XPS and H_2-TPR data showed that a redox cycle between Mn^{2+} and $Mn^{\delta+}$ ($2 \leq \delta < 3$) may take place under reaction conditions. The structural stability of the $MnWO_4$ phase may also be influenced by the liquefaction of Na_2WO_4.

4.4.2 *In-situ* and *operando* resonance Raman spectroscopy

Pure sodium tungsten oxide dihydrate ($Na_2WO_4 \cdot 2H_2O$) and manganese tungsten oxide ($MnWO_4$) as well as natural braunite (Mn_7SiO_{12}) were analysed via high-temperature Raman spectroscopy (HTRS) at 457 nm as references to the Mn-Na_2WO_4/SiO_2 catalyst system.

The room temperature spectrum of spinel-type[33] $Na_2WO_4 \cdot 2H_2O$, as seen in **Figure 25**, contains 22 bands between 88 and 929 cm^{-1} (refer to **Table 3**). Several

bands were observed that could not be allocated based on current literature.[30e, 30f, 34] The most intense bands appeared at 311, 834 and 929 cm^{-1} respectively.

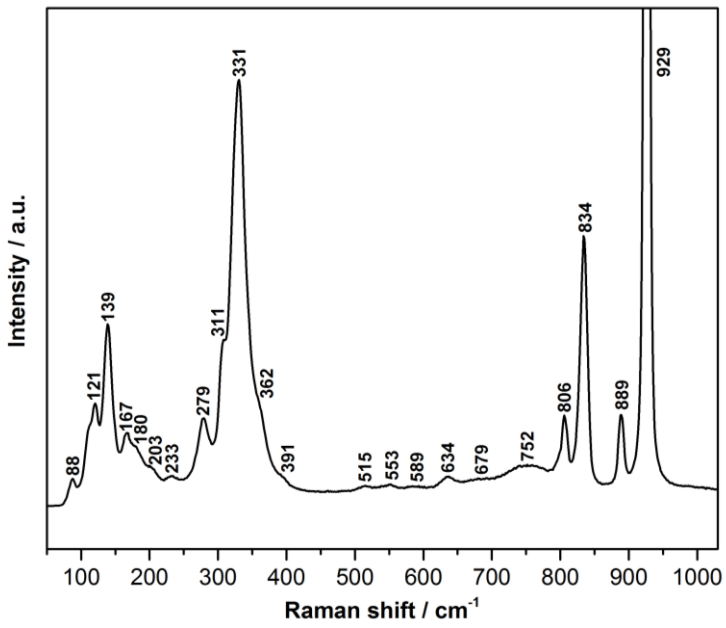

Figure 25: Raman spectrum of $Na_2WO_4 \cdot 2H_2O$ recorded 23 °C at 457 nm (exposure time = 1.5 min).

Table 3: Observed modes for the cubic $Na_2WO_4 \cdot 2H_2O$ phase at 23 °C (457 nm; L = lattice vibrations/translational mode, $\delta_{s/as}$ = symmetric/antisymmetric bending mode, $\nu_{s/as}$ = symmetric/antisymmetric stretching mode).

ω_{obs}	Mode assignment
88	L(WO_4)
121	L(WO_4)
139	unassigned
167	unassigned
180	unassigned
203	unassigned
233	unassigned
279	unassigned
311	δ_s(W–O)
331	unassigned
362	δ_{as}(W–O)
391	unassigned
515	unassigned
553	unassigned
589	unassigned
634	unassigned
679	unassigned
752	unassigned
806	ν_{as}(W–O)
834	unassigned
889	unassigned
929	ν_s(W–O)

In the high temperature Raman experiment, $Na_2WO_4 \cdot 2H_2O$ was heated in steps of approximately 100 °C from room temperature to 800 °C at 10 °C/min under the flow of synthetic air (10 mL/min).

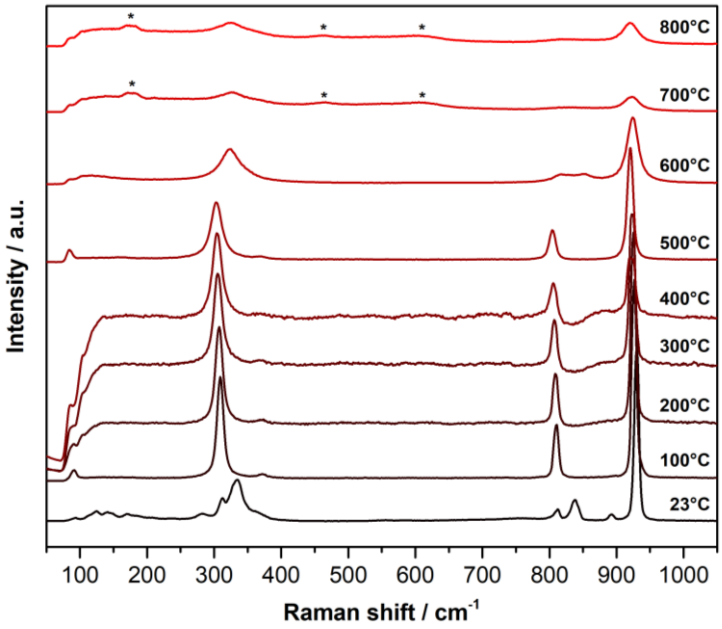

Figure 26: *In-situ* Raman spectra of $Na_2WO_4 \cdot 2H_2O$ recorded from 23 °C to 835 °C at 457 nm ($He:O_2$ = 79:21, total flow = 10 mL/min, exposure time = 1.5 min, baseline-corrected). Signals of the ceramic fiber carrier are indicated by *.

As can be seen in **Figure 26**, only five bands remained at 92, 309, 373, 811 and 926 cm^{-1} upon increasing the temperature to 100 °C. A temperature dependence of the spectra was evident. A gradually increasing bandwidth, due to the anharmonic effect introduced by temperature, and a decrease in intensity of the three main modes at 309, 811 and 926 cm^{-1} were observed. Furthermore, the bands were shifted steadily to lower wavenumbers (red shift, refer to **Figure 27**). At 600 °C, further significant changes in the Raman spectra were visible. A blue shift of the bands was seen here. This correlates with the first order phase transition of Na_2WO_4 from the cubic to the orthorhombic structure at 596 °C (TG-DSC), or as reported in literature, at 628 °C[30f]. Interestingly, a splitting of the mode at 805 cm^{-1} into two separate modes at 817 cm^{-1} and 851 cm^{-1} occurred concurrently. This has also been reported by *Lima et al.*[30f], who propose a significant distortion of the WO_4^{2-} tetrahedra and thus lowering of symmetry.The spectra recorded above the melting point of Na_2WO_4 (m.p. = 695 °C) featured a pronounced loss in intensity as well as broadening of peaks (refer to **Figure 28**). The tungstate groups are partially disordered in the liquid phase, thereby resulting in larger bandwidths

of the respective modes. All phase transitions have been observed to be reversible, as also reported in literature[30f].

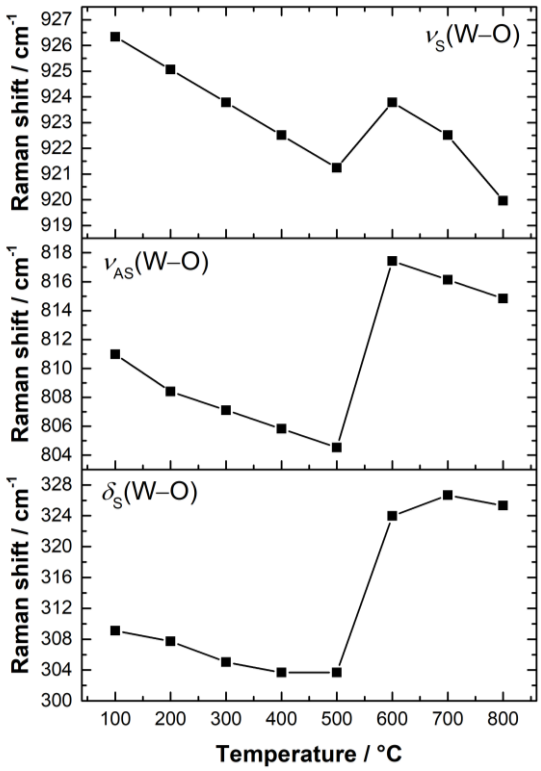

Figure 27: Temperature dependence of three selected Raman bands of $Na_2WO_4 \cdot 2H_2O$. For the mode appearing at 811 cm^{-1}, only the first band at 817 cm^{-1} was plotted after band splitting.

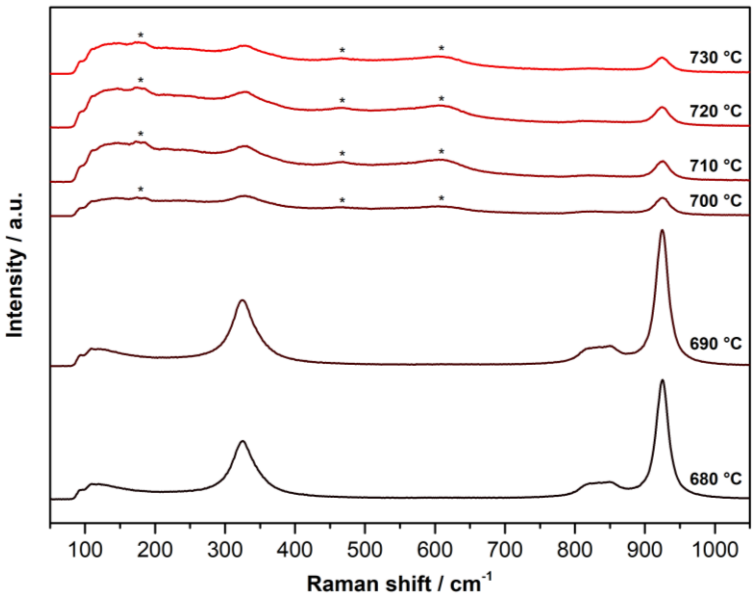

Figure 28: *In-situ* Raman spectra of $Na_2WO_4 \cdot 2H_2O$ recorded from 680 °C to 730 °C at 457 nm (N_2:O_2 = 79:21, total flow = 10 mL/min, heating rate = 10 °C/min, exposure time = 5 min). Signals of the ceramic fiber carrier are indicated by *.

An analogous experiment was performed with tetragonal[35] Mn_7SiO_{12} (refer to **Figure 29**). A total of 22 modes was detected at room temperature, including lattice vibrations, bending and stretching modes.

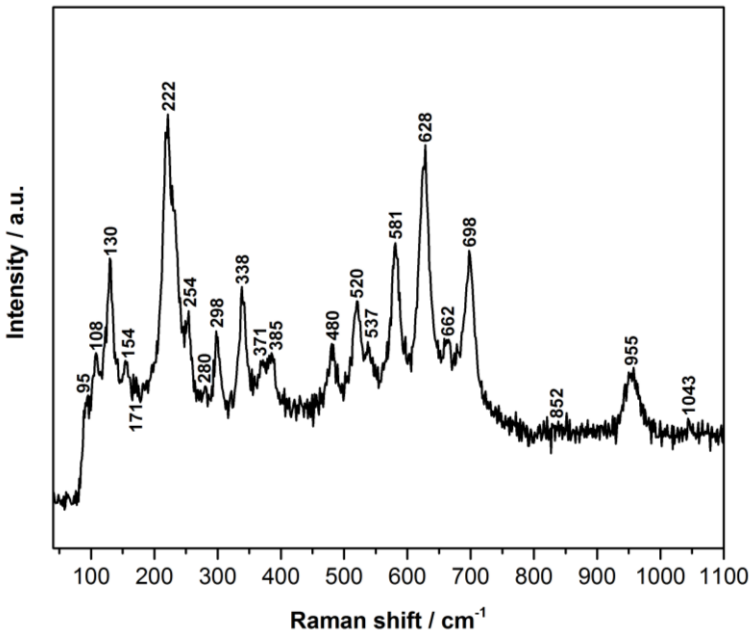

Figure 29: *Ex-situ* Raman spectrum of Mn_7SiO_{12} recorded 23 °C at 457 nm (exposure time = 10 min).

The results of high temperature Raman spectroscopy on Mn_7SiO_{12} are shown in **Figure 30**. The sample was heated in steps of roughly 100 °C from room temperature to 795 °C at 10 °C/min ($He:O_2$ = 79:21, total flow = 10 mL/min).

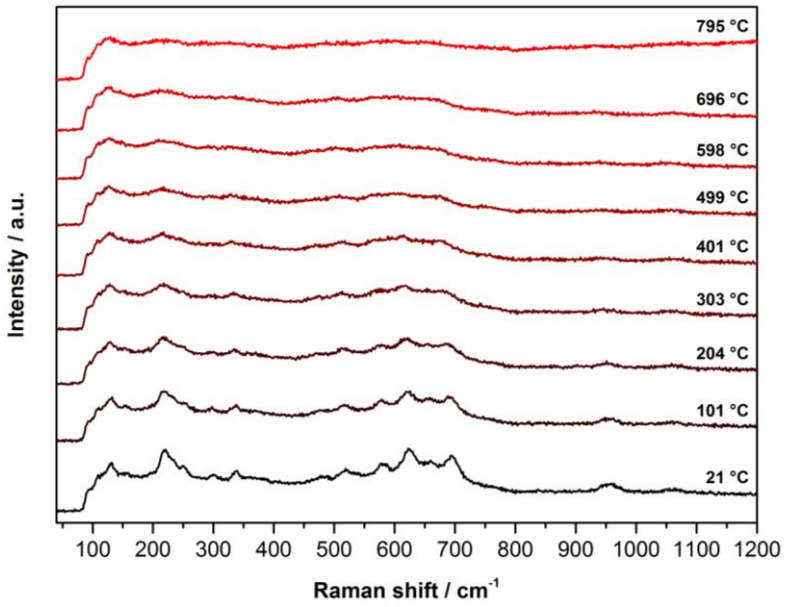

Figure 30: *In-situ* Raman spectra of Mn_7SiO_{12} recorded from 23 °C to 795 °C at 457 nm ($He:O_2$ = 79:21, total flow = 10 mL/min, exposure time = 10 min).

No changes in the band structure were observed. All bands broadened significantly with increasing temperature. The spectra recorded before and after heating were also identical.

Finally, the third reference sample, $MnWO_4$, was characterised spectroscopically. $MnWO_4$ has a wolframite structure at room temperature. Group theoretical analysis of the structure yields 36 lattice modes, out of which 18 are Raman active.[30g]

The room temperature spectrum of $MnWO_4$ recorded at 457 nm is given in **Figure 31**. Bands below 200 cm^{-1} can be assigned to lattice vibrations. Modes in the 200−400 cm^{-1} range originate from the bending vibrations of WO_6 octahedra while the 500−1000 cm^{-1} region features the stretching vibrations of the WO_6 octahedra.[30g] **Table 4** summarizes all phonon frequencies that were observed experimentally at ambient conditions together with the corresponding mode assignments.

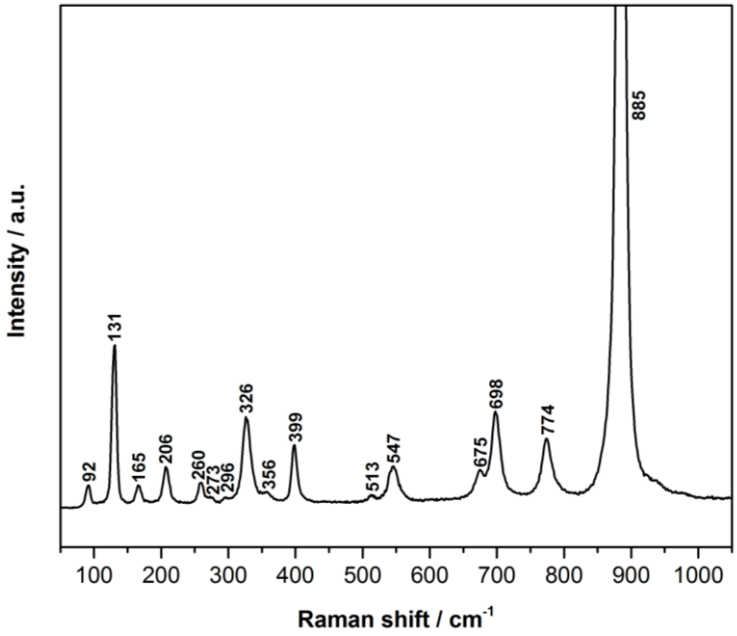

Figure 31: Raman spectrum of $MnWO_4$ recorded at 23 °C at 457 nm (exposure time = 3 min).

After recording the spectrum at room temperature, the sample was heated in steps of approximately 200 °C from 23 °C until 604 °C, followed by steps of approximately 100 °C from 604 °C to 795 °C at a heating rate of 10 °C/min under synthetic air (10 mL/min). Broadening together with a gradual frequency shift was observed for all peaks (refer to **Figure 32**).

Table 4: Observed modes for pure $MnWO_4$ at 23 °C (457 nm; L = lattice vibrations/translational modes, $\delta_{s/as}$ = symmetric/antisymmetric bending, $\nu_{s/as}$ = symmetric/antisymmetric stretching).

ω_{obs}	Mode assignment
92	L(WO_6)
131	L(WO_6)
165	L(WO_6)
206	δ_s(WOOW)
260	δ_s(WOOW)
273	unassigned
296	unassigned
326	δ_{as}(W–O)
356	unassigned
399	δ_s(W–O)
513	ν_s(WOOW)
547	ν_s(WOOW)
675	ν_s(WOOW)
698	ν_{as}(W–O)
774	ν_{as}(W–O)
885	ν_s(W–O)

The additional band at 931 cm^{-1} (604 °C) could not be identified. Similar results were reported in literature.[30g, 36] The positions of the most intense modes at 131 cm^{-1} and 885 cm^{-1} were plotted against the temperature (**Figure 33**). Both bands displayed a significant red shift. The Raman shift to higher wavenumbers from 604−701 °C might be associated with the occurrence of the abovementioned band at 931 cm^{-1}.

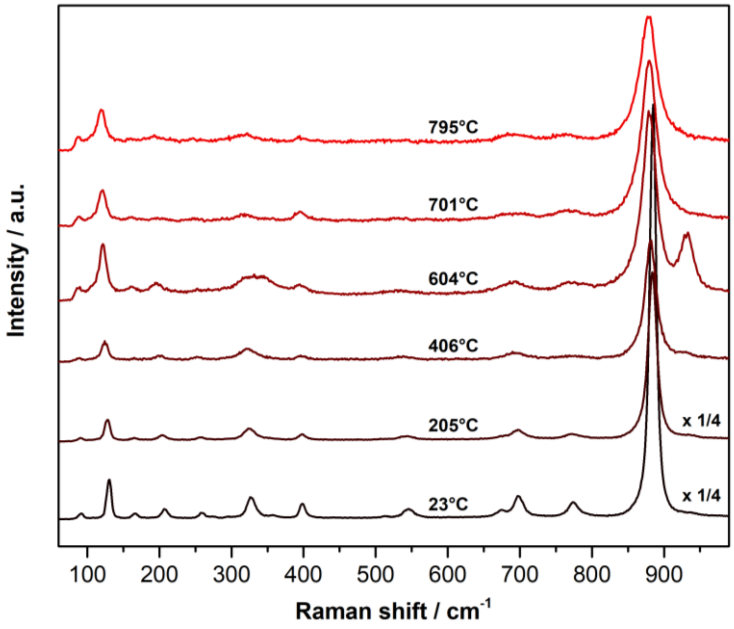

Figure 32: *In-situ* Raman spectra of $MnWO_4$ recorded from 23 °C to 795 °C at 457 nm ($He:O_2$ = 79:21, total flow = 10 mL/min, exposure time = 0.5−3 min).

In general, the observed changes in the Raman spectra correlate with the W–O bond strength, which in turn is influenced by the temperature induced lattice volume expansion. According to *Dai et al*., the observed monoclinic phase is stable up to 800 °C.[30g] The phase transition of $MnWO_4$ from solid to liquid starts at 900 °C and is completed at about 1100 °C. After cooling down to room temperature, the obtained Raman spectrum was identical to that of the starting sample.

The linear shift of Raman peaks to lower frequencies with increasing temperature for both Na_2WO_4 and $MnWO_4$, thus demonstrates that Raman frequencies correlate inversely with the temperature. Hereby indicated temperature-induced modes softening for the phonon frequency is mainly caused by the thermal expansion of the crystal.

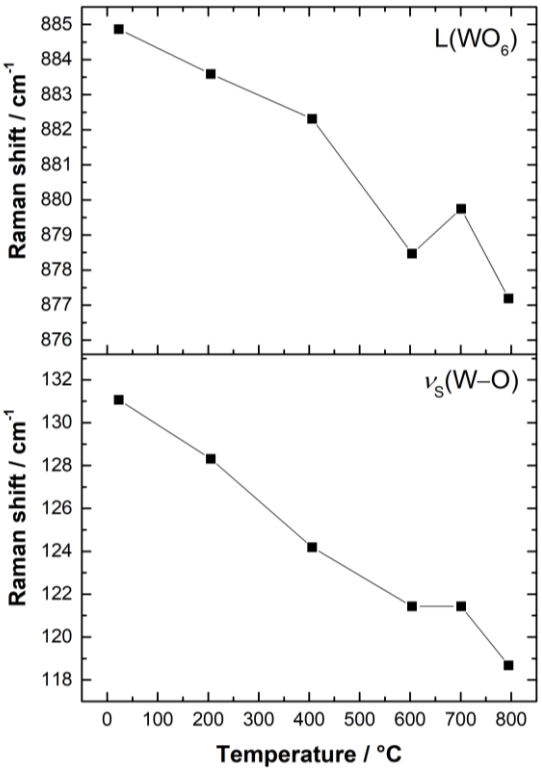

Figure 33: Temperature dependence of two selected Raman bands of $MnWO_4$.

Raman spectra of $MnWO_4$ were also recorded under different partial pressures of O_2 at 710 °C, 753 °C and 802 °C (**Figure 67−Figure 69**) with the aim of identifying structural changes. At all three temperatures, the spectra were recorded for 15 min for a given feed composition. No changes were observed.

After investigation of the reference samples, the catalyst system was studied *in-situ* under three different feeds from room temperature to its actual working

temperature of approximately 700−750 °C. A direct comparison of the peak positions and intensities of the reference spectra with those of the multiphase Mn-Na_2WO_4/SiO_2 catalyst enabled a successful allocation of bands in the corresponding spectra.

Figure 34 shows the temperature-dependent spectra of the catalyst under inert gas conditions (Ar, 10 mL/min). In order to equilibrate the catalyst, it was first heated to 740 °C at 50 °C/min. The temperature was maintained for one hour. After equilibration, the catalyst was cooled down to 91 °C (50 °C/min), where the first measurement was performed. Two intense bands at 885 cm^{-1} and 931 cm^{-1} appeared, indicating the presence of $MnWO_4$ and Na_2WO_4 respectively. With the help of the recorded reference spectra, several other bands for both $MnWO_4$ and Na_2WO_4 were identified (refer to **Figure 70**). A disappearance of all bands of Mn_7SiO_{12} was also evident. The unidentified bands at 463 cm^{-1} and 589 cm^{-1} are tentatively attributed to Mn-containing species, based on data reported in literature for MnOOH[37], MnO_2[38] and Mn_2O_3[38]. Patcas *et al*. also found several bands from 464−675 cm^{-1} for MnO_x/SiO_2 catalysts with different Mn/Si ratios.[39] A structural similarity with Mn_7SiO_{12}, however, must not be excluded, as it possesses modes in a similar range (480 cm^{-1} and 581 cm^{-1}, refer to **Figure 29**). Two signals of the support were visible at 227 cm^{-1} and 412 cm^{-1}.

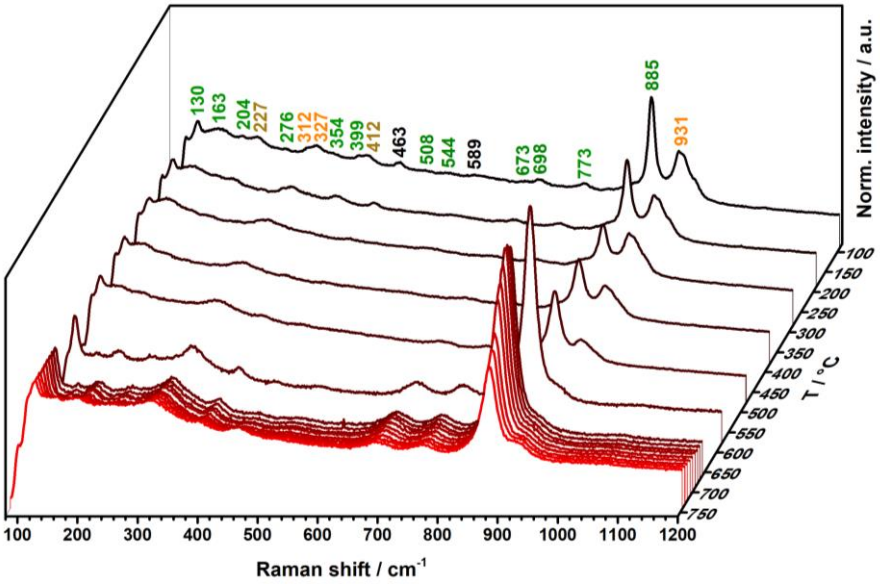

Figure 34: Raman spectra of the Mn-Na_2WO_4/SiO_2 catalyst in Ar (10 mL/min) recorded from 91 °C to 740 °C at 457 nm after equilibration (exposure time = 7.5 min). Modes for $MnWO_4$, Na_2WO_4 and SiO_2 are marked in green, orange and brown respectively. Unassigned bands are marked in black. The spectra were normalized to the band at 130 cm^{-1}.

Following the first measurement, the sample temperature was increased in steps of approximately 100 °C (rate: 25 °C/min) until 657 °C and in steps of 10 °C (rate: 10 °C/min) from 657−740 °C. Upon increasing the temperature of the sample, the peaks for the supported $MnWO_4$ and Na_2WO_4 species broadened gradually. By plotting the intensity of the 885 cm^{-1} band against the temperature, the concentration of formed $MnWO_4$ was shown to decrease until 283 °C, from whereon a slow increase takes place (refer to **Figure 35**). Between 477 °C and 577 °C, a drastic rise occurs, pointing to a re-formation of $MnWO_4$. The vibrational mode at 931 cm^{-1}, representative for Na_2WO_4, gradually loses intensity at higher temperatures. A complete disappearance or conversion of Na_2WO_4 into another phase at high temperatures was not observed spectroscopically. The above-mentioned peaks of the support at 227 cm^{-1} and 412 cm^{-1}, however, did disappear at higher temperatures due to its phase transition from α- to β-cristobalite at 267 °C[30a, 30c, 30d]. The relatively broad band that is observed in all spectra from approximately 100−400 cm^{-1} originates from the support.

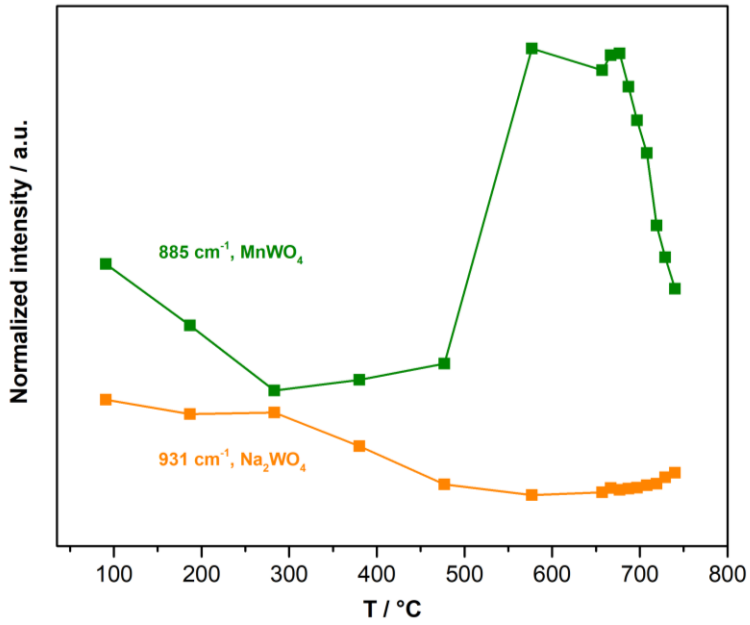

Figure 35: Temperature-dependency of selected peak intensities for $MnWO_4$ (885 cm^{-1}) and Na_2WO_4 (931 cm^{-1}) in Ar (10 mL/min) (normalization to band at 130 cm^{-1}).

The modes for $MnWO_4$ at 130 cm^{-1} and 885 cm^{-1} remained throughout the experiment, suggesting an irreversible conversion of Mn_7SiO_{12} into $MnWO_4$ under given conditions. The combination of an inert atmosphere and high temperature thus had a reducing effect on the Mn-Na_2WO_4/SiO_2 catalyst. The formation of $MnWO_4$ can only occur by reaction of Mn_7SiO_{12} with Na_2WO_4. While Mn^{3+} is

reduced to Mn^{2+}, the corresponding oxidation step is not clear. It is possible that W^{5+}/W^{6+} is involved in a redox cycle. The possibility of defect structure formation must also be considered. Na is postulated to either go into the support or to form a new phase with the silica support.

The phase transition is confirmed by comparing the spectra recorded before and after heating. As seen in **Figure 36**, the vibrational modes of Mn_7SiO_{12} in the 450−750 cm^{-1} region disappeared partially after heating, giving rise to modes belonging to $MnWO_4$ and the abovementioned, unidentified mode at 465 cm^{-1}. The absence of several vibrational modes of Mn_7SiO_{12} suggests that the mode may be related to a newly formed species. The presence of the 937 cm^{-1} band of Na_2WO_4 confirms that only a portion of the phase was involved in the reaction.

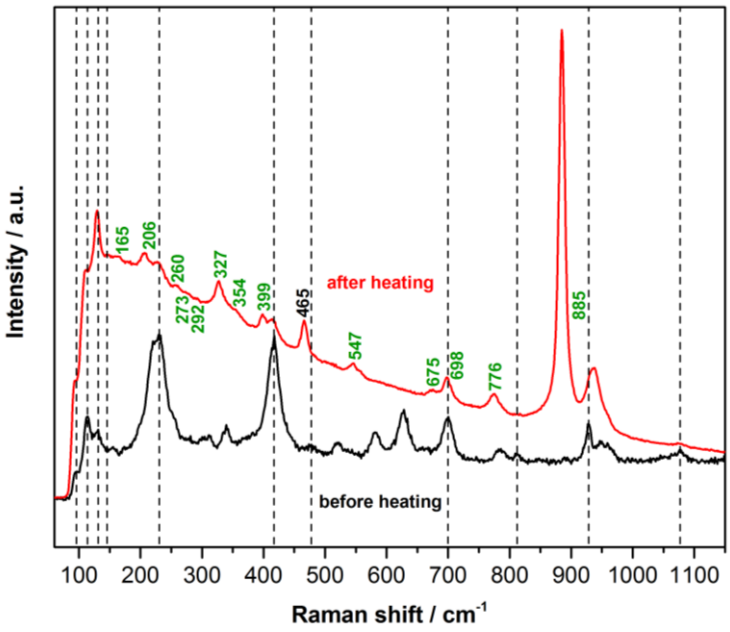

Figure 36: Raman spectra of the equilibrated Mn-Na_2WO_4/SiO_2 catalyst in Ar (10 mL/min) recorded before (23 °C, black) and after heating (30 °C, red) at 457 nm ($T_{heating,\ max}$ = 740 °C, exposure time = 7.5 min). Identical peaks are marked with dotted lines. Modes representing $MnWO_4$ are labelled in green.

The experiment was consequently repeated without prior equilibration of the catalyst at 740 °C. As shown in **Figure 37**, the characteristic modes for $MnWO_4$ first appeared in the spectrum recorded at 477 °C at 119 cm^{-1} and 882 cm^{-1} respectively. In the spectra collected at 577 °C and above, both modes featured with much increased intensities. The remaining bands for $MnWO_4$ as well as those for Na_2WO_4 can be assigned as has been done in **Figure 34**. Temperature induced band broadening was observed, especially for the bands originating from Na_2WO_4. A significant broadening of the mode at 922 cm^{-1} was visible when increasing the temperature above 477 °C. The sample position was changed at 380 °C and

477 °C to obtain spectra of higher quality. No new bands were observed. Similar to the previous experiment, an irreversible formation of $MnWO_4$ occurred under given experimental conditions.

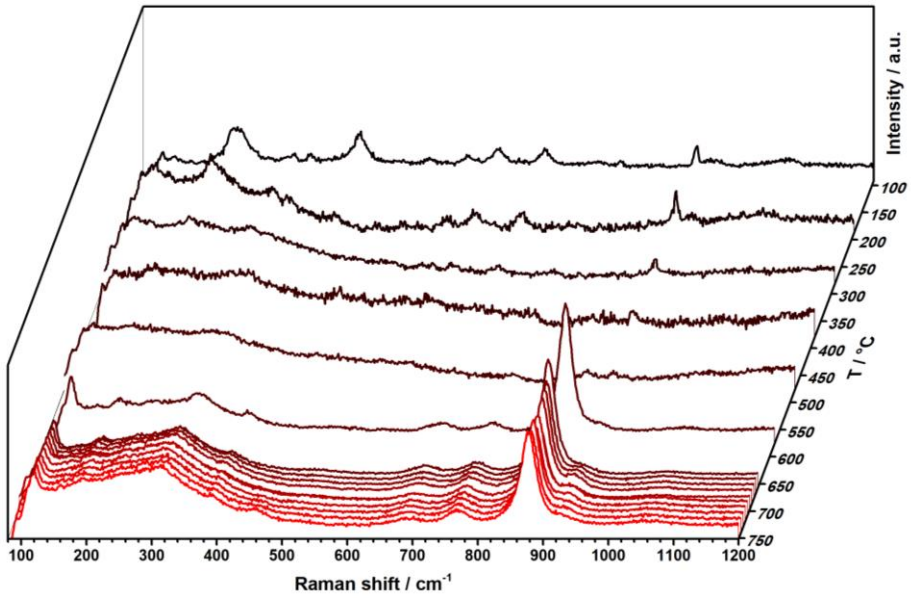

Figure 37: Baseline-corrected Raman spectra of the unequilibrated Mn-Na_2WO_4/SiO_2 catalyst in Ar (10 mL/min) recorded from 91 °C to 751 °C at 457 nm without catalyst equilibration (exposure time = 7.5 min). The spectra were normalized to the band at 120 cm^{-1}.

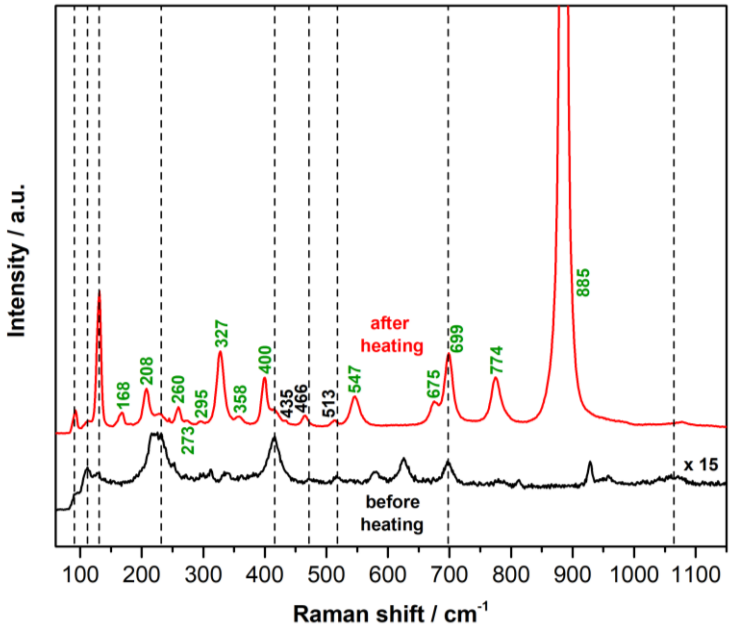

Figure 38: Raman spectra of the unequilibrated Mn-Na_2WO_4/SiO_2 catalyst in Ar (10 mL/min) recorded before (23 °C, black) and after heating (30 °C, red) at 457 nm ($T_{heating, max}$ = 751 °C, exposure time = 7.5 min). Identical peaks are marked with dotted lines. Modes representing $MnWO_4$ are labelled in green.

The room temperature spectrum recorded after heating the sample clearly contains bands that can be attributed to $MnWO_4$. (refer to **Figure 38**) The three modes occurring at 435, 466 and 513 cm^{-1} respectively could not be allocated

based on the reference spectra for $MnWO_4$ and Na_2WO_4 or on the spectrum recorded before heating. A MnO_x phase on SiO_2 is again suggested. With Mn_7SiO_{12} displaying similar bands in an identical region of the spectrum, however, the formation of a phase with structurally similar motifs must be considered. No sharp peak indicating Na_2WO_4 was present, suggesting a consumption of the phase in the formation of $MnWO_4$.

The results of *in-situ* Raman spectroscopy for the Mn-Na_2WO_4/SiO_2 catalyst under oxidizing conditions are given in **Figure 39**. The catalyst was heating from room temperature to 577 °C in steps of approximately 100 °C and from 657−751 °C in steps of 10 °C (heating rate: 10 °C/min). In contrast to the experiments under inert conditions, no significant phase transitions, apart from the α- to β-cristobalite transition of the support, were observed. No modes indicating the formation of $MnWO_4$ were detected. The bands for the supported Mn_7SiO_{12} and Na_2WO_4 species broadened as expected with increasing temperature. The sharp band at 923 cm^{-1}, attributed to Na_2WO_4, broadened significantly when increasing the temperature from 477 °C to 577 °C, as seen in analogous experiments under inert conditions. The sample position was changed at 751 °C to improve the quality of the spectrum. No changes in the composition of the spectrum were observed.

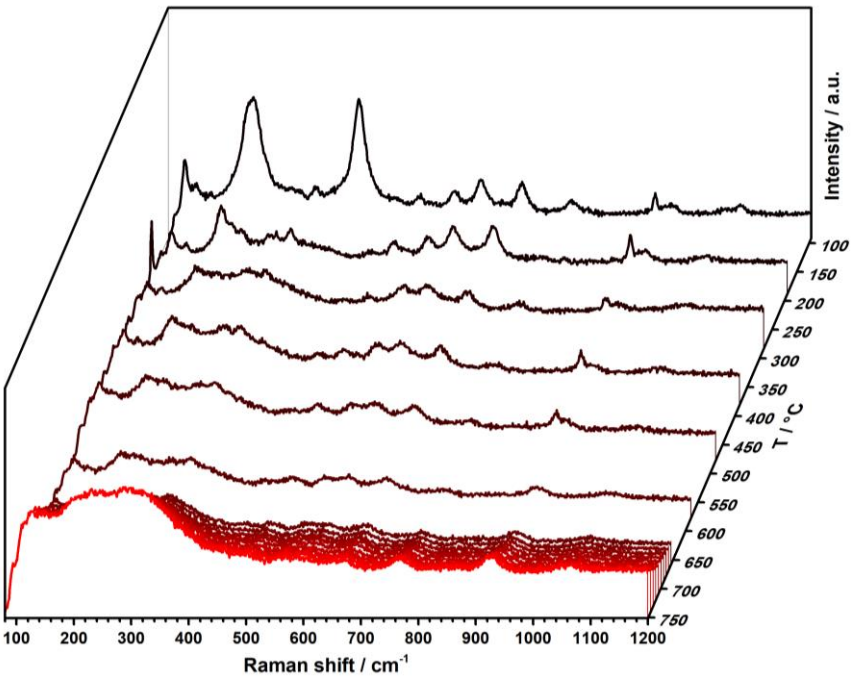

Figure 39: Raman spectra of the unequilibrated Mn-Na_2WO_4/SiO_2 catalyst in O_2:Ar = 1:8 (total flow = 10 mL/min) recorded from 91 °C to 751 °C at 457 nm (exposure time = 7.5 min).

The aforementioned results are also supported by the spectra recorded at room temperature after heating (refer to **Figure 40**). No new modes were observed after the experiment. However, the intensity of the bands for Na_2WO_4, featuring at 311, 813 and 930 cm^{-1}, decreased. This could be the result of an inhomogeneous distribution of Na_2WO_4 on the support, as the sample position was changed during the experiment. It is more likely, however, that a melting process of Na_2WO_4 has consequently led to less pronounced signal intensities, as already seen for the reference sample (refer to **Figure 28**) In general, the formation of $MnWO_4$, which corresponds to a partial or complete reduction of Mn_7SiO_{12}, may have suppressed by the presence of gas-phase oxygen.

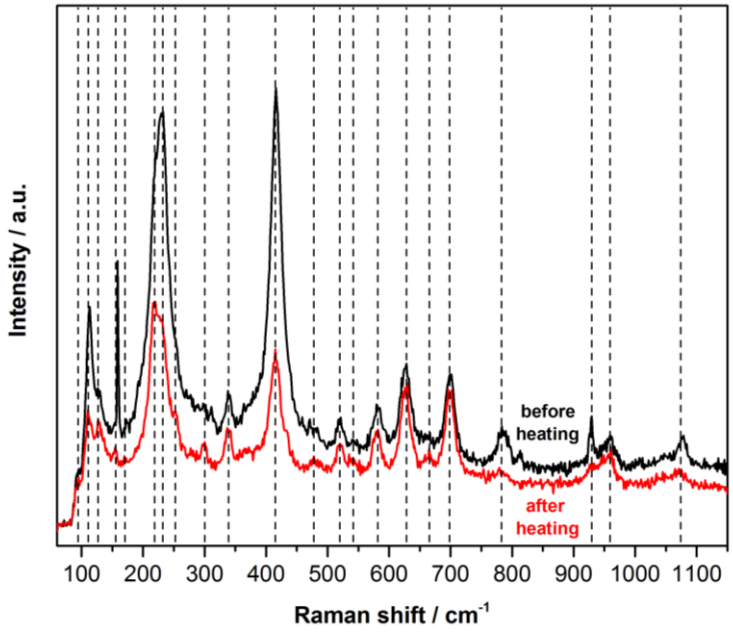

Figure 40: Raman spectra of the unequilibrated Mn-Na_2WO_4/SiO_2 catalyst in O_2:Ar = 1:8 (total flow = 10 mL/min) recorded before (23 °C, black) and after heating (30 °C, red) at 457 nm ($T_{heating, max}$ = 751 °C, exposure time = 7.5 min). Identical peaks are marked with dotted lines.

In order to determine whether a transition of the Na_2WO_4 phase from solid to liquid takes place at higher temperatures, thereby causing an intensity loss, the catalyst was studied under identical conditions between 501 °C and 752 °C (refer to **Figure 41**). For this, the sample was directly heated to 500 °C at 25 °C/min. Spectra were recorded every 10 °C while maintaining the same heating rate. The experiment revealed a gradual decrease in intensity of the 921 cm^{-1} band, with a noticeable drop occurring between 581 °C and 591 °C. Considering previous results (refer to **Figure 34**, **Figure 35** and **Figure 37**), it is possible that the onset of a phase transition of Na_2WO_4 occurs in this range.

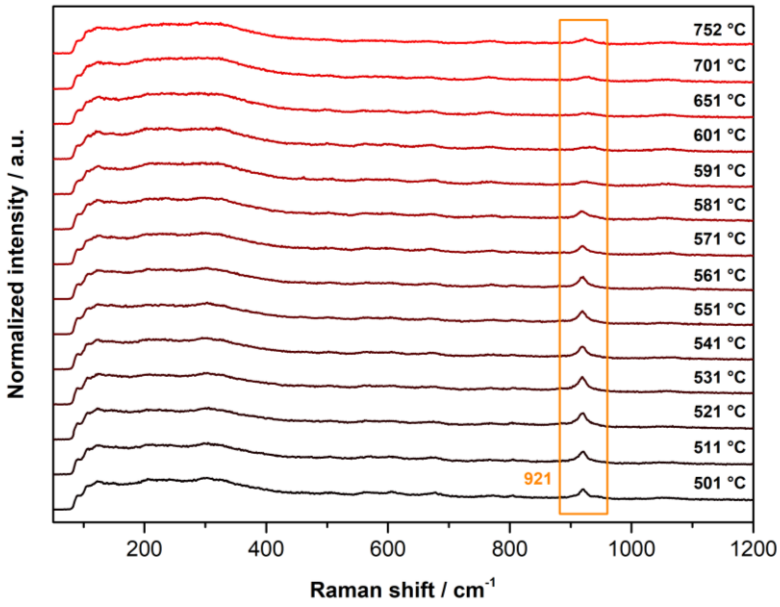

Figure 41: Raman spectra of the unequilibrated Mn-Na_2WO_4/SiO_2 catalyst in O_2:N_2 = 1:8 (total flow = 10 mL/min) recorded from 501 °C to 752 °C at 457 nm (exposure time = 10 min). The mode representing Na_2WO_4 is marked in orange.

The room temperature spectra of this experiment (refer to **Figure 42**) are similar to those collected in the previous experiment (refer to **Figure 40**). An intensity loss of the bands at 312, 809 and 927 cm^{-1} was observed, indicating structural changes to the Na_2WO_4 phase.

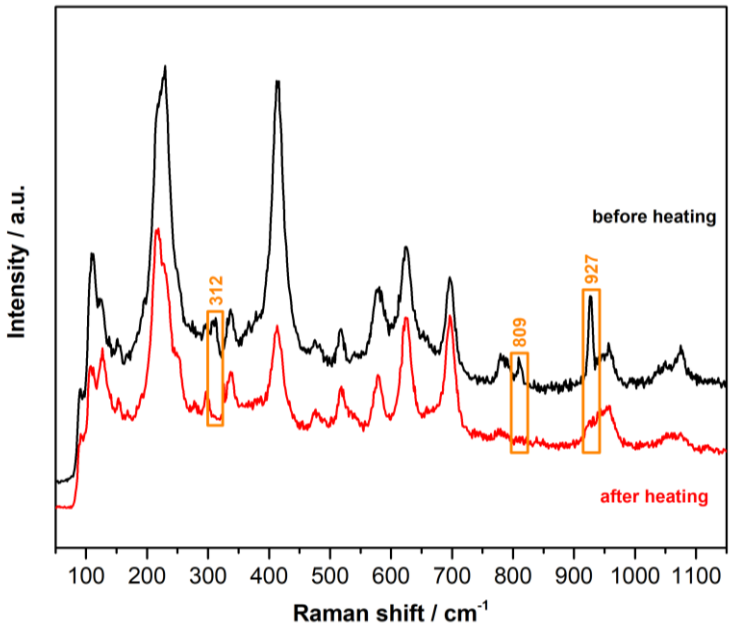

Figure 42: Raman spectra of the unequilibrated Mn-Na_2WO_4/SiO_2 catalyst in O_2:N_2 = 1:8 (total flow = 10 mL/min) recorded before (23 °C, black) and after heating (31 °C, red) at 457 nm ($T_{heating, max}$ = 752 °C, exposure time = 10 min). Modes representing Na_2WO_4 are marked in orange.

If a liquefaction of Na_2WO_4 is assumed based on given results, a correlation between this transition and an increased rate for the formation of $MnWO_4$ seems plausible (refer to **Figure 34**, **Figure 35** and **Figure 37**).

The Mn-Na_2WO_4/SiO_2 catalyst was also studied under reducing conditions (CH_4:Ar = 4:5, total flow = 10 mL/min). The sample was heated from 23−590 °C in steps of approximately 100 °C (rate: 25 °C/min) and from 634−718 °C in steps of 10 °C at 10 °C/min. The spectra recorded below 590 °C mainly featured the modes of Mn_7SiO_{12} and Na_2WO_4 (refer to **Figure 43**). For the latter, the 932 cm^{-1} mode increased in intensity at 590 °C. Concurrently, 10 new modes, indicating the presence of $MnWO_4$, were formed below 1000 cm^{-1}, the most notable appearing at 881 cm^{-1}. These bands increased dramatically in intensity upon heating to 634 °C. Raising the temperature above 634 °C, however, consequently resulted in all bands gradually losing intensity. This might be the result of strong coking, which was indicated by the characteristic D- and G-bands of carbon appearing in most spectra. The spent catalyst was also significantly darker.

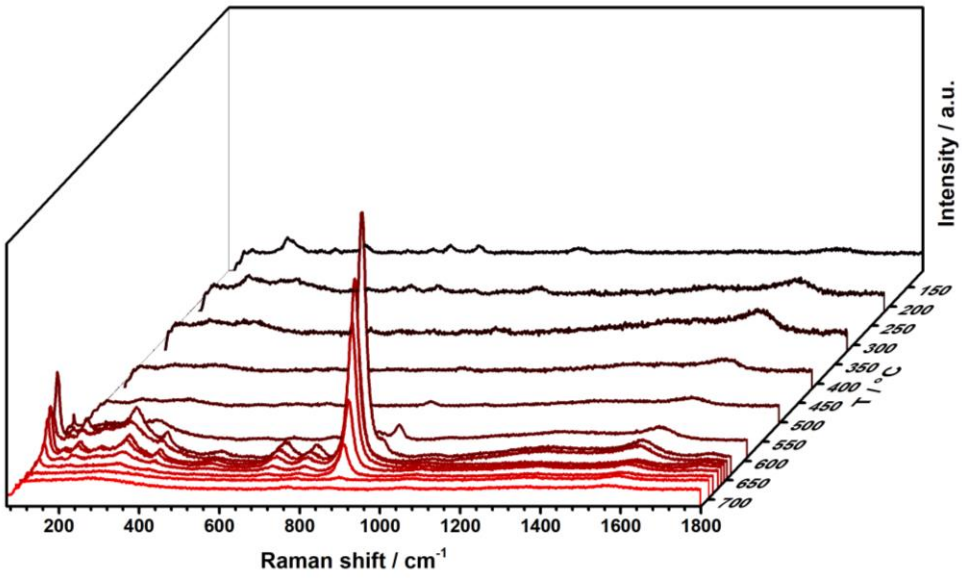

Figure 43: Baseline corrected Raman spectra of the unequilibrated Mn-Na_2WO_4/SiO_2 catalyst in CH_4:Ar = 4:5 (total flow = 10 mL/min) recorded from 107 °C to 718 °C at 457 nm (exposure time = 7.5 min).

Plotting the spectra recorded at 695 °C and 718 °C separately, as seen in **Figure 44**, helped to identify modes for the catalyst at maximum temperature. Bands denoting the presence of $MnWO_4$ and β-cristobalite were observed. The D- and G-bands of carbon also appeared at 1363 cm^{-1} and 1571 cm^{-1} respectively. An un-assigned band was registered at 835 cm^{-1}.

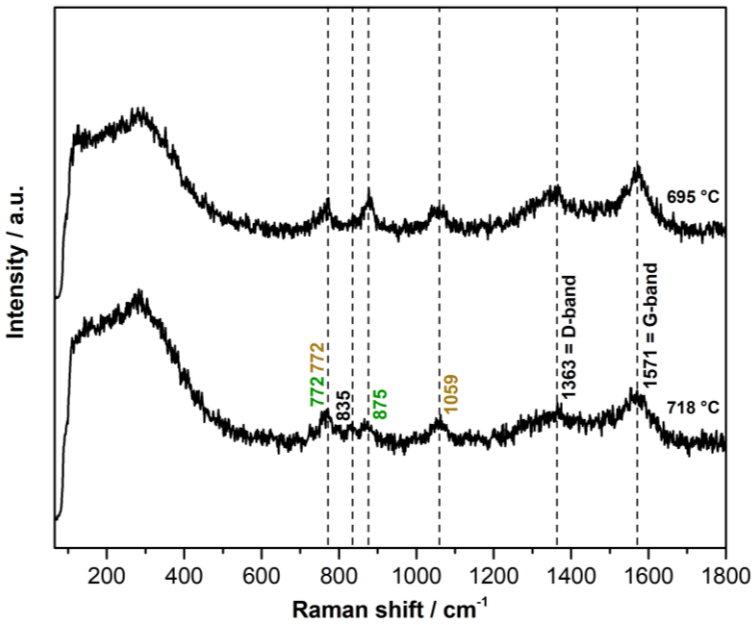

Figure 44: Baseline corrected Raman spectra of the unequilibrated Mn-Na_2WO_4/SiO_2 catalyst in CH_4:Ar = 4:5 (total flow = 10 mL/min) recorded at 695 °C and 718 °C at 457 nm (exposure time = 7.5 min). Identical peaks are marked with dotted lines. Modes for $MnWO_4$ and SiO_2 are marked in green and brown respectively. Unassigned bands as well as bands originating from coke are marked in black.

The spectrum recorded after the experiment (refer to **Figure 45**) also showed a significant coking of the catalyst**.** In comparison to the spectrum recorded at ambient conditions before the experiment, no modes representing any of the supported phases were detectable. The discoloration of the catalyst further underlined the significant amount of coking during the reaction.

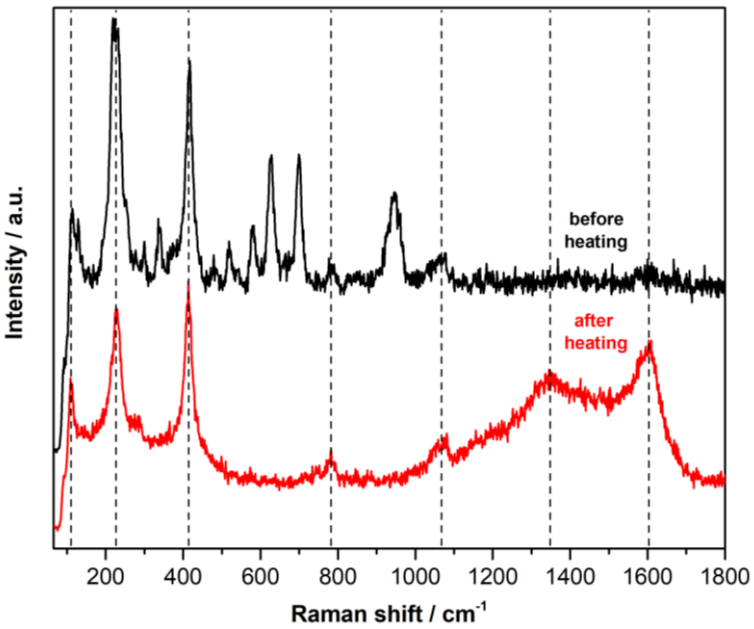

Figure 45: Baseline corrected Raman spectra of the unequilibrated Mn-Na_2WO_4/SiO_2 catalyst in CH_4:Ar = 4:5 (total flow = 10 mL/min) recorded before (23 °C, black) and after heating (30 °C, red) at 457 nm ($T_{heating,\ max}$ = 718 °C, exposure time = 7.5 min). Identical peaks are marked with dotted lines.

The experiments conducted under inert, oxidizing and reducing feed conditions revealed that $MnWO_4$ was formed by a reaction of Mn_7SiO_{12} with Na_2WO_4, as indicated by the complete disappearance of the Mn_7SiO_{12} bands and the loss in signal intensity of the Na_2WO_4 modes after heating. This phase conversion was suppressed in the presence of oxygen, which underlines the influence of a reducing feed (CH_4/Ar or Ar). $MnWO_4$ was detected in high concentrations at 577 °C and 634 °C for Ar and CH_4/Ar feeds respectively. Structural changes to the Na_2WO_4 phase, resulting in a significant intensity loss, were observed from 581 °C onwards in an O_2/Ar atmosphere. It is possible that this a consequence of melting. A correlation between the liquefaction of Na_2WO_4 and the formation of $MnWO_4$ is postulated, with the melt acting as transfer medium for solid state reactions.

After studying the catalyst at higher temperatures under inert, oxidizing and reducing feed conditions, the system was investigated spectroscopically from 635−728 °C under an OCM reaction feed of CH_4:O_2:Ar = 4:1:4 (total flow rate = 10 mL/min, sample heated with 25 °C/min to 635 °C and with 10 °C/min from 635−728 °C). **Figure 46** shows the Raman spectra collected between 671 °C and 728 °C. The spectral region of 100−400 cm^{-1} was dominated by a broad band of the β-cristobalite support.[30c] The prominent peak at 120 cm^{-1} originates from Mn_7SiO_{12} and/or $MnWO_4$, depending on whether the corresponding phase transition has taken place. The spectra recorded until 684 °C predominantly featured bands of Mn_7SiO_{12} and the β-cristobalite support (refer to **Figure 46**, **Figure 72**). The relatively broad shape of the band at 931 cm^{-1}, characteristic of supported Na_2WO_4, suggests liquefaction of the phase. Upon increasing the temperature above 684 °C, the Mn_7SiO_{12} modes decreased in intensity and disappeared. The formation of a new band at approximately 878 cm^{-1} from 696 °C onwards revealed the presence of $MnWO_4$ in higher concentrations. The concurrent disappearance of the Mn_7SiO_{12} modes indicates that the phase is involved in the reaction to form $MnWO_4$.

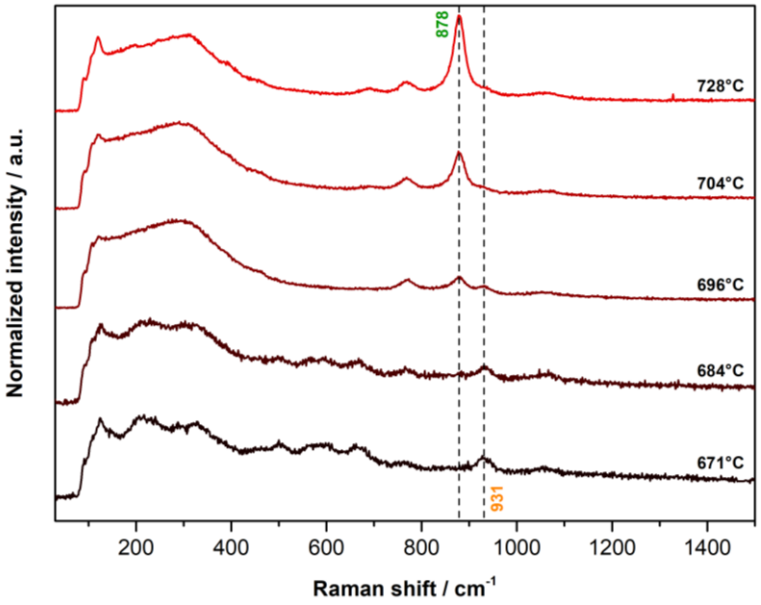

Figure 46: Baseline-corrected Raman spectra of the unequilibrated Mn-Na_2WO_4/SiO_2 catalyst recorded from 671 °C to 728 °C at 457 nm under reaction conditions (CH_4:O_2:Ar = 4:1:4, total flow = 10 mL/min, exposure time = 10 min). Modes representing $MnWO_4$ and Na_2WO_4 are labelled in green and orange respectively. The spectra were normalized to the band at 124 cm^{-1}.

The room temperature spectra recorded after the experiment confirmed that $MnWO_4$ has been formed (refer to **Figure 47**). Modes indicating Mn_7SiO_{12} are also visible. This may either be attributed to an incomplete conversion of Mn_7SiO_{12} into $MnWO_4$ under reaction conditions or to a reversibility of this reaction.

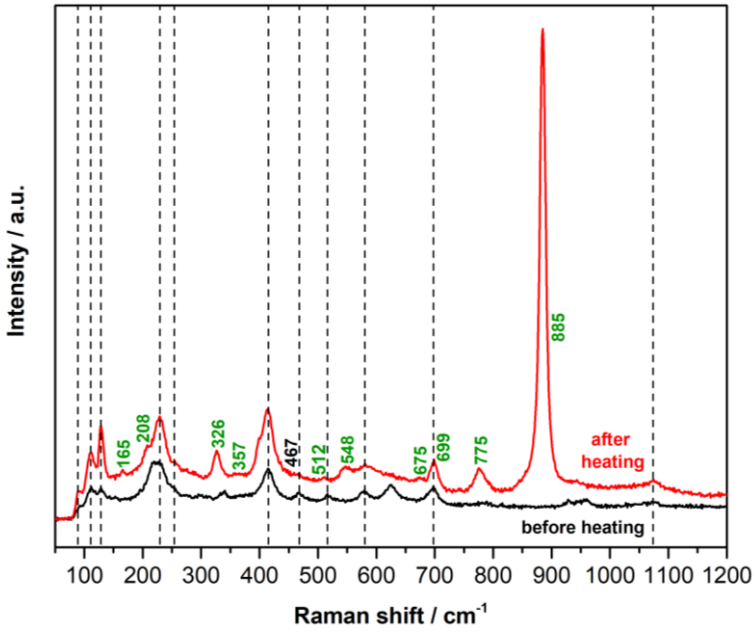

Figure 47: Raman spectra of the Mn-Na_2WO_4/SiO_2 catalyst under reaction conditions (CH_4:O_2:Ar = 4:1:4, total flow = 10 mL/min) recorded before (20 °C, black) and after reaction (44 °C, red) at 457 nm (exposure time = 10 min). Identical peaks are marked with dotted lines. Modes representing $MnWO_4$ are labelled in green.

XRD analysis of the spent catalyst also confirmed the presence of $MnWO_4$ (**Figure 48**). The decline of the reflection intensities of Na_2WO_4 and Mn_7SiO_{12}, most markedly shown by the reflections at 2θ = 32° and 2θ = 33° respectively, indicates a reaction of these two phases to yield $MnWO_4$. The spent catalyst also contains a higher fraction of SiO_2 in form of quartz, analogous to the sample removed from the reactor after testing (refer to **Figure 22**). Phase analysis revealed the catalyst to contain 76.38 wt% α-cristobalite, 19.37 wt% quartz, 0.73 wt% Na_2WO_4 and 3.52 wt% $MnWO_4$. The amount of Na_2WO_4 has thus decreased significantly compared to the fresh catalyst. Furthermore, no braunite was detected, suggesting a complete conversion of the phase into $MnWO_4$ or an X-ray amorphous phase. A dispersed MnO_x/SiO_2 species seems likely due to the occurrence of bands in the Raman spectrum after heating from approximately 450−700 cm^{-1}.[39]

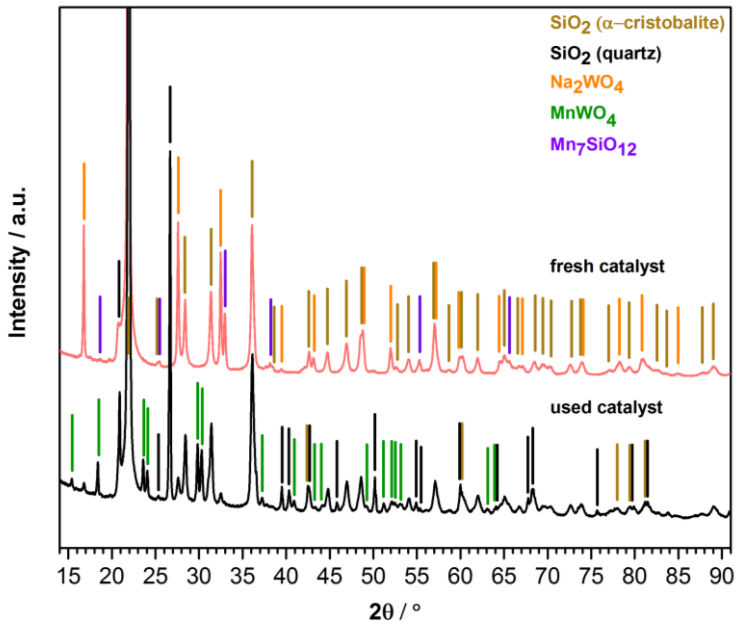

Figure 48: XRD of Mn-Na_2WO_4/SiO_2 before (red) and after reaction (black). Only new reflexes are labelled for the used catalyst.

In order to study the correlation of possible phase transitions with the catalyst performance, the activity of the catalyst was monitored with the help of online gas chromatography. As expected, the main reaction products included ethane, ethene, carbon oxides and water. Hydrogen, coke and small amounts of propane were also formed. $X(CH_4)$ and $X(O_2)$ of the catalyst are given in **Figure 49**. From 635 °C onwards, the oxygen was almost completely consumed.

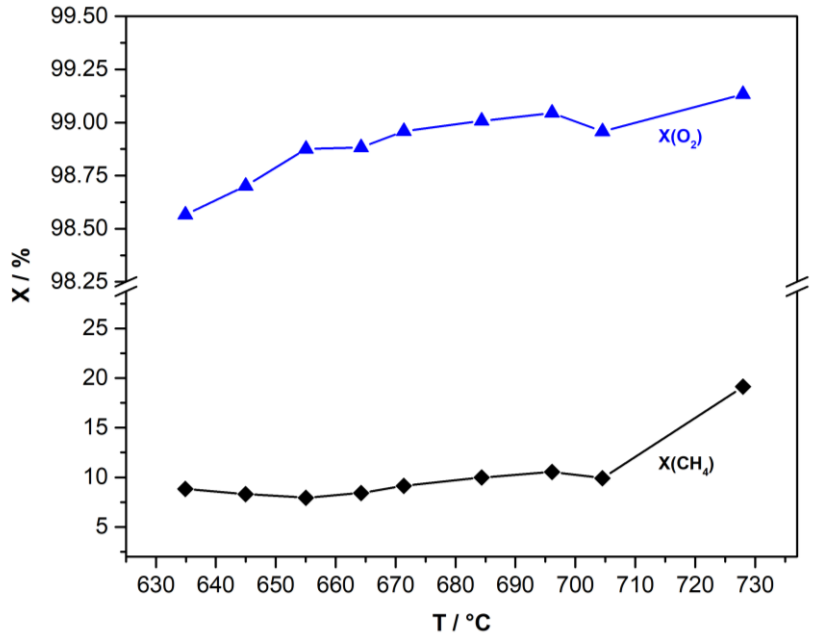

Figure 49: $X(CH_4)$ and $X(O_2)$ for 30.0 mg of Mn-Na_2WO_4/SiO_2 catalyst in a feed of CH_4:O_2:Ar = 4:1:4 (total flow = 10 mL/min) (W/F = 0.0030 g*min*mL^{-1}). The reaction was performed in a Harrick reaction cell.

To evaluate the activity of the catalyst, the formation of ethane and ethene was plotted against the temperature, as seen in **Figure 50**.

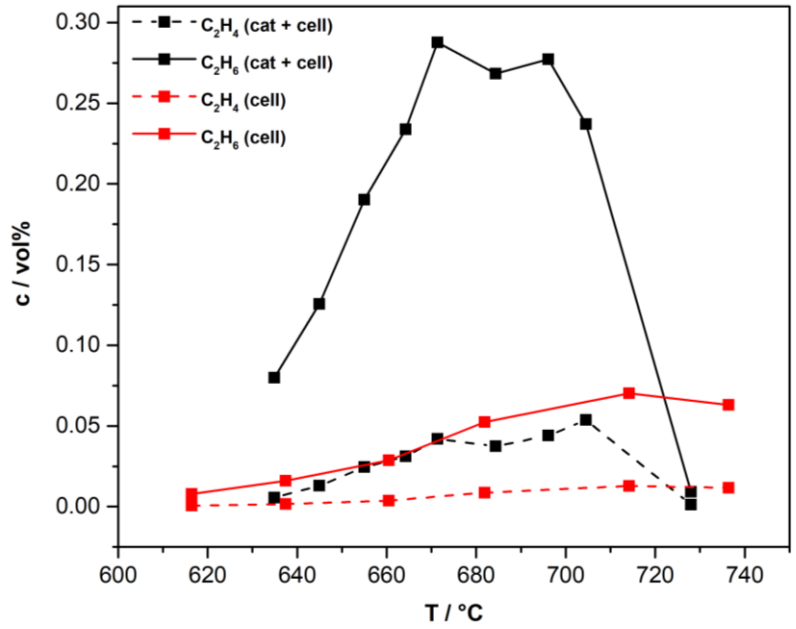

Figure 50: Formation of ethane (C_2H_6) and ethene (C_2H_4) as a function of temperature for the Mn-Na_2WO_4/SiO_2 catalyst under reaction conditions (black) *versus* the reaction cell (red) (T =635−728 °C; CH_4:O_2:Ar = 4:1:4, total flow = 10 mL/min; W/F = 0.0030 g*min*mL^{-1}).

While the data for the catalyst (+ cell) is marked in black, the blank activity measurement of the cell is given in red. It is evident that the catalytic activity can be mainly attributed to the catalyst (also refer to **Figure 73** and **Figure 74** for activity comparison). As seen above, the concentration of both ethane and ethene

increased linearly with temperature until 671 °C, where a plateau was reached. Using this linear regime, activation energies for the formation of ethane and ethene were calculated as 248 kJ/mol and 382 kJ/mol respectively (refer to **Figure 75**). This is in agreement with literature.[40] A linear extrapolation of the regression lines gave corresponding onset temperatures of 616 °C and 617 °C for the reaction. A sharp decline in activity occurred from 696 °C onwards, which coincided with the formation of the $MnWO_4$ and the disappearance of the Mn_7SiO_{12} modes, as observed via Raman spectroscopy (**Figure 51**). Intensities of the modes for $MnWO_4$ and Na_2WO_4, observed at approximately 878 cm^{-1} and 927 cm^{-1} (refer to **Figure 46**), were also plotted against the catalytic data. While the concentration of Na_2WO_4 decreased gradually, a prominent increase in the concentration of $MnWO_4$ was evident.

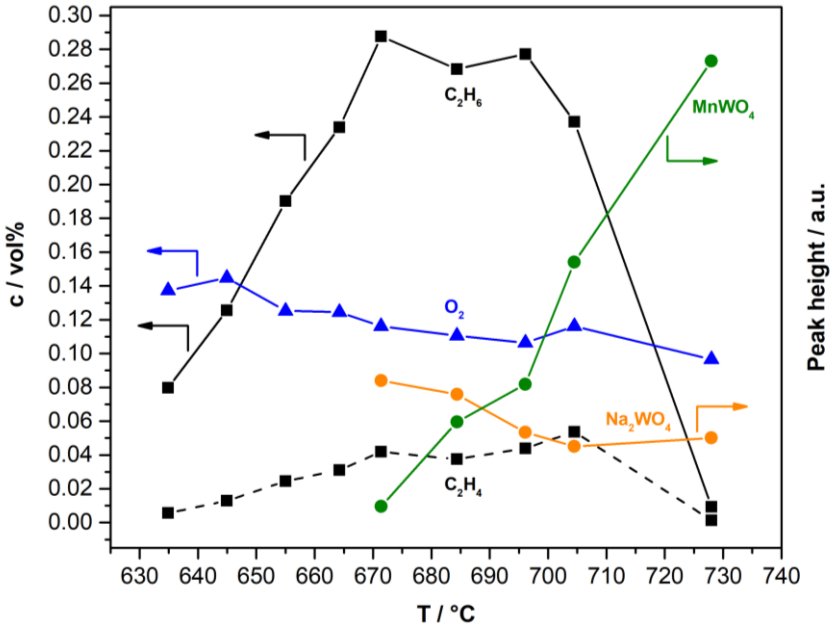

Figure 51: Correlation between the catalyst activity, represented indirectly by the concentrations of ethane and ethene, and the formation of $MnWO_4$ and Na_2WO_4 phases, as determined via Raman spectroscopy (peak heights derived after normalization to peak at 124 cm^{-1}) (T =635−728 °C; CH_4:O_2:Ar = 4:1:4, total flow = 10 mL/min; W/F = 0.0030 g*min*mL^{-1}).

A similar plot depicting the catalyst selectivity and activity in correlation with the concentrations of $MnWO_4$ and Na_2WO_4 is given in **Figure 52**. The formation of $MnWO_4$ goes along with an increase in CH_4 and O_2 conversion. This rising CH_4 conversion is, in turn, responsible for a drop in C_2 selectivity.

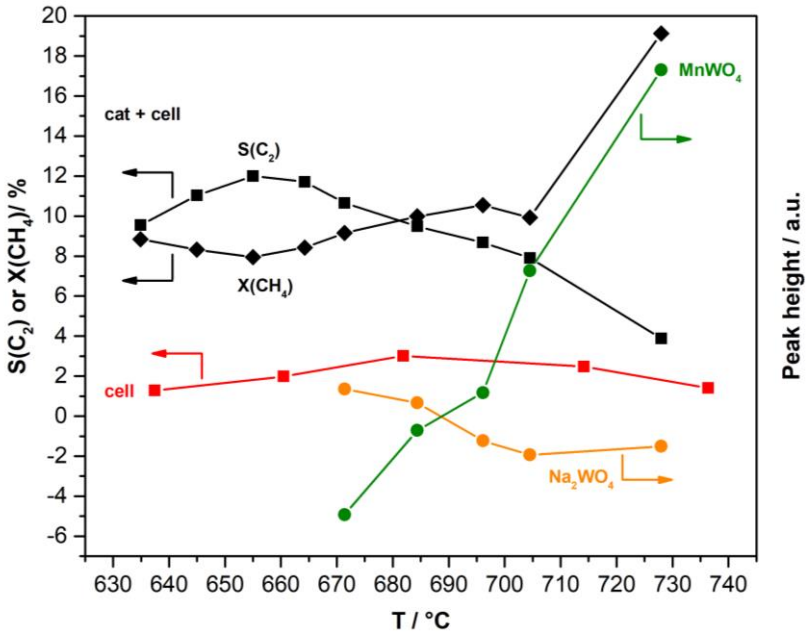

Figure 52: Correlation between the catalyst selectivity, methane conversion and the formation of $MnWO_4$ and Na_2WO_4 phases, as determined via Raman spectroscopy (peak heights derived after normalization to peak at 124 cm^{-1}) (T =635−728 °C; CH_4:O_2:Ar = 4:1:4, total flow = 10 mL/min; W/F = 0.0030 g*min*mL^{-1}).

It must be acknowledged that the *operando* experiment only helps to establish a trend of reactivity and does not yield accurate catalytic data. Firstly, differences in reactivity arise from the setup. The Harrick reaction cell that was used cannot reproduce the performance of a full-scale tubular reactor. The herein observed fluid dynamics are bound to differ strongly from those experienced in a reactor. Secondly, by using the catalyst in an undiluted and, more importantly, mortared state, the ratio of catalyst surface to void volume of the bed (S/V) was changed. This can affect the relative contributions of heterogeneous reactions at the catalyst surface and homogeneous reactions in the gas-phase (void volume). Koirala *et al*. showed that an increase in the CH_4-conversion correlates with the catalyst amount (W/F or S/V), indicating a strong dependency on the heterogeneous reaction network.[41] Local hot spot formation may also be favoured.[41]

In order to verify this reactivity trend, a time-on-stream experiment was performed at 685 °C using a similar *operando* approach. The catalyst was heated to the desired temperature at 50 °C/min. Once the temperature was reached, continuous Raman spectroscopy (exposure time = 1 min per spectrum) was used to monitor the structural dynamics of the catalyst in combination with online gas chroma-tography. The temperature was maintained for approximately 1 h. A fluctuating conversion of methane was observed during the reaction (refer to **Figure 53**). This

unusual behaviour could indicate that the catalyst has not reached steady-state conditions. Alternatively, it might be a consequence of gas-phase chemistry or structural transitions of the catalyst.

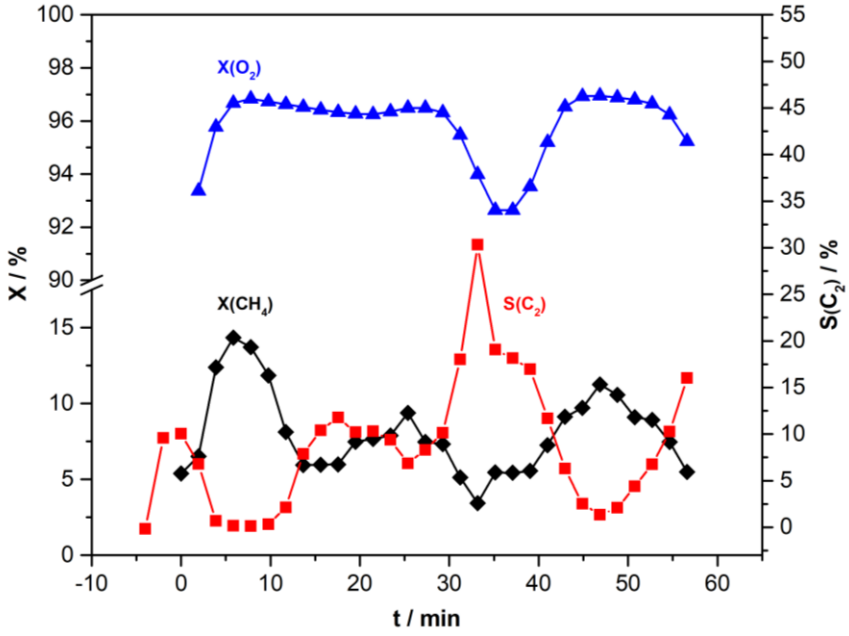

Figure 53: $X(CH_4)$, $X(O_2)$ and $S(C_2)$ for 30.0 mg of Mn-Na_2WO_4/SiO_2 catalyst in a feed of CH_4:O_2:Ar = 4:1:4 (total flow = 10 mL/min) at 685 °C (W/F = 0.0030 g*min*mL^{-1}). The reaction was performed in a Harrick reaction cell.

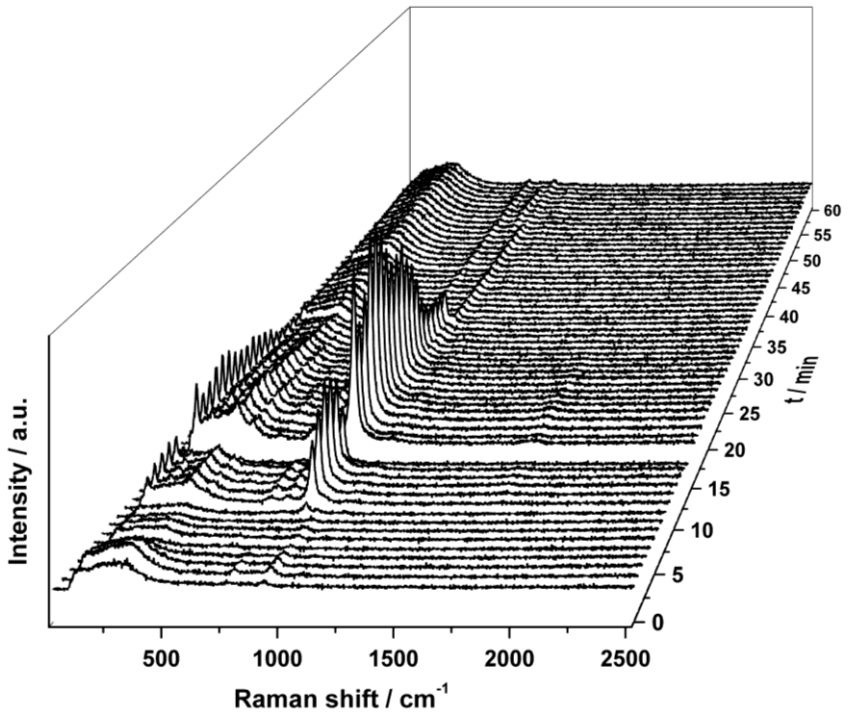

Figure 54: Uncorrected time-dependent *in-situ* Raman spectra of the Mn-Na_2WO_4/SiO_2 catalyst for t = 0−60 min of the time-on-stream experiment at 685 °C (CH_4:O_2:N_2 = 4:1:4, total flow = 10 mL/min, W/F = 0.0030 g*min*mL^{-1}). The spectrum at t = 15 min was not included.

As demonstrated by **Figure 54**, $MnWO_4$ was formed in high concentrations in the time range of 8−34 min. It then disappeared and reformed at 50−59 min. The corrected and uncorrected $MnWO_4$ peak intensities (correction by normalization to peak at 120 cm^{-1} for t = 8−34 min) were plotted against the concentration of O_2 (refer to **Figure 55**).

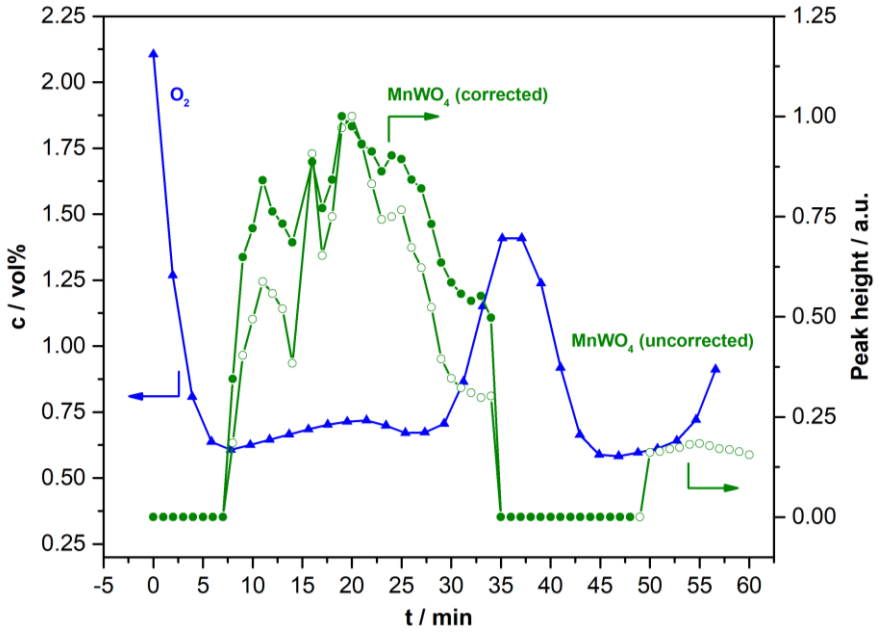

Figure 55: Correlation between the concentrations of O_2 and the formation of $MnWO_4$, as determined via Raman spectroscopy (peak heights derived after normalization to peak at 120 cm^{-1} for corrected data set) (T = 685 °C; CH_4:O_2:N_2 = 4:1:4, total flow = 10 mL/min; W/F = 0.0030 g*min*mL^{-1}).

The concentration of O_2 decreased significantly in the first 5 min after reaching 685 °C. This is connected to the increase in X(CH_4). From t = 10 min onwards, $MnWO_4$ formation is observed while the O_2 concentration remains low. It seems that the reduced concentration of O_2 in the product gas-streams is related to the appearance of $MnWO_4$ and vice-versa.

X(CH_4) and S(C_2) were also plotted together against the $MnWO_4$ peak intensity in **Figure 56**. An oscillatory behaviour of both is observed. A high conversion of CH_4 led to a reduced selectivity for C_2H_6 and C_2H_4. $MnWO_4$ appears at high CH_4 and O_2 conversion. The oscillatory behaviour of the curves, however, still needs further investigation to make valid conclusions.

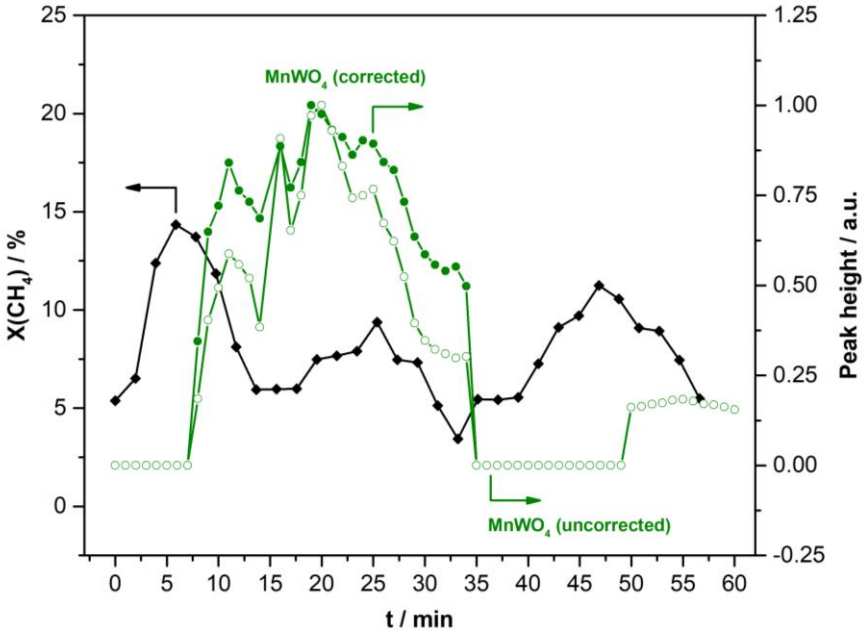

Figure 56: Correlation between the catalyst activity and the formation of $MnWO_4$, as determined via Raman spectroscopy (peak heights derived after normalization to peak at 120 cm^{-1} for corrected data set) (T = 685 °C; CH_4:O_2:N_2 = 4:1:4, total flow = 10 mL/min; W/F = 0.0030 g*min*mL^{-1}).

The Raman spectrum recorded at room temperature after the experiment featured reduced bands for the α-cristobalite support, with the bands of Na_2WO_4 also having disappeared (refer to **Figure 57**). The modes originating from Mn_7SiO_{12}, on the other hand, seem to have gained in intensity. No modes of $MnWO_4$ were detected.

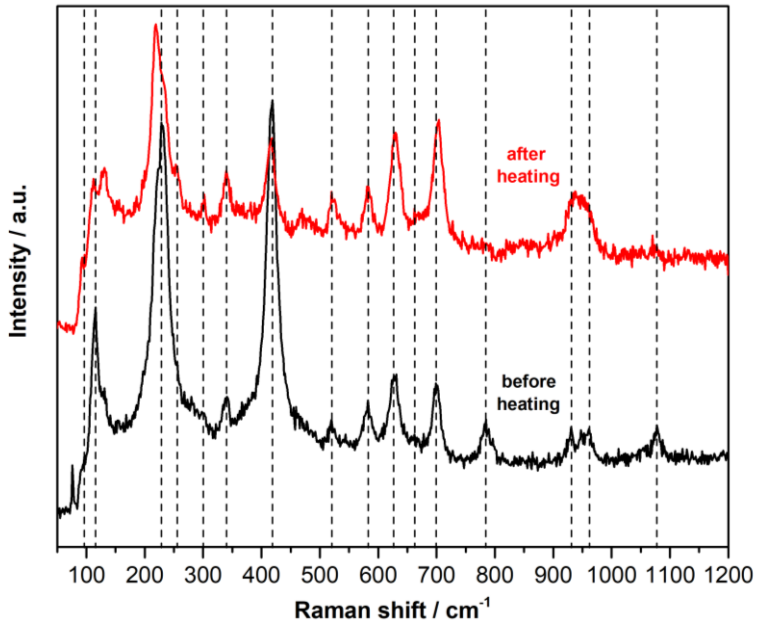

Figure 57: Raman spectra of the Mn-Na_2WO_4/SiO_2 catalyst under reaction feed (CH_4:O_2:N_2 = 4:1:4, total flow = 10 mL/min) recorded before (24 °C, black) and after heating (30 °C, red) at 457 nm (T_{max} = 685 °C). Identical peaks are marked with dotted lines.

XRD of the spent catalyst revealed an unidentified phase (**Figure 58**). Neglecting this phase, quantitative analysis showed the catalyst to be constituted 94.16 wt% α-cristobalite, 2.26 wt% quartz, 0.94 wt% Na_2WO_4 and 2.63 wt% Mn_7SiO_{12}. The amounts of Na_2WO_4 and Mn_7SiO_{12} were thus significantly lower than in the original catalyst.

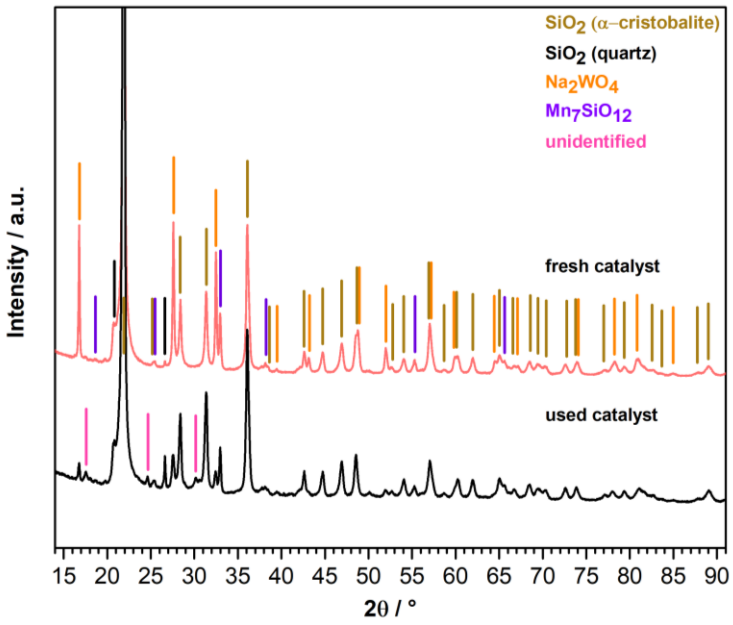

Figure 58: XRD of Mn-Na_2WO_4/SiO_2 before (red) and after reaction (black). Only new reflexes are labelled for the used catalyst.

All in all, the time-on-stream experiment confirms that $MnWO_4$ is formed under reducing conditions The exact influence of the *in-situ* generated $MnWO_4$ on the catalytic activity must be further studied. The decrease in selectivity that was observed in the first *operando* experiment could be the result of an ignition of the CH_4/O_2 mixture at high temperatures. A pronounced gas-phase radical chemistry could be the cause for the oscillatory behaviour of $X(CH_4)$ and $S(C_2)$. It is more likely, however, that this behaviour is representative for the dynamic nature of the catalyst surface, which is changing in response to the gas-phase composition - thus influencing the observed reactivity.

4.4.3 *In-situ* high temperature TEM

The structural changes of the catalyst at higher temperatures were followed by using TEM-EDX. The catalyst was heated in vacuum from room temperature until 700 °C in steps of 100 °C. A heating ramp of 10 °C/min was applied.

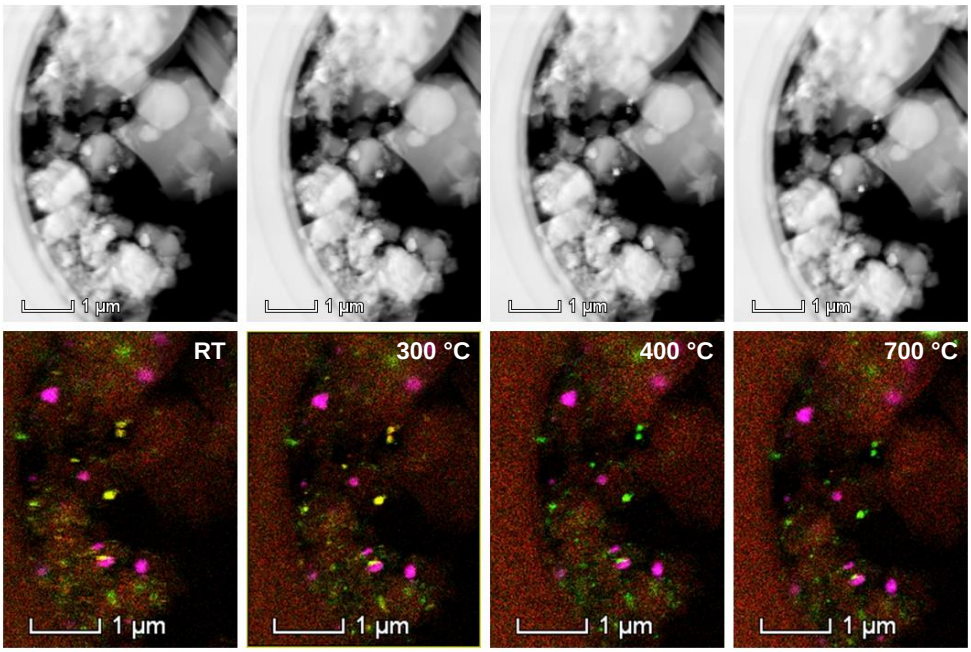

Figure 59: SE images and EDX maps of a selected catalyst area at room temperature, 300 °C, 400 °C and 700 °C recorded at 200 kV (Na given in red, Mn in pink and W in green; yellow areas results from an overlap of Na and W).

As can be seen in **Figure 59**, the supported Na_2WO_4 and Mn_7SiO_{12} phases form separate particles and are inhomogeneously distributed on the catalyst surface at room temperature. While W (green) may also exist as a dispersed WO_x species or W-clusters in addition to featuring in the Na_2WO_4 phase (yellow), Mn (pink) is only present in form of discrete Mn clusters or Mn_7SiO_{12} at given magnification. At higher temperatures, the inhomogeneously distributed particles undergo minor structural changes. Interestingly, Na disappears from the Na_2WO_4 particles between 300 °C and 400 °C, as indicated by the distinct colour change from yellow to green. By plotting the relative atomic ratios of Na, Mn and W against the temperature (refer to **Figure 60**), a general decrease in the concentration of Na is evident, with the highest decrease occurring from 300 °C to 400 °C. This may correlate with the sublimation of Na at higher temperatures or with catalyst decomposition. Since the experiment was conducted in vacuum, the effective temperature is significantly higher than indicated in the diagrams. The disappearance of Na at higher temperatures requires further investigation.

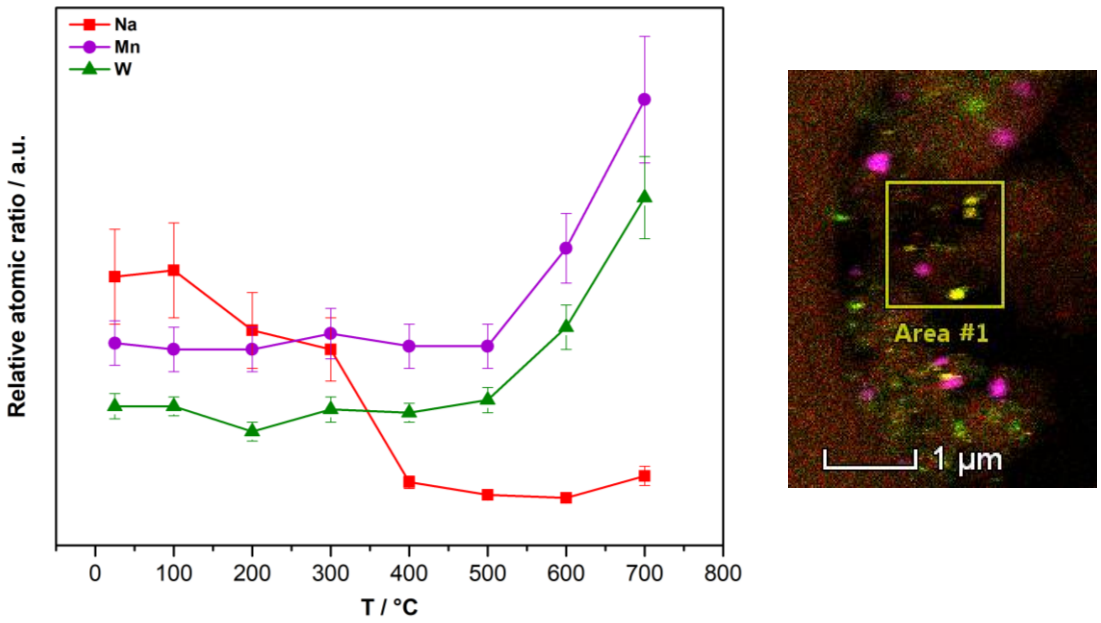

Figure 60: Relative atomic ratios of Na, Mn and W from room temperature until 700 °C. The corresponding area that was analysed is shown on the right.

5 Conclusion and Perspective

New insights into the structure and functionality of the Mn-Na_2WO_4/SiO_2 catalyst and its constituent phases are summarized as follows:

- the supported phases (Na_2WO_4, Mn_7SiO_{12}, possibly WO_x and MnO_x) are inhomogeneously distributed on the cristobalite support (SEM- and TEM-EDX) with limited structural dynamics at higher temperatures (µm-scale)
- a substantial release of oxygen (0.21 wt%) is observed for the catalyst at working temperatures (onset: 680 °C, maximum: 918 °C; TG-DSC-MS/TG-DTA-MS). A comparison with the reference samples has shown this to originate from the supported Mn_7SiO_{12} phase. Hence, Mn_7SiO_{12} is postulated to contribute to the catalysis as oxygen provider.
- a partial melting of the Na_2WO_4 phase is likely under reaction conditions (*in-situ* XRD, *in-situ* and *operando* Raman spectroscopy). The onset of this transition has been determined to lie in the range of 581-591 °C under O_2/Ar feed. This is significantly lower than the melting point of the pure substance (694 °C, TG-DSC). The melt is postulated to act as a transfer medium.
- a formation of $MnWO_4$ takes place under reducing feed conditions (CH_4/O_2/Ar, CH_4/Ar, Ar) by reaction of Mn_7SiO_{12} with Na_2WO_4 (*in-situ* and *operando* Raman spectroscopy). The melting of Na_2WO_4 may facilitate this process.
- Raman spectra recorded after *in-situ* and *operando* Raman experiments featured unidentified bands, in addition to the generated $MnWO_4$. These fall into the range of both unsupported and supported Mn oxide (MnO_x) species (450−700 cm^{-1}).[37-38, 38c, 39]
- the activity of the catalyst in *operando* Raman experiments seems to be related to the availability of highly dispersed Mn oxides species. When the activity increases, the oxygen partial pressure decreases and as a consequence, $MnWO_4$ is formed by reduction of dispersed Mn oxide. This results in fewer active sites and a lower activity.
- $MnWO_4$ is reoxidized again under these conditions, possibly explaining the oscillatory behaviour.

In order to determine the exact implications of these structural dynamics of the catalyst, further time-on-stream experiments should be performed over a longer

period of time. Furthermore, TEM/STEM-EELS studies at higher magnifications could help to identify species such as MnO_x and WO_x, which may be present in fine dispersion and/or in low concentrations on the support. While the structural synergy of all phases is likely to be responsible for the high activity and stability of the Mn-Na_2WO_4/SiO_2 catalyst system, there are indications that the redox-active Mn_7SiO_{12} phase contributes directly to the catalysis. It is likely to function as an oxygen-donor by providing mobile lattice oxygen at high temperatures. O_2 TPD experiments, such as those performed by *Gordienko et al*.[42], should be considered to further study this behaviour.

6 Experimental Section

6.1 General procedures

The Mn-Na_2WO_4/SiO_2 catalyst was prepared and supplied by U. Simon (Technische Universität Berlin).[12d] The reference samples $Na_2WO_4 \cdot 2H_2O$ and $MnWO_4$ were used as received from commercial sources (Sigma-Aldrich, 99%, LOT: 11725JD and purity Aesar, 99.9%, LOT: Y25AO43) without undergoing any further purification. The Mn_7SiO_{12} sample (origin: Langban, Sweden) that was used for Raman spectroscopy and TG-DSC measurements was supplied by Dr. Rupert Hochleitner (Mineralogische Staatssammlung München). The mineral was ground using a planetary mill. No additional purification procedures were applied.

6.2 Catalyst preparation

The Mn-Na_2WO_4/SiO_2 catalyst was prepared by Simon *et al*.[12d] at the Technische Universität Berlin following a nominal composition of 2.0 wt% Mn^{2+} ions and 4.5 wt% Na_2WO_4 on SiO_2. It was processed as concentring granulate using a fluidized bed granulator (Büchi 710, Switzerland). Amorphous SiO_2 with grain sizes ranging from 250−350 µm, purchased from Sigma-Aldrich (Silica Gel, Davisil, Grade 634), was used as catalytic support material. The fluidizing chamber of the granulator was loaded with 200 g of these nuclei. An air flux of 30 m^3/h, heated up to 80 °C, was chosen. As a result, the granules underwent fluidization. The atomisation column for coating consisted of a vertically assembled two-component nozzle (inner tube for guiding solutions and outer coaxial gas outlet). The nozzle was operated at 80 °C at a pressure of 0.07 MPa (0.7 bar). Aqueous solutions of $Mn(NO_3)_2 \cdot 4H_2O$ and of $Na_2WO_4 \cdot 2H_2O$, henceforth referred to as Mn-solution and Na/W-solution, were prepared at 70 °C in appropriate concentration. After the start up process, the aqueous Mn-solution was sprayed into the fluidizing chamber, resulting in a primary coating of Mn phases on the SiO_2 granules. Using the Na−W-solution, a second layer was applied subsequently. The concentrically coated SiO_2-granules were then heated up to 250 °C in an air atmosphere in an Al_2O_3-cruicible for 1 h, in order to remove residual water and remaining nitrates. Finally, the coated SiO_2 precursors were annealed at 800 °C for 8 h under air. All annealing procedures were performed using a heating rate of 10 K/min.

6.3 Catalyst characterization

6.3.1 X-ray fluorescence analysis (XRF)

Elemental analysis via wavelength dispersive X-ray fluorescence spectrometry was performed using a S4 Pioneer spectrometer by Bruker. It is equipped with a Rh end window X-ray tube (20−60 kV, 5−150 mA, max. 4 kW) and proportional and scintillation counters for the detection of lighter and heavier elements respectively. 8.90 g di-lithium tetraborate (> 99.995%, Aldrich) were added to 97.2 mg of the Mn-Na_2WO_4/SiO_2 catalyst for fluxing digestion in a gold hardened Pt crucible at 1300 °C (Vulcan Fusion Machine, HD Elektronik & Elektrotechnik GmbH). A pellet with a 40.0 mm diameter was obtained for analysis.

6.3.2 Inductively coupled plasma optical emission spectroscopy (ICP-OES)

Elemental analysis via ICP-OES was performed using an Optima 8300 ICP-OES system by Perkin Elmer. 10.0 mg LiF were added to 10.0 mg of the catalyst. The mixture was then dissolved in 10 mL HNO_3 (65%, Suprapur) and heated to 220 °C (60 bar, 2 h) in a microwave autoclave. The resulting solution was filled up to 50 mL with ultra-pure water and diluted again by a factor of 10 for analysis. The values presented in this work under the abbreviation TUB were measured externally at the Technische Universität Berlin.

6.3.3 X-ray diffraction (XRD)

All X-ray diffraction measurements were performed in Bragg-Brentano geometry on a Bruker AXS D8 Advance II theta/theta diffractometer, using Ni-filtered Cu Kα radiation and a position sensitive energy-dispersive LynxEye silicon strip detector. The mortared samples were filled into the recess of a cup-shaped sample holder, with the surface of the powder bed being in alignment with the sample holder edge (front loading). The measurement range was 6.0° to 140.0° (2θ). Qualitative phase identification was accomplished using the DIFFRAC.EVA software (Bruker AXS, 2010−2016) by matching the powder XRD patterns against the PDF-4+ database (ICDD, 2017). Phase quantification is based on whole pattern fitting according to the Rietveld method, using the TOPAS 5.0 program (Bruker AXS, 2014).

The *in-situ* XRD data were collected on a STOE Theta/theta X-ray diffractometer (Cu $K\alpha_{1+2}$ radiation, secondary graphite monochromator, scintillation counter) equipped with an Anton Paar XRK 900 *in-situ* reactor chamber. The measurement range was 15.0−39.0° (2θ). A step size of 0.02° and a counting time of 15 s were used. The gas feed was mixed by means of Bronkhorst mass flow controllers, using helium as inert balance gas at a total flow rate of 20 mLn/min. The effluent gas composition was monitored with a Pfeiffer OmniStar quadrupole mass spectrometer.

The *in-situ* experiment under oxidizing conditions was conducted in a feed of O_2:He = 1:8 (total flow = 20 mLn/min). 64.0 mg of mortared catalyst were used. The sample was directly heated from 25 °C to 400 °C at a heating rate of 20 °C/min. From thereon, a heating rate of 10 °C/min was applied. Temperature steps of 50 °C were maintained until 650 °C. The range of 650−750 °C was covered in 10 °C steps. An analogous temperature program was followed during cooling. A scan of 5 min was performed for each temperature step.

The experiment under reducing conditions was performed in a feed of CH_4:Ar = 4:5 (total flow = 20 mLn/min). 64.2 mg of mortared catalyst were used. Similar to the experiment under oxidizing conditions, the sample was also heated from 25 °C to 400 °C at a heating rate of 20 °C/min. Temperature steps of 100 °C and a heating rate of 10 °C were maintained until 700 °C. An analogous temperature program was followed during cooling. A scan of 10 min was performed for each temperature step.

6.3.4 Raman spectroscopy

A specially designed Raman microscope system, assembled and configured by S&I Spectroscopy & Imaging GmbH (Warstein, Germany), was used for the characterization of all samples. The experimental setup consists of a triple-spectrometer system (Princeton Instruments) combined with a TriVista confocal Raman microscope system (TriVista TR 557, Princeton Instruments) (refer to **Figure 61**). A 266 nm laser (FQCW 266) from CryLaS, 325 nm and 442 nm He-Cd lasers from Kommon Koha, a 488 nm laser (Sapphire SF) from Coherent, 355 nm, 457 nm and 532 nm single frequency continuous-wave diode-pumped lasers from Cobolt as well as 633 nm and 785 nm lasers from IPS are installed. Neutral density filters (ND) are installed to tune the laser power. 600 g/mm,

2400 g/mm and 3600 g/mm gratings are used in the case of using visible (Vis, 442 nm−532 nm) and ultraviolet lasers (UV, 266 nm−355 nm) excitations, while 150 g/mm, 300 g/mm and 1200 g/mm gratings are used in the case of near infrared (NIR, 633 nm and 785 nm) and visible lasers excitations. Scattered light signals are monitored by liquid nitrogen cooled, back-illuminated CCD detectors (PyLoN:2K and PyLoN:100 from Princeton Instruments). The PyLoN:2K detector has a 2048 x 512 imaging array (13.5 µm x 13.5 µm pixels) and is highly sensitive both in the UV and visible range (quantum efficiency, QE: 50%−70%). The PyLoN:100 detector possesses a 1340 x 100 imaging array (20 µm x 20 µm pixels) and is highly sensitive both in the visible and NIR range (QE > 80%). A resolution of 1 cm^{-1} is given. For spectrometer frequency calibration, a silicon wafer (520.7 ± 0.5 cm^{-1}) is applied.

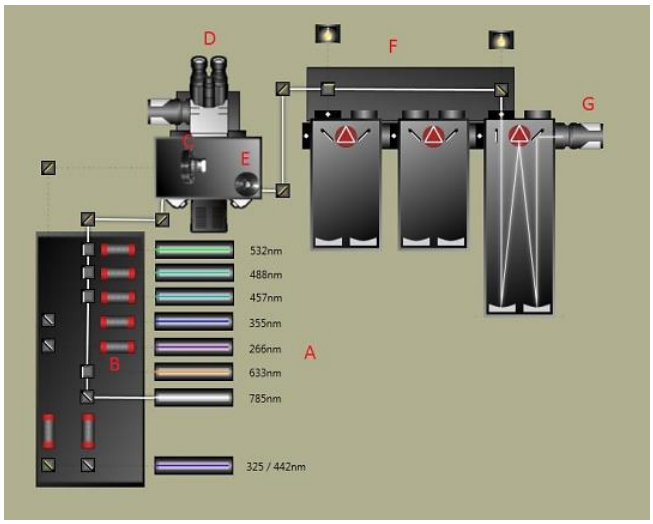

Figure 61: Schematic diagram of the multi-laser Raman spectroscopy setup. A: laser source; B: beam expander; C: neutral density filter; D: optical microscope; E: edge filter; F: TriVista triple grating spectrometers; G: liquid nitrogen cooled CCD detector.

A single-stage configuration using edge filters was adopted for all measurements. The Raman spectroscopic investigation of all samples was performed at 457 nm excitation wavelength. Unless stated otherwise, a laser power of 0.459 mW, a 600 g/mm grating and a 100 µm slit entrance were applied. A x10 microscope objective was used to focus the incident beam on the sample. The exposure time is documented in the Results section. All samples were mortared prior to investigation. The sample position was maintained if not stated otherwise. The system configuration (laser, objective, software settings) was varied for the multi-wavelength approach. Temperatures and heating rates for the *in-situ and operando* experiments are given in the Results section.

In-situ measurements

The *in-situ* measurements in Ar, O_2/Ar and O_2/N_2 feed were conducted in a commercial CCR1000 reaction cell from Linkam Scientific Instruments (refer to **Figure 62**). The gas flows from the top to the bottom of the cell, passing through the powder sample that is supported by a ceramic fibre filter (96% Al_2O_3/4% SiO_2, non-woven fabric) in a ceramic sample holder. Two thermocouples are present in the reaction chamber. One is located along the inner wall of the sample holder for temperature control (Tc1), while another is inserted into the sample from below to measure the actual temperature (Tc2). For each measurement, 10 mg of mortared sample were placed in the ceramic holder. After loading the sample, the surface was evened out. The sample was then flushed with feed gas for 20 minutes before starting the first measurement.

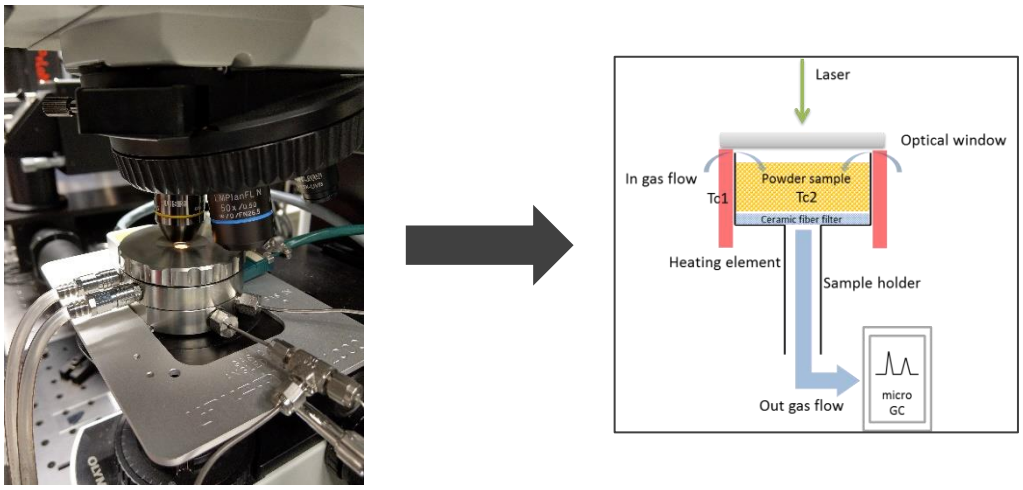

Figure 62: Schematic representation of the Linkam CCR1000 reaction cell.

In-situ measurements in CH_4/Ar, were performed in a HVC-MRA-5 cell from Harrick Scientific Instruments using the same amount of sample (refer to **Figure 63**Figure 62). In the applied set-up, the gas flows from the bottom to the top of the cell, passing through the powder sample that is supported by a mesh. The cell temperature is controlled by an external temperature controller from Harrick Scientific Instruments. Calibration was performed using a thermocouple that was placed in between the window lid and the cell body, touching the surface of the catalyst. The nominal temperature of the reaction chamber was logged over the entire course of the experiment and then converted into the actual temperature using a calibration function.

Operando measurements

The *operando* measurements in $CH_4/O_2/Ar$ or $CH_4/O_2/N_2$ were also conducted in the HVC-MRA-5 cell from Harrick Scientific Instruments using an identical configuration. 30 mg of mortared sample were loaded into the cell and evened out. The sample was flushed with feed gas for 20 minutes.

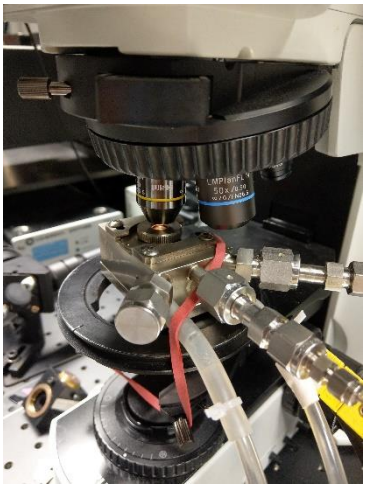

Figure 63: The Harrick HVC-MRA-5 reaction cell used in the characterization of Mn-Na_2WO_4/SiO_2.

Contrary to the *in-situ* experiments, the outgoing gas of the Harrick cell was connected to a micro-GC (Varian CP-4900 or Agilent 490 Micro GC) performing on-line gas product analysis. The conversion of methane X and the product selectivity S_{C2} were calculated based on the sum of products as follows [Eq. (1) and (2)]:

$$X = \frac{n^0_{CH_4} - n_{CH_4}}{n^0_{CH_4}} \quad (1)$$

$$S_{C2} = \frac{0.5\, n_{C_2H_6} + 0.5\, n_{C_2H_4}}{n^0_{CH_4} - n_{CH_4}} \quad (2)$$

6.3.5 Scanning electron microscopy and energy-dispersive X-ray analysis (SEM-EDX)

A Hitachi S-4800 field emission scanning electron microscope operating in the range of 0.1 to 30 kV (acceleration voltage) in secondary electron (SE) mode was applied. It features a cold field emission gun and produces a maximum resolution of 1.4 nm, 1.0 nm and 1.0 nm for acceleration voltages of 1 kV, 15 kV and 30 kV (STEM mode) respectively. Morphology studies were performed at a voltage of 1.5 kV and a working distance of 3.0 mm. For this, the sample was applied to

double-sided adhesive, conductive carbon tape, which was then stuck onto a carbon disc to reduce the background signal. The energy dispersive X-ray analysis data was collected with an integrated Bruker EDX QUANTAX 800 system (with XFlash®6) applying a SDD (silicon drift detector) detector. For X-ray analysis, an excitation voltage of at least two times the highest peak energy for the elements of interest was applied. The voltage was set at 20 kV for all EDX measurements, resulting in an average interaction depth of 2.8 µm. The working distance for the detection of X-rays was optimized to 10.0 mm due to the geometry of the system.

6.3.6 Transmission electron microscopy and energy-dispersive X-ray analysis (TEM-EDX)

Data acquisition and imaging was performed on a FEI Talos F200X transmission/scanning transmission electron microscope (S/TEM) equipped with a Super X-EDXS detector. The system was operated at 200 kV (acceleration voltage). The samples were prepared by the drop casting deposition method. The mortared catalyst was dispersed in isopropanol. Few drops of this suspension were then placed on a heating and biasing FEI MEMS chip. For high temperature characterisation, a FEI heating and biasing holder was used. The sample was heated from room temperature until 700 °C in 100 °C steps at a rate of 10 °C/min. For EDX data quantification, spectra deconvolution was applied using the Velox™ S/TEM software. Simultaneous EDX data acquisition and imaging was performed in the STEM microscope operating mode. All images were acquired with a HAADF detector.

6.3.7 N_2-physisorption (Brunauer-Emmett-Teller, Multipoint-BET)

Nitrogen adsorption was performed at −196 °C using a Quantachrome Autosorb-6B-MP system after outgassing the catalyst (53.7 mg) in vacuum for 12 h at 150 °C. All data treatments were performed using the Quantachrome Autosorb software package. The specific surface area S_{BET} was calculated according to the multipoint BET method in the p/p_0=0.06–0.29 pressure range assuming the N_2 cross sectional area of 16.2 $Å^2$. An adsorption/desorption isotherm consisting of 79 measurement points was recorded in the p/p_0 range of 0.04−1.0 to evaluate the microporosity of the sample.

6.3.8 Thermogravimetry and differential scanning calorimetry or differential thermal analysis (TG-DSC/TG-DTA)

Thermogravimetric studies were conducted using a NETZSCH STA 449 C *Jupiter* apparatus, which features a top-loading thermo-microbalance (TG) with a true heat flux differential scanning calorimeter (DSC) for simultaneous TGA-DSC. The system is connected to a Pfeiffer Vacuum ThermoStar GSD 301 T for additional mass spectrometry analysis.

The reference samples were all analysed according to a similar procedure. 34.6 mg of Na_2WO_4 were placed in a DSC sample holder and heated to 700 °C at a heating rate of 5 °C/min in Ar (100 mL/min). The temperature was maintained for 1 h.

In the case of Mn_7SiO_{12}, 17.6 mg of the sample were heated to 1000 °C in a DSC sample holder at a heating rate of 5 °C/min in Ar (100 mL/min). The temperature was maintained for 1 h.

For the characterisation of $MnWO_4$, 31.2 mg were placed in a DSC sample holder and heated to 1000 °C at a heating rate of 5 °C/min in Ar (100 mL/min). The maximum temperature was maintained for 1 h.

For the measurement of the Mn-Na_2WO_4/SiO_2 catalyst in synthetic air, 16.5 mg were placed in a DSC sample holder and heated to 900 °C at a continuous heating rate of 10 °C/min (Ar:O_2 = 79:21, total flow rate = 100 mL/min). After reaching the maximum temperature, the sample was cooled to 30 °C at a rate of 5 °C/min.

The measurement in Ar was performed with 104.5 mg of the catalyst, which were placed in a DTA sample holder and pre-treated in synthetic air (21% O_2 in Ar, 100 mL/min) at 500 °C for 1 h (heating rate: 10 °C/min). H_2O, CO_2 and carbonaceous deposits were consequently removed from the surface. For the actual TG-DTA, the sample was heated to 1000 °C at a continuous heating rate of 5 °C/min in Ar (total flow rate = 70 mL/min). The temperature was maintained for 1 h.

6.4 Catalytic activity test

The catalytic activity of the Mn-Na_2WO_4/SiO_2 catalyst in the oxidative coupling of methane was studied by using a setup for partial oxidation (Integrated Lab Solutions) with eight fixed-bed quartz reactors (6 mm inner diameter) in parallel. Each reactor was equipped with a thermocouple for measuring the temperature inside the catalyst bed. The catalytic performance was determined at atmospheric pressure under steady state conditions. The applied temperature range for the reaction was 700−750 °C. The reaction temperature was not increased above 750 °C to avoid catalyst decomposition. The reactor was first heated up to 700 °C at a heating rate of 5 °C/min under reactant gas flow, followed by a stepwise increase to 725 °C and 750 °C respectively. The reactant feed comprised CH_4, O_2 and He as diluent in a ratio of 4:1:4 (40 mL/min total flow). The Mn-Na_2WO_4/SiO_2 catalyst was sieved to a particle size of 250−355 mm. 100 mg of the catalyst were loaded into the reactor without prior dilution for direct comparison with the *operando* Raman experiments that were performed thereafter. Contact time variation was performed at a fixed temperature of 750 °C by variation of the gas flow (40, 60 and 80 mL/min). The calculated pressure drop was below 0.5 mbar for all loadings. An online gas chromatograph (Agilent 7890A) was used for gas analysis. A combination of Plot-Q (length 30 m, 0.53 mm internal diameter, 40 mm film thickness) and Plot-MoleSieve 5A columns (30 m length, 0.53 mm internal diameter, 50 mm film thickness), connected to a thermal conductivity detector (TCD), was used to analyse the permanent gases CH_4, O_2, CO, CO_2 and He. A system of a FFAP (length 30 m, 0.53 mm internal diameter, 1 mm film thickness) and a Plot-Q column (length 30 m, 0.53 mm internal diameter, 40 mm film thickness), connected to a flame ionization detector (FID), was used to analyse C_2−C_3 hydrocarbons and oxygenates. The carbon balance always equaled 100%. The conversion of methane X and the product selectivity S_k were calculated based on the sum of products as follows [Eq. (3) and (4)]:

$$\mathrm{X} = \frac{\sum_{i=1}^{n} \frac{n_i(\mathrm{product})}{|\nu_i|}}{\sum_{j=1}^{k} \frac{n_j(\mathrm{C-compound})}{|\nu_j|}} \tag{3}$$

$$\mathrm{S}_k = \frac{N_k(\mathrm{C-atoms}) \times n_k(\mathrm{product})}{\sum_{i=1}^{n} N_i(\mathrm{C-atoms}) \times n_i(\mathrm{product})} \, , k = 1 \ldots n \tag{4}$$

7 Supporting Information

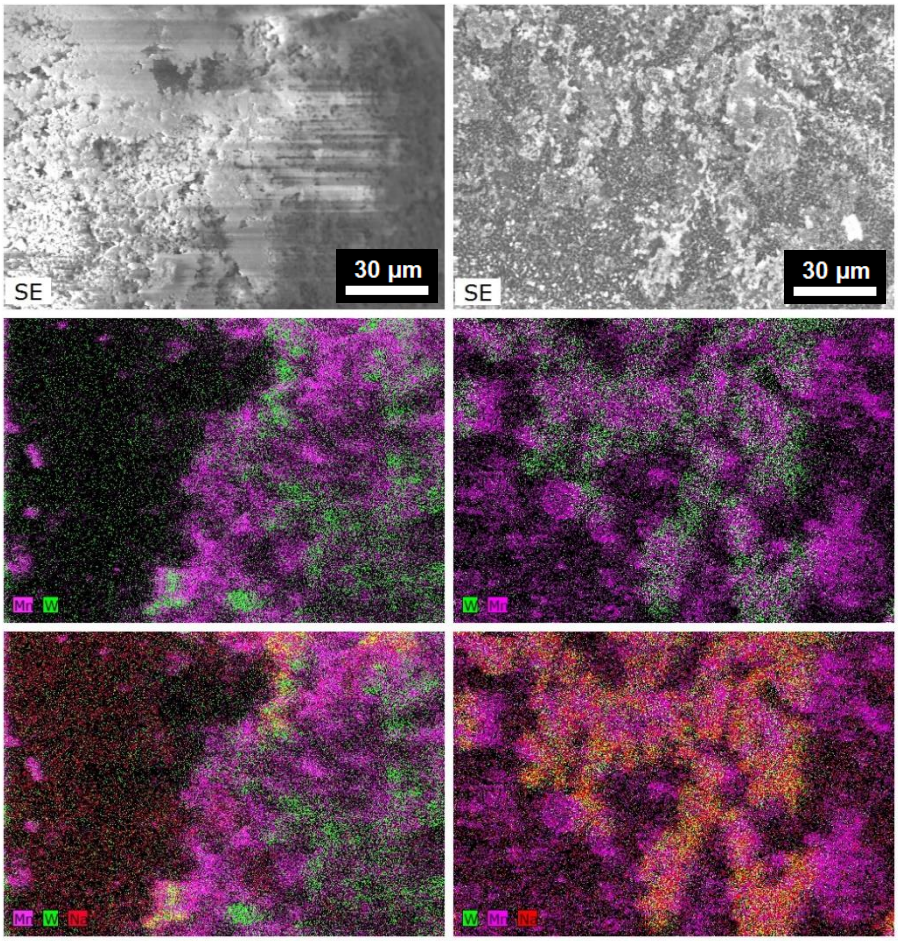

Figure 64: SE images and EDX mapping of W, Mn and Na for two selected catalyst areas (map 1: left, map 2: right; acceleration voltage: 20 kV, magnification: x1.0k, working distance: 10 mm, average interaction depth: 2.8 µm). Na_2WO_4-rich areas are yellow due to the overlap of the respective colours for Na and W. The SE image of map 1 indicates strong charging of the SiO_2 support.

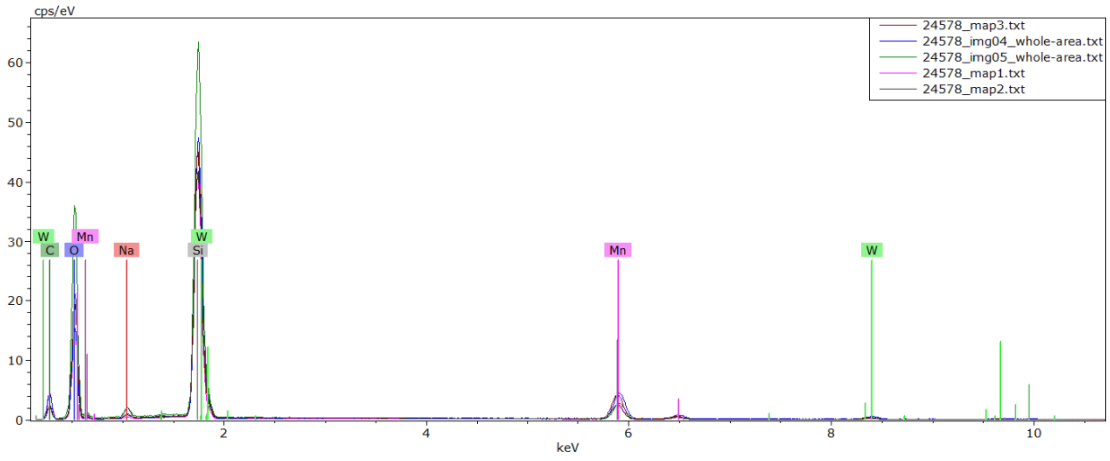

Figure 65: EDX spectra of five selected areas of the Mn-Na_2WO_4/SiO_2 catalyst (acceleration voltage: 20 kV, magnification: x1.0k, working distance: 10 mm, average interaction depth: 2.8 µm).

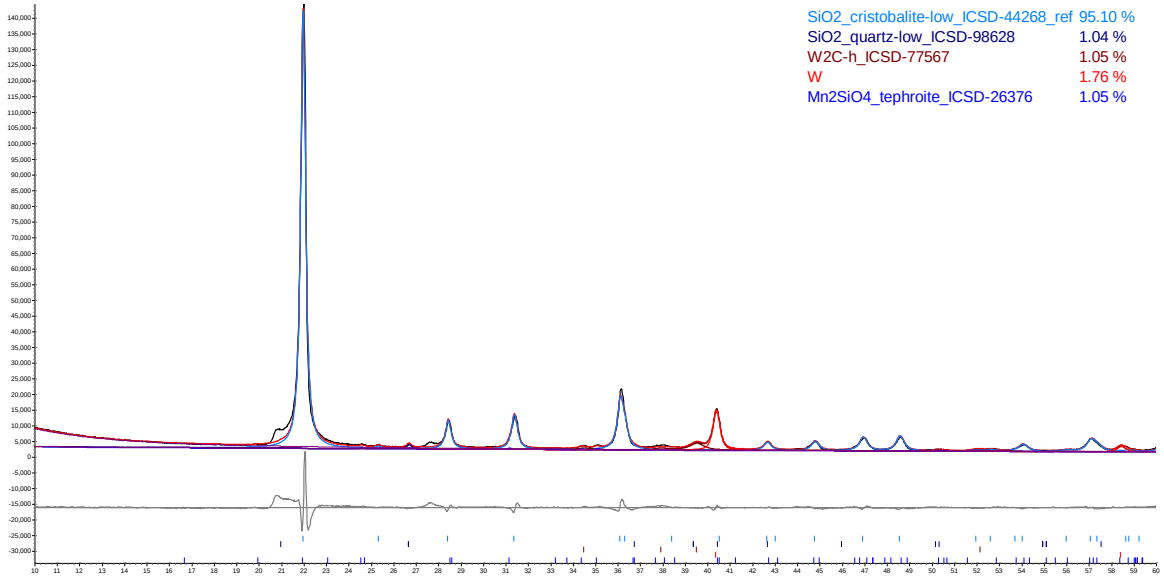

Figure 66: Room temperature XRD of the spent Mn-Na_2WO_4/SiO_2 catalyst after the *in-situ* XRD experiment under reducing conditions (CH_4:He = 4:5, 20 mLn/min, W/F = 0.0032 g*min*mLn-1).

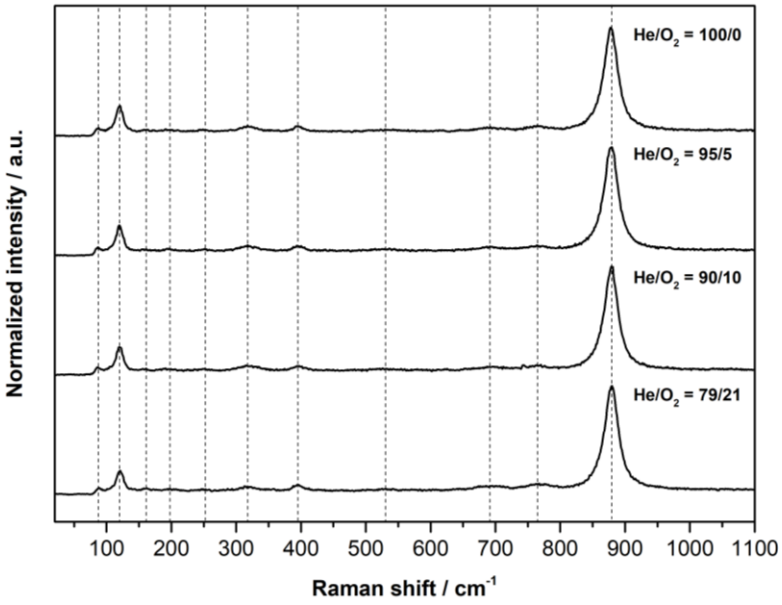

Figure 67: Raman spectra of $MnWO_4$ recorded at 710 °C at different partial pressures of O_2 (457 nm, exposure time = 3 min).

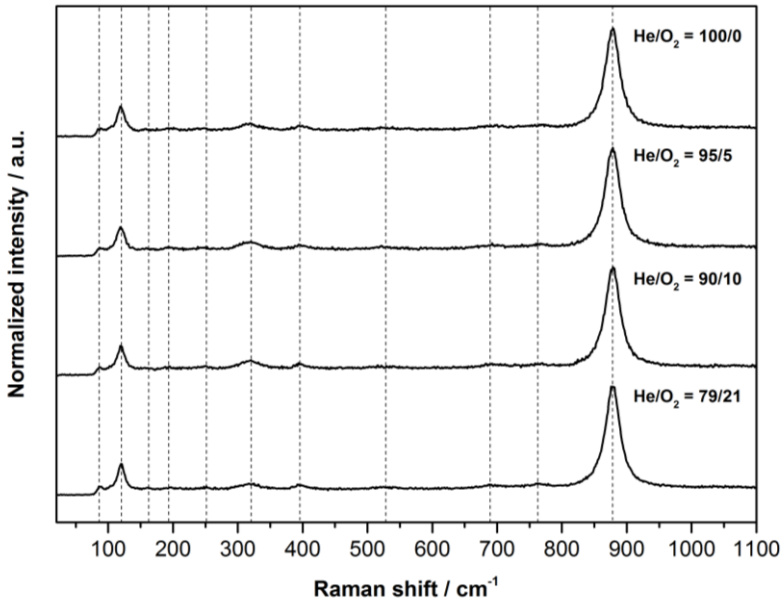

Figure 68: Raman spectra of $MnWO_4$ recorded at 753 °C at different partial pressures of O_2 (457 nm, exposure time = 3 min).

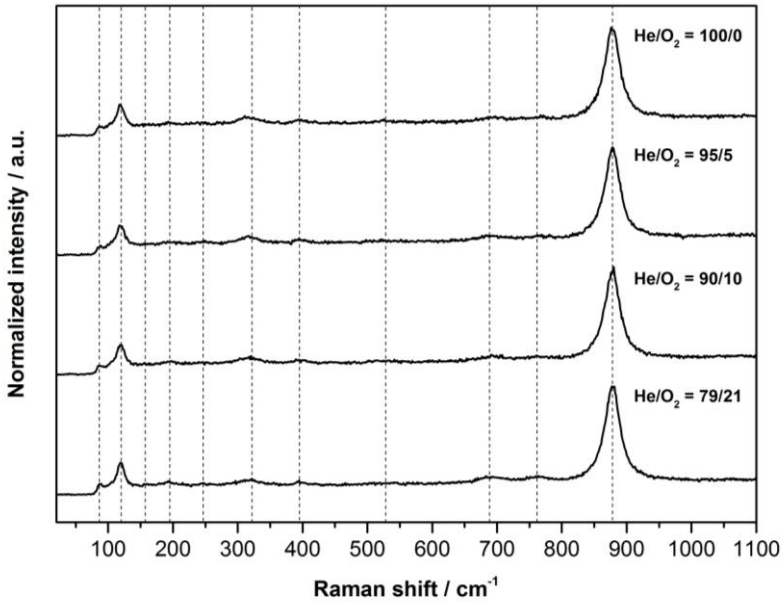

Figure 69: Raman spectra of $MnWO_4$ recorded at 802 °C at different partial pressures of O_2 (457 nm, exposure time = 3 min).

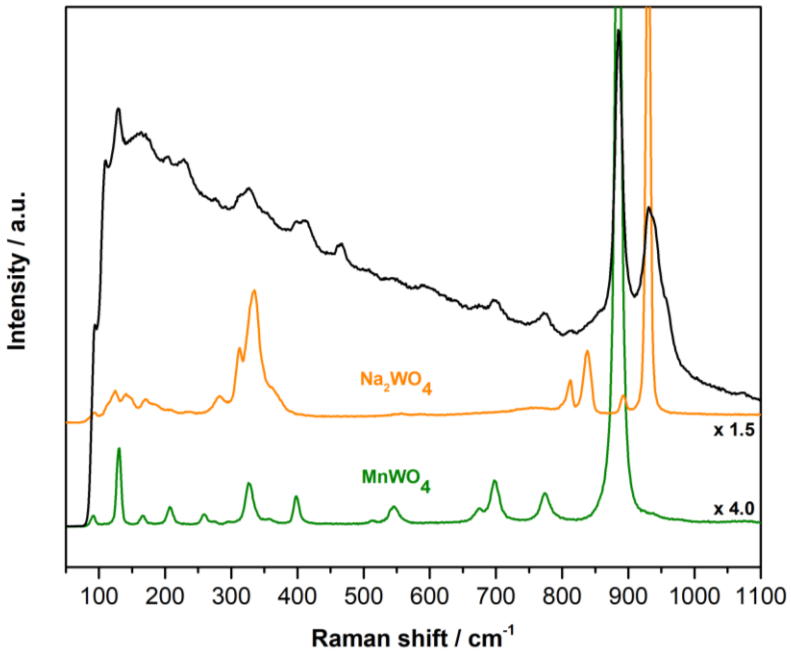

Figure 70: Raman spectrum of Mn-Na_2WO_4/SiO_2 recorded after equilibration (740 °C) at 91 °C under Ar flow (10 mL/min) (457 nm). The reference spectra for Na_2WO_4 (orange) and $MnWO_4$ (green) at 23 °C (457 nm, $He:O_2$ = 79:21, total flow = 10 mL/min) were included for signal allocation (exposure time = 7.5 min).

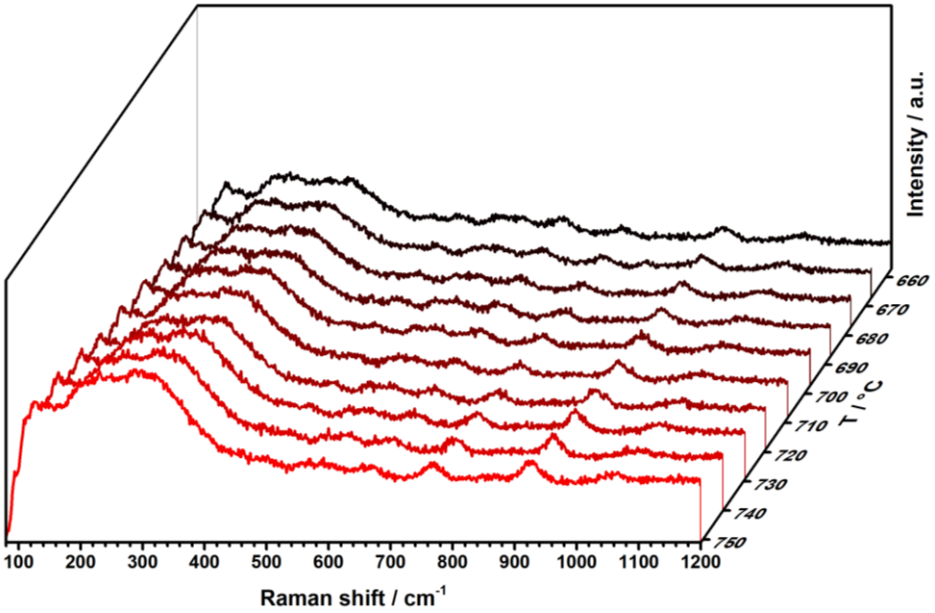

Figure 71: Raman spectra of the unequilibrated Mn-Na_2WO_4/SiO_2 catalyst in O_2:Ar = 1:8 (total flow = 10 mL/min) recorded from 657 °C to 751 °C at 457 nm (exposure time = 7.5 min).

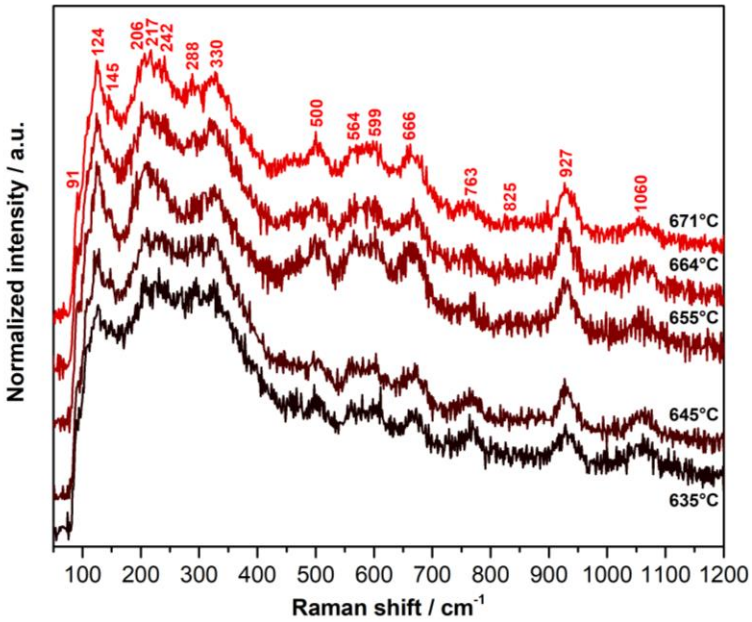

Figure 72: Raman spectra of Mn-Na_2WO_4/SiO_2 recorded from 635 to 671 °C at 457 nm under reaction conditions (CH_4:O_2:Ar = 4:1:4, total flow = 10 mL/min, W/F = 0.0030 g*min*mL^{-1}, exposure time = 10 min). The spectra were normalized to the intensity of the highest peak.

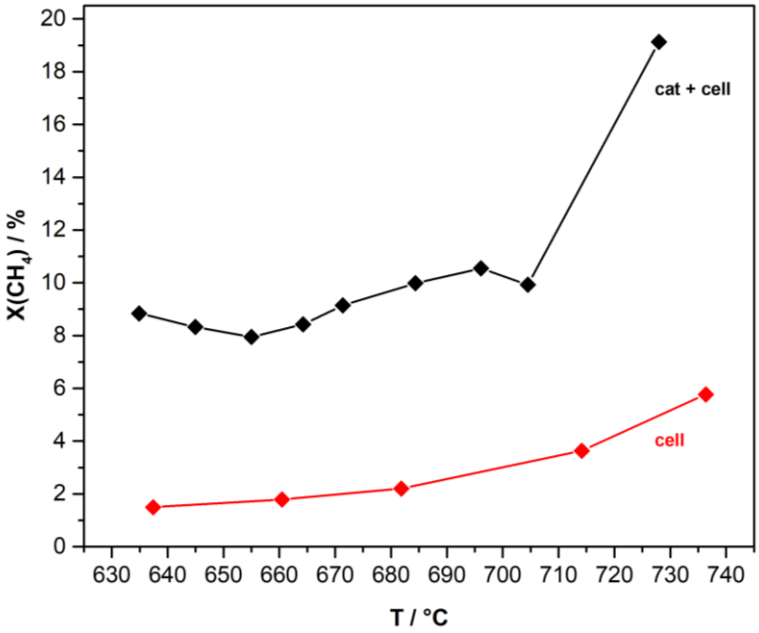

Figure 73: Methane conversion of the Harrick reaction cell in comparison to the catalyst. For the reaction, 30.0 mg of the Mn-Na_2WO_4/SiO_2 catalyst were used in a feed of CH_4:O_2:Ar = 4:1:4 (total flow = 10 mL/min) (W/F = 0.0030 g*min*mL^{-1}).

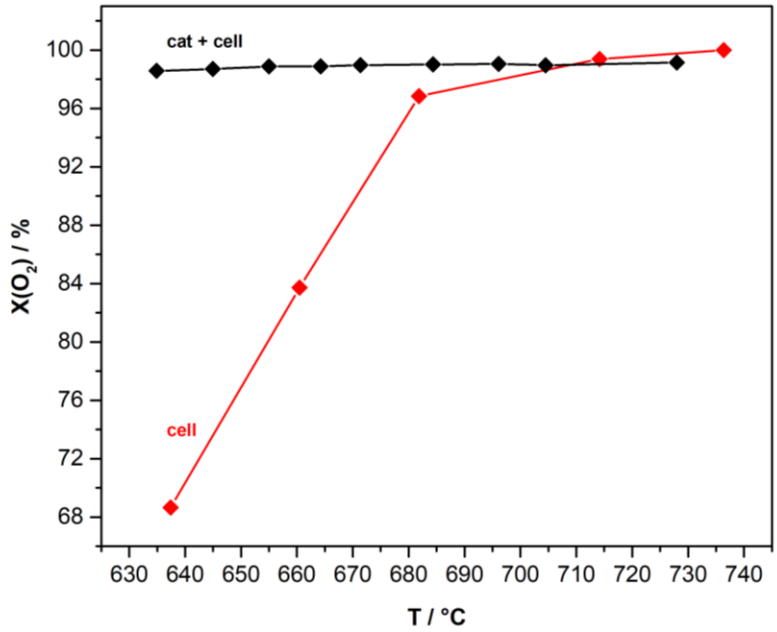

Figure 74: $X(O_2)$ for the reaction cell and the catalyst + reaction cell in a feed of CH_4:O_2:Ar = 4:1:4 (total flow = 10 mL/min) (W/F = 0.0030 g*min*mL^{-1}).

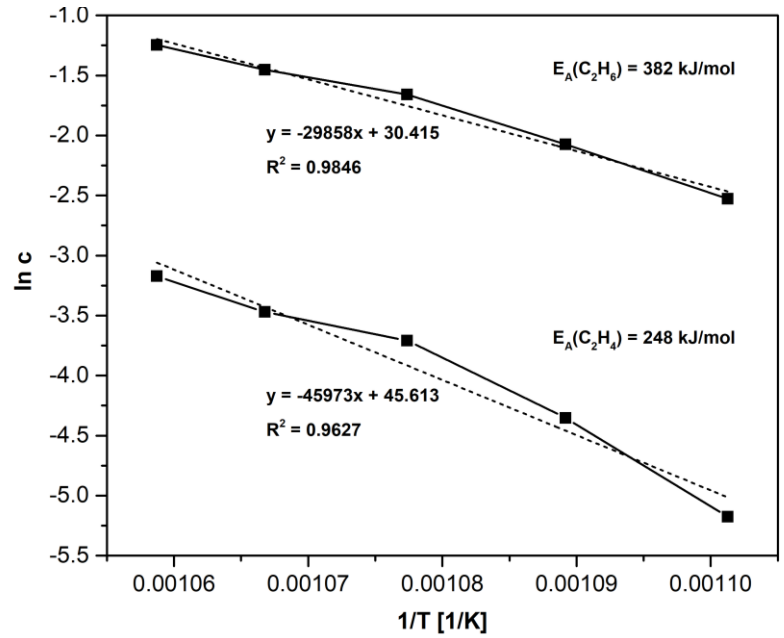

Figure 75: Determination of the activation energies for C_2H_6 and C_2H_4 formation based on the experimental data of the *operando* experiment with the Mn-Na_2WO_4/SiO_2 catalyst.

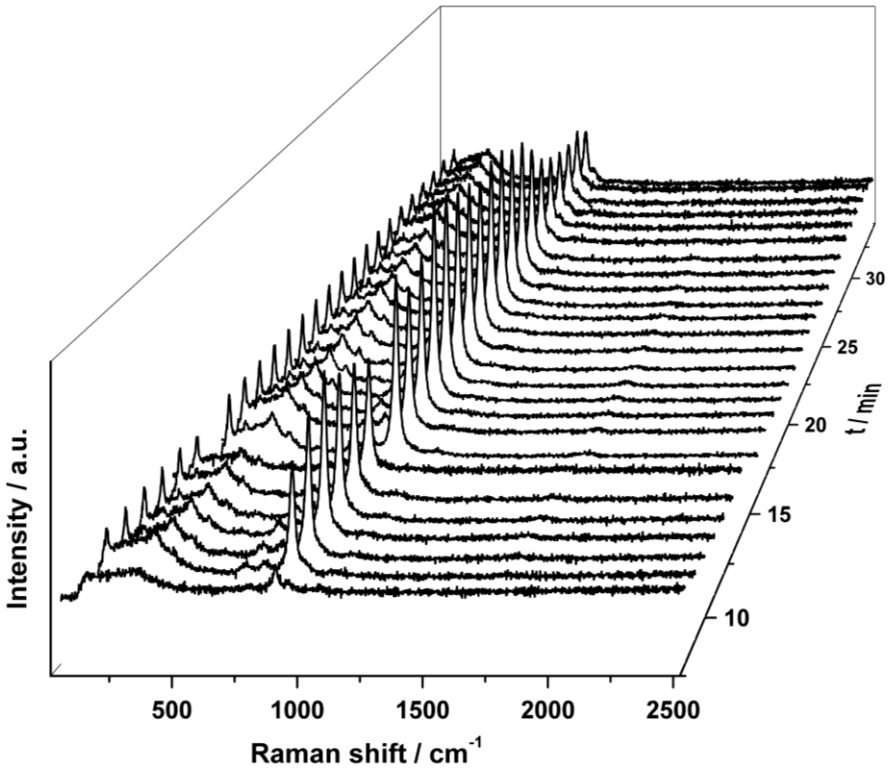

Figure 76: Time-dependent *in-situ* Raman spectra of the Mn-Na_2WO_4/SiO_2 catalyst for t = 8−34 min of the time-on-stream experiment at 685 °C (CH_4:O_2:N_2 = 4:1:4, total flow = 10 mL/min, W/F = 0.0030 g*min*mL^{-1}). The spectra were normalized to the 120 cm^{-1} peak. The spectrum at t = 15 min was not included.

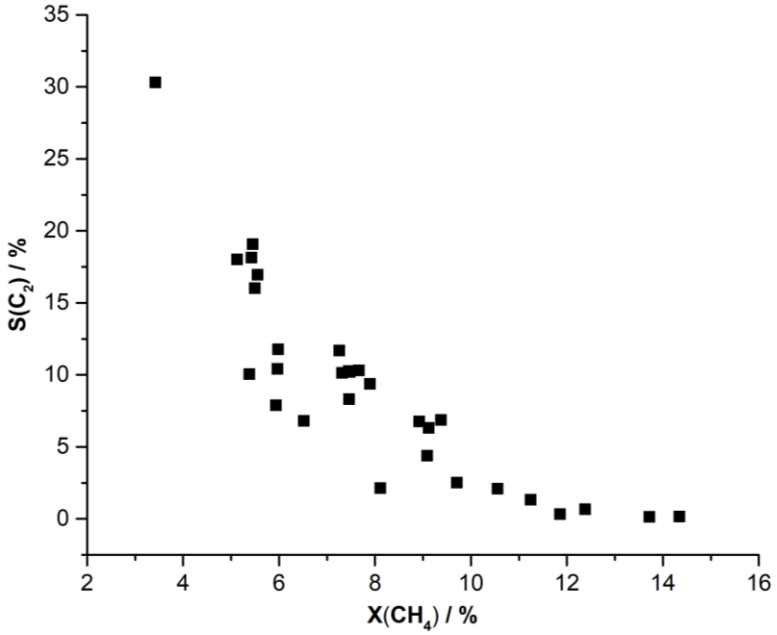

Figure 77: X *versus* S plot for the Mn-Na_2WO_4/SiO_2 catalyst. Data was derived from the time-on-stream experiment at 685 °C (CH_4:O_2:N_2 = 4:1:4, total flow = 10 mL/min, W/F = 0.0030 g*min*mL^{-1}).

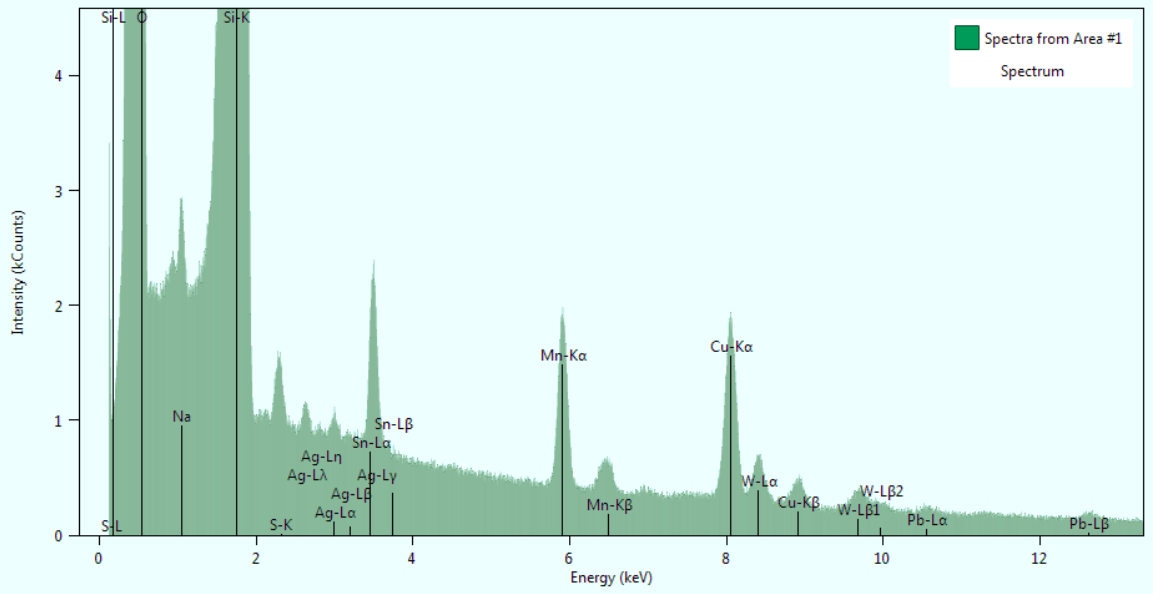

Figure 78: TEM-EDX spectrum of the Mn-Na_2WO_4/SiO_2 catalyst at room temperature. Cu originates from the sample holder and microscope. Ag can be attributed to the sample holder while the Sn signals can be interpreted as artefacts induced by the Si X-rays. A contamination of the sample with S was also observed.

8 References

[1] P. Schwach, X. Pan, X. Bao, *Chemical reviews* **2017**, *117*, 8497-8520.

[2] a) BP, *BP Statistical Review of World Energy June 2017* **2017**; b) E. McFarland, *Science* **2012**, *338*, 340-342.

[3] a) P. F. van den Oosterkamp, *Encyclopedia of Catalyis, Vol. 6*, Wiley-VCH, Weinheim, **2003**; b) J. H. Lunsford, *Catalysis Today* **2000**, *63*, 165-174.

[4] *Ullmann's Encyclopedia of Industrial Chemistry, Cyano Compounds, Inorganic, Vol. 10*, Wiley-VCH, Weinheim, **2003**.

[5] L. Wang, L. Tao, M. Xie, G. Xu, J. Huang, Y. Xu, *Catalysis Letters* **1993**, *21*, 35-41.

[6] J. J. Spivey, G. Hutchings, *Chem Soc Rev* **2014**, *43*, 792-803.

[7] C. Karakaya, R. J. Kee, *Progress in Energy and Combustion Science* **2016**, *55*, 60-97.

[8] X. Guo, G. Fang, G. Li, H. Ma, H. Fan, L. Yu, C. Ma, X. Wu, D. Deng, M. Wei, D. Tan, R. Si, S. Zhang, J. Li, L. Sun, Z. Tang, X. Pan, X. Bao, *Science* **2014**, *344*, 616-619.

[9] G. E. Keller, M. M. Bhasin, *Journal of Catalysis* **1982**, *73*, 9-19.

[10] W. Hinsen, M. Baerns, *Chemiker-Zeitung* **1983**, *107*, 223-226.

[11] T. Ito, J. H. Lunsford, *Nature* **1985**, *314*, 721.

[12] a) S. Arndt, T. Otremba, U. Simon, M. Yildiz, H. Schubert, R. Schomäcker, *Applied Catalysis A: General* **2012**, *425-426*, 53-61; b) J. Lin, J. Gu, D. Yang, C. Zhang, Y. Yang, Y. Chu, S. Li, *Shiyou Huagong* **1995**, *24*, 293-298; c) X. L. Wang, J. N. Zhang, D. X. Yang, C. W. Zhang, J. Z. Lin, S. B. Li, *Shiyou Huagong* **1997**, *26*, 361–367; d) U. Simon, O. Görke, A. Berthold, S. Arndt, R. Schomäcker, H. Schubert, *Chemical Engineering Journal* **2011**, *168*, 1352-1359; e) S. Pak, P. Qiu, J. H. Lunsford, *Journal of Catalysis* **1998**, *179*, 222-230; f) H. Liu, X. Wang, D. Yang, R. Gao, Z. Wang, J. Yang, *Journal of Natural Gas Chemistry* **2008**, *17*, 59-63.

[13] E. V. Kondratenko, M. Baerns, in *Handbook of Heterogeneous Catalysis*, Wiley-VCH Verlag GmbH & Co. KGaA, **2008**.

[14] D. J. Driscoll, W. Martir, J. X. Wang, J. H. Lunsford, *Journal of the American Chemical Society* **1985**, *107*, 58-63.

[15] O. V. Buyevskaya, M. Rothaemel, H. W. Zanthoff, M. Baerns, *Journal of Catalysis* **1994**, *146*, 346-357.

[16] a) M. Baerns, E. E. E. Wolf, *Methane Conversion by Oxidative Processes - Fundamental and Engineering Aspects.*, Springer Netherlands, **1992**; b) V. Sokolovskii, E. Mamedov, *ChemInform* **1992**, *23*; c) O. V. Krylov, *Catalysis Today* **1993**, *18*, 209-302.

[17] G. Ertl, H. Knözinger, F. Schüth, J. Weitkamp, *Handbook of Heterogeneous Catalysis. 2nd Edition*, Wiley-VCH, Weinheim, **2008**.

[18] a) A. M. Maitra, *Applied Catalysis A: General* **1993**, *104*, 11-59; b) J. H. Lunsford, *Angewandte Chemie International Edition in English* **1995**, *34*, 970-980; c) E. E. Wolf, *Methane Conversion by Oxidative Processes - Fundamental and Engineering Aspects.*, Springer Netherlands, **1992**.

[19] a) L. Mleczko, M. Baerns, *Fuel Process. Technol.* **1995**, *42*, 217-248; b) B. L. Farrell, V. O. Igenegbai, S. Linic, *ACS Catalysis* **2016**, *6*, 4340-4346.

[20] U. Zavyalova, M. Holena, R. Schlögl, M. Baerns, *ChemCatChem* **2011**, *3*, 1935-1947.

[21] a) X. P. Fang, S. B. Li, J. Z. Lin, Y. L. Chu, *Journal of Molecular Catalysis (in Chinese)* **1992**, *6*, 427-433; b) X. P. Fang, S. B. Li, J. Z. Lin, J. F. Gu, D. X. Yan, *Journal of Molecular Catalysis (in Chinese)* **1992**, *6*, 255-262.

[22] a) S.-f. Ji, T.-c. Xiao, S.-b. Li, C.-z. Xu, R.-l. Hou, K. S. Coleman, M. L. H. Green, *Applied Catalysis A: General* **2002**, *225*, 271-284; b) S. Ji, T. Xiao, S. Li, L. Chou, B. Zhang, C. Xu, R. Hou, A. P. E. York, M. L. H. Green, *Journal of Catalysis* **2003**, *220*, 47-56.

[23] Z. C. Jiang, C. J. Yu, X. P. Fang, S. B. Li, H. L. Wang, *The Journal of Physical Chemistry* **1993**, *97*, 12870-12875.

[24] D. J. Wang, M. P. Rosynek, J. H. Lunsford, *Journal of Catalysis* **1995**, *155*, 390-402.

[25] Z. C. Jiang, H. Gong, S. B. Li, *Methane activation over Mn2O3-Na2WO4/SiO2 catalyst and oxygen spillover, Vol. 112*, **1997**.

[26] A. Palermo, J. P. Holgado Vazquez, A. F. Lee, M. S. Tikhov, R. M. Lambert, *Journal of Catalysis* **1998**, *177*, 259-266.

[27] Y. Kou, B. Zhang, J.-z. Niu, S.-b. Li, H.-l. Wang, T. Tanaka, S. Yoshida, *Journal of Catalysis* **1998**, *173*, 399-408.

[28] S. Hou, Y. Cao, W. Xiong, H. Liu, Y. Kou, *Industrial & Engineering Chemistry Research* **2006**, *45*, 7077-7083.

[29] V. Salehoun, A. Khodadadi, Y. Mortazavi, A. Talebizadeh, *Chemical Engineering Science* **2008**, *63*, 4910-4916.

[30] a) I. P. Swainson, M. T. Dove, D. C. Palmer, *Physics and Chemistry of Minerals* **2003**, *30*, 353-365; b) N. J.-Z. Chen Hong-Shan, Xia Chun-Gu, Li Shu-Ben, *Acta Physico-Chimica Sinca* **2000**, *16*, 543-546; c) P. Richet, B. O. Mysen, *Geophysical Research Letters* **1999**, *26*, 2283-2286; d) J. B. Bates, *The Journal of Chemical Physics* **1972**, *57*, 4042-4047; e) G. D. Saraiva, C. Luz-Lima, P. T. C. Freire, A. J. Ramiro de Castro, G. P. de Sousa, F. E. A. Melo, J. H. Silva, J. Mendes Filho, *Journal of Molecular Structure* **2013**, *1033*, 154-161; f) C. L. Lima, G. D. Saraiva, P. T. C. Freire, M. Maczka, W. Paraguassu, F. F. de Sousa, J. Mendes, *J. Raman Spectrosc.* **2011**, *42*, 799-802; g) R. C. Dai, X. Ding, Z. P. Wang, Z. M. Zhang, *Chemical Physics Letters* **2013**, *586*, 76-80; h) L. H. Hoang, N. T. M. Hien, W. S. Choi, Y. S. Lee, K. Taniguchi, T. Arima, S. Yoon, X. B. Chen, I.-S. Yang, *J. Raman Spectrosc.* **2010**, *41*, 1005-1010; i) J. Wu, S. Li, *The Journal of Physical Chemistry* **1995**, *99*, 4566-4568; j) S. B. Li, *Chin. J. Chem.* **2001**, *19*, 16-21.

[31] a) K. D. Singh Mudher, M. Keskar, K. Krishnan, V. Venugopal, *Journal of Alloys and Compounds* **2005**, *396*, 275-279; b) K. G. Bramnik, H. Ehrenberg, *Zeitschrift für anorganische und allgemeine Chemie* **2004**, *630*, 1336-1341; c) P. H. Bottelberghs, F. R. van Buren, *Journal of Solid State Chemistry* **1975**, *13*, 182-191; d) R. W. Goranson, F. C. Kracek, *The Journal of Chemical Physics* **1935**, *3*, 87-92.

[32] D. M. Hatch, S. Ghose, *Physics and Chemistry of Minerals* **1991**, *17*, 554-562.

[33] A. D. Fortes, *Acta Crystallogr E Crystallogr Commun* **2015**, *71*, 592-596.

[34] R. H. Busey, O. L. K. Jr., *The Journal of Chemical Physics* **1964**, *41*, 215-225.

[35] J. P. R. De Villiers, *American Mineralogist* **1975**, *60*.

[36] M. N. Iliev, M. M. Gospodinov, A. P. Litvinchuk, *Physical Review B* **2009**, *80*, 212302.

[37] B. A. L. De Mishima, T. Ohtsuka, N. Sato, *Journal of Electroanalytical Chemistry and Interfacial Electrochemistry* **1988**, *243*, 219-223.

[38] a) M.-C. Bernard, A. Hugot-Le Goff, B. V. Thi, S. Cordoba de Torresi, *J. Electrochem. Soc.* **1993**, *140*, 3065-3070; b) C. M. Julien, M. Massot, C. Poinsignon, *Spectrochimica Acta Part A: Molecular and Biomolecular Spectroscopy* **2004**, *60*, 689-700; c) F. Buciuman, F. Patcas, R. Craciun, D. R. T. Zahn, *Physical Chemistry Chemical Physics* **1999**, *1*, 185-190.

[39] F. Patcas, F. C. Buciuman, in *Zeitschrift für Physikalische Chemie, Vol. 215*, **2001**, p. 29.

[40] V. Fleischer, R. Steuer, S. Parishan, R. Schomäcker, *Journal of Catalysis* **2016**, *341*, 91-103.

[41] R. Koirala, R. Büchel, S. E. Pratsinis, A. Baiker, *Applied Catalysis A: General* **2014**, *484*, 97-107.

[42] Y. Gordienko, T. Usmanov, V. Bychkov, V. Lomonosov, Z. Fattakhova, Y. Tulenin, D. Shashkin, M. Sinev, *Catalysis Today* **2016**, *278*, 127-134.

9 Declaration of Authorship

This master thesis is based on experiments performed in the Department of Inorganic Chemistry of Prof. Dr. R. Schlögl at the Fritz-Haber-Institute of the Max-Planck-Society from August 2017 until February 2018.

I hereby declare that the thesis submitted is my own unaided work. All direct or indirect sources used are acknowledged as references.

_____ _____

Place, date Signature